8-31-2025

The global phase space of the three-vortex interaction system and its application to vortex-dipole scattering

Atul Anurag
New Jersey Institute of Technology, aa2894@njit.edu

ABSTRACT

THE GLOBAL PHASE SPACE OF THE THREE-VORTEX INTERACTION SYSTEM AND ITS APPLICATION TO VORTEX-DIPOLE SCATTERING

by
Atul Anurag

This dissertation presents a global reduction of the classical three-vortex problem that is free from coordinate singularities, enabling a comprehensive analysis of the system's dynamics across all circulation regimes.

To achieve this, a two-step symplectic reduction procedure is developed. The first step introduces Jacobi coordinates adapted to the symplectic structure of the vortex system, and the second applies a Lie-Poisson reduction to the resulting system. This formulation eliminates the non-physical singularities associated with collinear vortex configurations and facilitates a global phase space analysis, including a detailed and novel investigation of bifurcations.

Within this reduced framework, all relative fixed points are systematically identified and their stability and bifurcation behaviors are classified. The reduction is further applied to the vortex-dipole scattering problem, extending previous analyses to treat a more general case.

In this process, classical approaches dating back to Gröbli (1877), which relied on pairwise vortex distances, are extended and refined. While historically effective, those coordinates introduce singularities that obstruct a complete analysis. The present method overcomes these limitations, enabling a singularity-free and unified description of the full three-vortex dynamics.

A major challenge arises in the case of vanishing total circulation, where the Jacobi coordinate reduction fails. This is addressed by refining the reduction technique to handle the degenerate case and establishing a continuous connection to

the non-vanishing regime. This unified treatment enables a complete description of the three-vortex dynamics across all circulation configurations.

Finally, the methodology is extended to the integrable four-vortex problem that results under conditions of vanishing total circulation and linear impulse, providing new insight into vortex dynamics in regimes where classical tools are limited.

THE GLOBAL PHASE SPACE OF THE THREE-VORTEX INTERACTION SYSTEM AND ITS APPLICATION TO VORTEX-DIPOLE SCATTERING

by
Atul Anurag

A Dissertation
Submitted to the Faculty of
New Jersey Institute of Technology and
Rutgers, The State University of New Jersey—Newark
in Partial Fulfillment of the Requirements for the Degree of
Doctor of Philosophy in Mathematical Sciences

Department of Mathematics

August 2025

APPROVAL PAGE

THE GLOBAL PHASE SPACE OF THE THREE-VORTEX INTERACTION SYSTEM AND ITS APPLICATION TO VORTEX-DIPOLE SCATTERING

Atul Anurag

Dr. Roy H. Goodman, Dissertation Advisor — Date
Professor, Department of Mathematical Sciences, NJIT

Dr. Amitabha Bose, Committee Member — Date
Professor, Department of Mathematical Sciences, NJIT

Dr. David Shirokoff, Committee Member — Date
Associate Professor, Department of Mathematical Sciences, NJIT

Dr. Jonathan Jaquette, Committee Member — Date
Assistant Professor, Department of Mathematical Sciences, NJIT

Dr. Renato Calleja, Committee Member — Date
Associate Professor, Department of Mathematics and Mechanics,
Instituto de Investigaciones en Matemáticas Aplicadas y Sistemas,
Mexico City, Mexico

BIOGRAPHICAL SKETCH

Author: Atul Anurag

Degree: Doctor of Philosophy

Date: August 2025

Undergraduate and Graduate Education:

- Doctor of Philosophy in Mathematical Sciences,
  New Jersey Institute of Technology, Newark, NJ, 2025
- Master of Science in Applied Mathematics,
  National Institute of Technology, Warangal, Telangana, India, 2017
- Bachelor of Science (Honors) in Mathematics,
  Ramjas College, University of Delhi, New Delhi, India, 2015

Major: Mathematical Sciences

Presentations and Publications:

A. Anurag. Problem solver. In *Mathematical Problems in Industry Workshop, New Jersey Institute of Technology*, June 2023.

A. Anurag and D. L. Blackmore. Walking droplet dynamics research. In *Summer Talk, New Jersey Institute of Technology*, June 2021.

A. Anurag and R. H. Goodman. Continuation of periodic orbits in symmetric hamiltonian and conservative systems. In *Summer Talk, New Jersey Institute of Technology*, July 2023.

A. Anurag and R. H. Goodman. Global phase plane analysis of the three-vortex problem. In *2024 SIAM New York–New Jersey–Pennsylvania Section, Poster*, Nov. 2024.

A. Anurag and R. H. Goodman. The four-vortex motion with zero total circulation. *preprint*.

A. Anurag and R. H. Goodman. The global phase space of the three-vortex interaction system. *arXiv preprint arXiv:2504.16038*, 2025. https://arxiv.org/abs/2504.16038.

A. Anurag and R. H. Goodman. The phase space of the three-vortex problem. In *2024 SIAM Conference on Nonlinear Waves and Coherent Structures, Speaker, Baltimore, MD*, June 2024.

A. Anurag and R. H. Goodman. The phase space of the three-vortex problem and its application to vortex-dipole scattering. In *Summer Talk, New Jersey Institute of Technology*, June 2024.

A. Anurag and R. H. Goodman. Walking droplet dynamics research. In *Drexel University*, Mar. 2023.

A. Anurag, R. H. Goodman, and E. K. O'Grady. A new canonical reduction of three-vortex motion and its application to vortex-dipole scattering. *Physics of Fluids*, 36:067110, 2024.

A. Anurag, R. H. Goodman, and E. K. O'Grady. Point vortex dipole scattering. In *2023 SIAM New York–New Jersey–Pennsylvania Section, Poster*, Oct. 2023.

"Karmanye vadhikaraste Ma Phaleshu Kadachana,
Ma Karmaphalaheturbhurma Te Sangostvakarmani"

You have the right to perform your prescribed duty, but you are not entitled to the fruits of action. Never consider yourself the cause of the results of your activities, and never be attached to not doing your duty.

Bhagavad Gita 2.47

ACKNOWLEDGMENTS

I would like to express my deepest gratitude to my advisor, Prof. Roy H. Goodman, for his invaluable guidance and mentorship throughout my doctoral journey.

I would also like to extend heartfelt thanks to my late advisor, Prof. Denis Blackmore, for his unconditional support and for preparing me to succeed in this program.

I am also sincerely thankful to my committee members — Prof. David Shirokoff, Prof. Amitabha Bose, Prof. Jonathan Jaquette, and Prof. Renato Calleja — for their insightful feedback, and encouragement.

I am equally grateful to the Department of Mathematical Sciences for their financial support, and to the National Science Foundation, under grant DMS-2206016, which made my research possible.

I deeply appreciate everyone who contributed to creating a welcoming and organized environment during my PhD journey. In particular, I extend my gratitude to Wieslawa Kapturkiewicz for ensuring our workspace was always clean and inviting. Her kindness went beyond her duties—she would regularly stop by to greet us and check in on our well-being. I am forever indebted to her for the small, thoughtful gestures that had a profound impact on my daily life and made my time at NJIT so much smoother.

For most people, like me, coffee is a source of happiness. There is a Starbucks located in the Campus Center of NJIT, where Jackie, the Barista, always knew my order before I even asked. Though I usually got my coffee at 8:30 a.m., she would still take the time to ask me about my day. We often chatted about past vacations and the ones we planned to take in the near future, sharing pictures from our recent trips. Those small conversations became a delightful part of my daily routine, making

the simple act of getting coffee feel a little more special. I will always be empathetic toward her for her kind gestures.

I extend my deepest gratitude to Dr. Tattwamasi Amrutam for his invaluable mentorship. Our initial encounter occurred during my undergraduate studies at the Indian Institute of Sciences, Bangalore, India. At the time, he had recently completed his undergraduate degree and was eager to pursue his master's degree in mathematics at the Indian Institute of Technology, Mumbai, India. His guidance played a pivotal role in motivating me to pursue higher studies in mathematics. I hold him in the highest regard for his contributions. I am indebted to him for aligning my thoughts and guiding me to this moment, enabling me to achieve my goals.

I would also like to extend my sincere gratitude to the friends I made during my time in the U.S. for their warmth, generosity, and unwavering support. Coming from India, adapting to a new culture and environment was both exciting and challenging, but their welcoming nature made the transition so much easier. Dr. Tadanaga Takahashi, Dr. Nick Dubicki, Dr. Prianka Bose, Dr. Moshe Silverstein, Dr. Austin Juhl, Dr. Jake Brusca, David Mazowiecki, Nicholas Harty, Andrew White, Rey Sentina, Brian O'Donnell, Jose Pabón, Micheal Storm, Matthew Cassini, Elizabeth, Arianna, you not only helped me understand the nuances of American culture but also made me feel at home, far from home. Your kindness, patience, and willingness to share your experiences and traditions with me have been invaluable in helping me navigate this journey. Whether it was introducing me to new customs, sharing a meal, or simply offering advice and perspective, you have made my experience in the U.S. richer and more fulfilling. I am incredibly grateful for the friendships we have built, and I will always cherish the memories we have created together.

To my childhood friend, Dr. Kamal Rana, our journey from India to the United States has been a story of shared dreams and support. I still remember the long conversations we had when you were already in the United States and I was back in

India, planning and hoping to begin my PhD journey. Your guidance, encouragement, and insights during that time gave me clarity and confidence. A year later, when I finally made it here, having you by my side made this new country feel a little more like home. Thank you for being there every step, from childhood memories to academic milestones. Your friendship has been a constant in an ever-changing world, and I am truly grateful for your presence in my life—then, now, and always.

I just wanted to take a moment to express my deepest gratitude to my parents, Shrimati Shobha Sharma and Shri Satendra Kumar Sharma. They have been my rock through thick and thin, and I could not have done this without them. Their support, and encouragement have been the driving force behind my academic journey. Even when things got tough, they believed in me and gave me the strength to keep going. Their sacrifices, guidance, and constant presence in my life have been the foundation upon which this achievement rests. This dissertation is as much theirs as it is mine.

My heartfelt gratitude to my sister, Ankita Sharma, who has been like a second mother to me. Her care, guidance, and unconditional love have been a constant source of comfort and strength. She has supported me not only as a sibling but with the warmth and understanding of a parent, and for that, I am deeply thankful.

At last, but not the least, I would also want to express my deepest gratitude to my beloved Akanksha Dobriyal for being my constant companion and my emotional anchor. When I was feeling lost and alone, you were always there to listen and support me. Your patience, empathy, and belief in me helped me get through some of the toughest times. I am so grateful to have you in my life, and I love how much joy and positivity you bring into my days.

TABLE OF CONTENTS

Chapter **Page**

TABLE OF CONTENTS
(Continued)

Chapter **Page**

TABLE OF CONTENTS
(Continued)

Chapter **Page**

TABLE OF CONTENTS
(Continued)

Chapter **Page**

TABLE OF CONTENTS
(Continued)

Chapter **Page**

LIST OF FIGURES

Figure **Page**

LIST OF FIGURES
(Continued)

Figure **Page**

LIST OF FIGURES
(Continued)

Figure **Page**

LIST OF FIGURES
(Continued)

Figure **Page**

LIST OF FIGURES
(Continued)

Figure **Page**

CHAPTER 1

INTRODUCTION

1.1 Introduction to Point-Vortex Interactions

The dynamics of point vortices are governed by Euler's equations for an ideal, incompressible fluid. Helmholtz [22] derived a system of ordinary differential equations (ODEs) to describe the motion of interacting vortices as discrete particles, and later Kirchhoff reformulated them as a Hamiltonian system [27], which allows us to apply the theory of Hamiltonians to understand the dynamics of the system. This system governed by a Hamiltonian system of ordinary differential equations has garnered extensive research over the past 150 years [11, 12, 15, 16, 28, 30, 35, 37, 46, 47, 48].

Helmholtz's point-vortex model posits an inviscid, incompressible fluid confined to a nearly two-dimensional region. Within this fluid, vorticity is localized to a finite number of discrete points. Each of these point vortices generates a velocity field that, in turn, propels the other vortices to move. The study of such models is a standard topic in elementary fluid mechanics. Paul Newton's dedicated textbook covers the study of such models in great depth [37].

The point-vortex model has regained significance in the study of quantum fluids, particularly in the realm of Bose-Einstein condensates (BECs). A Bose-Einstein condensate is a state of matter composed of bosons cooled to temperatures approaching absolute zero. In this state, a substantial portion of the bosons occupy the same quantum state, leading to the manifestation of macroscopic quantum phenomena. When BECs undergo rotation, they exhibit the formation of quantized vortices, which are minuscule whirlpools characterized by the circulation of superfluid with quantized angular momentum. Notably, these quantized vortices exhibit

behavior that closely resembles the classical point vortices proposed by Helmholtz and Kirchhoff, as summarized by Lydon [31].

The convergence of classical and quantum vortex dynamics has made the point-vortex model a powerful tool in fluid mechanics. In regimes with few vortices, the system becomes analytically tractable, revealing insights into vortex motion, interaction, and stability. Among these few-vortex systems, the three-vortex problem stands out due to its rich mathematical structure and physical significance.

In subsequent sections, we discuss the reduction techniques in an attempt to solve a three-point vortex model, starting with Gröbli, who provided one of the first analytical reductions of this system.

1.2 Gröbli's Reduction for the Three-Vortex Problem

In his 1877 doctoral dissertation, Gröbli explored the complex dynamics of $N \geq 3$ interacting point vortices in an inviscid incompressible two-dimensional fluid. Furthermore, he provided an explicit reduction to quadratures of the three-vortex problem for arbitrary vortex circulations.

In this work, he formulated a widely-used reduction for the three-vortex system, describing the side lengths of the triangle formed by the vortices [20]. Specifically, he introduced evolution equations of relative motion for the squared pairwise distances between the vortices, which evolve as follows:

$$\frac{\partial}{\partial t}\begin{pmatrix} \ell_{23}^2 \\ \ell_{31}^2 \\ \ell_{12}^2 \end{pmatrix} = 4\sigma A \begin{pmatrix} \Gamma_1 \left(\ell_{12}^{-2} - \ell_{31}^{-2}\right) \\ \Gamma_2 \left(\ell_{23}^{-2} - \ell_{12}^{-2}\right) \\ \Gamma_3 \left(\ell_{31}^{-2} - \ell_{23}^{-2}\right) \end{pmatrix}, \tag{1.1}$$

where ℓ_{ij} denotes the distance between vortices i and j, A is the area of the triangle formed by the vortices, and $\sigma = \pm 1$ indicates the orientation of the triangle—positive if the vortices are ordered clockwise, and negative otherwise.

Given that the area of the region can be entirely expressed in terms of the side lengths using Heron's formula,

$$A = \frac{1}{4}\left(2\ell_{12}^2\ell_{23}^2 + 2\ell_{23}^2\ell_{31}^2 + 2\ell_{31}^2\ell_{12}^2 - \ell_{12}^4 - \ell_{23}^4 - \ell_{31}^4\right)^{1/2},$$

the system (1.1) is closed, except for the case where the three vortices are collinear. The dynamics governed by (1.1) preserve the equation

$$\Gamma_1\Gamma_2\ell_{12}^2 + \Gamma_2\Gamma_3\ell_{23}^2 + \Gamma_3\Gamma_1\ell_{31}^2 = 3L\Gamma_1\Gamma_2\Gamma_3, \tag{1.2}$$

where $L = \Theta - Q^2 - P^2$, $\mathbf{M} = \langle Q, P\rangle$ and Θ are the systems linear impulse and angular momentum, respectively, defined in Equation (3.6).

The conservation law expressed in Equation (1.2) permits the elimination of one variable, such as ℓ_{31}. As a result, Gröbli simplified the system to a set of quadratures. Since then, these equations have posed significant challenges for over 150 years (cf. [3], [37]). Goodman translated Grobli's dissertation into English [18].

In his 1893 treatise, Poincaré applied symmetry reductions to the vortex system, particularly by exploiting the conservation of linear and angular momentum, to reduce the complexity of the problem—a technique that remains standard in modern studies. Although not the first to examine the three-vortex problem (Gröbli's work predates his), Poincaré identified that the system admits three conserved quantities in involution—namely, the two components of linear impulse and the Hamiltonian—thus establishing the complete integrability of the system for arbitrary circulations [43].

In 1949, Synge gave a geometrical interpretation of Gröbli's solutions, using the coordinates that describe the position of a point relative to the three sides of a triangle, known as *trilinear coordinates* [47]. In a three-vortex system, the vertices of the triangle represents the positions of the vortices.

1.3 Trilinear Coordinates and Their Limitations

The trilinear coordinates approach to solving the three-vortex problem with arbitrary circulations was previously employed by Synge and Novikov [38, 47]. Building on Synge's contributions, Aref reformulated Gröbli's solution to the three-vortex interactions in 1979 using a different set of trilinear coordinates. Aref and his collaborators further explored and documented this historical development in subsequent works [6, 35].

1.3.1 Aref's trilinear coordinates

For $L \neq 0$, as defined in Equation (1.2), Aref introduces new variables:

$$b_1 = \frac{l_{23}^2}{\Gamma_1 L}, \quad b_2 = \frac{l_{31}^2}{\Gamma_2 L}, \quad b_3 = \frac{l_{12}^2}{\Gamma_3 L}, \tag{1.3}$$

which, by Equation (1.2), satisfy the constraint

$$b_1 + b_2 + b_3 = 3.$$

These variables can be interpreted as trilinear coordinates in the plane. Specifically, given three points p_1, p_2, and p_3 forming an equilateral triangle of height 3, any point in the plane can be uniquely represented by the triplet of signed distances b_j from that point to the lines extending the sides opposite vertices p_j of the triangle.

For the case where $L = 0$, the factor $\frac{1}{L}$ is omitted from the definition of the trilinear coordinates specified in Equation (1.3). Consequently, we obtain the following equation:

$$b_1 + b_2 + b_3 = 0.$$

The phase planes based on the trilinear coordinates introduced by Aref are shown in Figure 1.1 (a). The trilinear coordinates b_j describe the motion of a point in the plane. Since the coordinates ℓ_{ij} represent the sides of a triangle, they must satisfy

the triangle inequality, implying that not all triples of coordinates correspond to physically valid configurations.

Let $\mathcal{D}_{\text{phys}} \subset \mathbb{R}^3$ denote the domain of physical configurations, where each point in its interior represents two distinct phase points related by mirror symmetry. The boundary $\partial\mathcal{D}_{\text{phys}}$ consists of collinear configurations of the three vortices, and Aref demonstrated that it forms a conic section in the plane. For certain sets of circulations, this boundary is an ellipse, while for others, it is a hyperbola. Figure 1.1 illustrates three such phase diagrams.

- **Panel (a)** illustrates the phase diagram for circulations $(\Gamma_1, \Gamma_2, \Gamma_3) = (1, 1, 1)$, where the trajectories (level sets of a rescaled Hamiltonian denoted by θ) are confined within a circle that is tangent to the triangle formed by the axes of the trilinear coordinate system.
- **Panel (b)** presents the phase diagram for circulations $(\Gamma_1, \Gamma_2, \Gamma_3) = (1, 1, -1)$ with $L \neq 0$, where $\partial\mathcal{D}_{\text{phys}}$ is bounded by a hyperbola.
- **Panel (c)** depicts the case for $L = 0$, where the boundary is defined by the b_1 and b_2 axes. These diagrams correspond to Figures 2, 4, and 5 in Aref [2].

While the coordinate system simplifies some aspects of the problem, it also has certain drawbacks:

- The triplet (b_1, b_2, b_3) uniquely describes any point in the plane using signed distances from equilateral triangle sides. However, not all triplets (b_1, b_2, b_3) have physical significance because portions outside the shaded regions lack physical interpretation.
- The reliance on pairwise distances between vortices, which become degenerate when vortices are in a collinear state.
- The coordinate system lacks a global phase-plane making the general three-point vortex system difficult to analyze.
- The degeneracies introduced at collinear configurations make the system singular. For instance, the linearized dynamics near collinear states are undefined due to square-root singularities in Heron's formula.

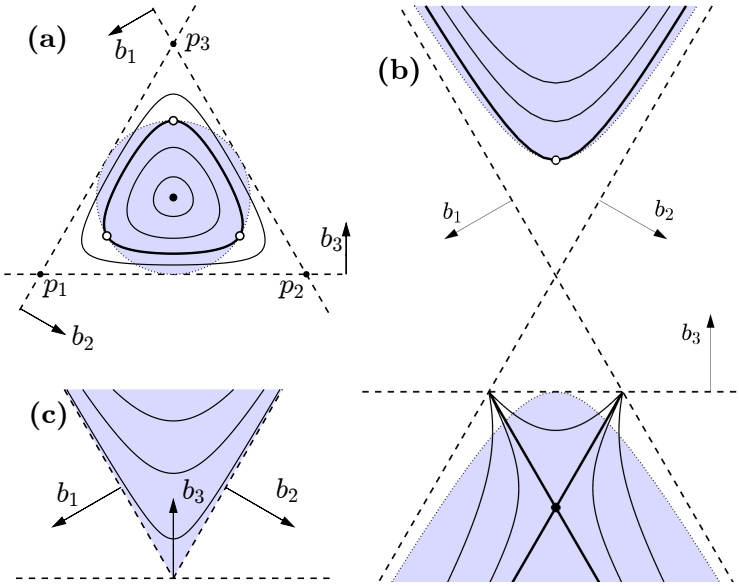

Figure 1.1 Phase diagrams in trilinear coordinates. Solid black lines are level sets of the Hamiltonian, but only the portions of these curves in $\mathcal{D}_{\text{phys}}$, shown here as shaded regions, are meaningful. Portions of the level sets lying outside them have no physical meaning. Collinear relative equilibria are marked $\circ$ and equilateral triangle relative equilibria $\bullet$. Heavier curves are separatrices. (a) Vortices of circulations $(1, 1, 1)$. (b) Vortices of circulation $(1, 1, -1)$ with $L \neq 0$. (c) Vortices of circulation $(1, 1, -1)$ with $L = 0$.

- Global phase-plane analysis is limited. For example, the reduced ODE system becomes unreliable near $\partial\mathcal{D}_{\text{phys}}$, even though the full vortex equations remain well-behaved except at vortex collisions.

These shortcomings motivated the researchers to explore alternative reduction methods to the three-point-vortex interactions. Conte's 1979 dissertation [16] uses a single complex parameter to describe triangle shape, though the transformation is difficult to interpret. Synge's original trilinear approach was revived by Tavantzis and Ting [48] to explore circulation dependence, but it shares the same issues as Aref's version. Aref himself later developed an algebraic approach to do a linear stability analysis for relative equilibria[1] of three vortices [4], limiting its utility for general dynamics.

[1] A vortex configuration is in relative equilibrium if it moves as a rigid body—the entire shape rotates or translates over time, but the distance between any two vortices stays the same.

It is noteworthy to mention some of the recent efforts that use geometric properties such as angles of a triangle. Krishnamurthy [28] derived equations of motion involving the triangle's interior angles and the circle that circumscribes that triangle. The relationships were established between the vortex strength ratios and the interior angles of the triangle. Makarov [32] proposed a reduction to the three-vortex problem. This reduction involves three vortices, where the invariant function is dependent on only two variables: the ratio of the lengths of any two sides of the vortex triangle and the angle between them.

Another coordinate system proposed by Stremler [46] is based on the interior angles of a triangle, which can be used as a trilinear coordinate system. This system naturally converts physical constraints but still suffers from singularities at collinear states, mirroring the drawbacks of the trilinear framework.

1.4 Alternative Coordinate Systems for Three-Vortex Dynamics

A coordinate singularity is a type of singularity that arises from the selection of coordinate system. This singularity can be eliminated by transforming to an alternative coordinate system through the specific choice of coordinates. Therefore, the choice of a proper coordinate system plays a significant role in reduction. All the reductions techniques that we discussed in Sections 1.2 and 1.3, introduces a non-physical singularity into the coordinate system at all collinear arrangements of the vortices.

The objective of this dissertation is to introduce a novel coordinate reduction method that facilitates the analysis of the global dynamics of three-vortex interactions. The primary goals of this work are:

- **Goal I:** To develop a coordinate reduction technique that eliminates coordinate singularities and enumerates all relative equilibria of the three-vortex problem, including their stability and the parameter values at which bifurcations occur.

- **Goal II:** A comprehensive application of a newly developed reduction method to a vortex-dipole scattering problem.
- **To-do Goal:** In Chapter 7, we demonstrate the method's applicability to an integrable four-vortex system characterized by vanishing net circulation and linear impulse. We present preliminary results that support the method's efficacy in such systems and plan to extend this work to provide a full phase space analysis.

CHAPTER 2

MATHEMATICAL TECHNIQUES AND DEFINITIONS

In this chapter, we provide a concise overview of key mathematical techniques and definitions relevant to this dissertation, establishing a foundation for more advanced discussions in subsequent chapters. This allows readers to reference these concepts as needed. The chapter is structured as follows:

Section 2.1 introduces the fundamental concepts and definitions of dynamical systems. Subsection 2.1.2 offers an overview of linear dynamical systems in $\mathbb{R}^N$, followed by a discussion on the stability of fixed points in Subsection 2.1.3. This section covers Lyapunov and asymptotic stability criteria and explores the classification of fixed points based on the Jacobian matrix. Understanding the nature of fixed points, such as stable nodes or saddle points, is essential for analyzing the long-term behavior of vortex systems.

In Section 2.3, we discuss Hamiltonian mechanics, a framework essential for understanding vortex motion. We begin by presenting the Hamiltonian equations of motion, which describe the evolution of generalized coordinates and momenta. We also introduce Poisson brackets, key to analyzing conserved quantities and symmetries within the system. This section provides the foundation for the Hamiltonian formulation of vortex dynamics discussed later in the dissertation.

In Subsection 2.3.4, we establish connections between stability theory and integrability conditions in dynamical systems, particularly within the context of Hamiltonian mechanics. The results presented in this chapter provide the essential tools for the more advanced discussions in the subsequent chapters.

2.1 Introduction to Dynamical Systems

In this section, we introduce fundamental notions of the geometric theory of (autonomous) dynamical systems. Consider the initial value problem of the form:

$$\frac{\mathrm{d}\mathbf{x}}{\mathrm{d}t} = \mathbf{f}(\mathbf{x}), \quad \mathbf{x}(t_0) = \mathbf{x}_0 \in \mathbb{R}^N, \tag{2.1}$$

where the vector field $\mathbf{f} : \mathcal{O} \to \mathbb{R}^N$ is assumed to be smooth and globally Lipschitz, with $\mathcal{O}$ being an open subset of $\mathbb{R}^N$. The fundamental existence and uniqueness theorem for differential equations guarantees the existence of a unique solution $\mathbf{x}(t)$ for each initial condition [14, 36, 42].

The solution or the *flow* ϕ_t of Equation (2.1) satisfies the following properties for all $\mathbf{x} \in \mathbb{R}^N$:

- ϕ_0 is an is an identity map, i.e., $\phi_0(\mathbf{x}) = \mathbf{x}$ and
- For all t and $s \in \mathbb{R}$,
$$\phi_t \circ \phi_s = \phi_{t+s}$$
where the composition symbol, $\circ$, means, $(\phi_t \circ \phi_s)(\mathbf{x}) = \phi_t(\phi_s(\mathbf{x}))$.

2.1.1 Orbits and invariant sets in dynamical systems

An *invariant set* is a subset $S \subset \mathbb{R}^N$ such that if a point $\mathbf{x}_0 \in S$, then the entire trajectory starting from $\mathbf{x}_0$, given by the flow $\phi_t(\mathbf{x}_0)$, stays within S for all future times t. Formally, a set S is invariant if:

$$\phi_t(S) \subseteq S \quad \text{for all} \quad t \in \mathbb{R}.$$

A set S is said to be *forward invariant* if $\phi_t(S) \subseteq S$ for all $t \geq 0$.

We now define some fundamental concepts related to dynamical systems and their trajectories under the flow ϕ_t.

- The *orbit* of a point $\mathbf{x}_0 \in \mathbb{R}^N$ under the flow ϕ_t is the set of all points that the solution $\mathbf{x}(t)$ reaches starting from $\mathbf{x}_0$, that is, the trajectory:

$$\{\phi_t(\mathbf{x}_0) : t \in \mathbb{R}\}.$$

- A non-constant solution to Equation (2.1) is a *periodic orbit* if there exists a period $T \neq 0$ such that:

$$\phi_{t+T}(\mathbf{x}) = \phi_t(\mathbf{x}) \quad \text{for all} \quad t \in \mathbb{R} \quad \text{and} \quad \mathbf{x} \in \mathbb{R}^N.$$

  If T is the smallest positive number with this property, it is called the *period* of the orbit.

- A point $\mathbf{x}_*$ is called an *equilibrium point* if its trajectory under the flow ϕ_t is invariant, meaning that

$$\phi_t(\mathbf{x}_*) = \mathbf{x}_* \quad \forall \quad t \in \mathbb{R}.$$

- A *homoclinic orbit* is a trajectory that connects an equilibrium point to itself. More precisely, a homoclinic orbit begins at an equilibrium point $\mathbf{x}_0$ and returns to the same point as $t \to \pm\infty$. Mathematically, a trajectory $\gamma(t)$ is homoclinic if:

$$\lim_{t\to\infty} \gamma(t) = \mathbf{x}_0 \quad \text{and} \quad \lim_{t\to-\infty} \gamma(t) = \mathbf{x}_0,$$

  where $\mathbf{x}_0$ is an equilibrium point.

- A *heteroclinic orbit* is a trajectory that connects two distinct equilibrium points. Specifically, if $\mathbf{x}_1$ and $\mathbf{x}_2$ are two different equilibrium points, a heteroclinic orbit is a trajectory that starts at $\mathbf{x}_1$ and asymptotically approaches $\mathbf{x}_2$ as $t \to \infty$. For a trajectory $\gamma(t)$, we have:

$$\lim_{t\to-\infty} \gamma(t) = \mathbf{x}_1 \quad \text{and} \quad \lim_{t\to\infty} \gamma(t) = \mathbf{x}_2,$$

  where $\mathbf{x}_1 \neq \mathbf{x}_2$ are distinct equilibrium points.

2.1.2 Linear systems in $\mathbb{R}^n$

A fundamental class of dynamical systems is given by linear systems, where the vector field $\mathbf{f}(\mathbf{x})$ depends linearly on $\mathbf{x}$. In N dimensions, the system (2.1) has the form

$$\frac{\mathrm{d}\mathbf{x}}{\mathrm{d}t} = A\mathbf{x}, \quad \mathbf{x}(0) = \mathbf{x}_0, \tag{2.2}$$

where A is a constant $N \times N$ matrix, admits a general solution of the form

$$\mathbf{x}(t) = e^{At}\mathbf{x}_0. \tag{2.3}$$

Here, the *fundamental solution operator* is given by the matrix exponential

$$e^{At} = \sum_{k=0}^{\infty} \frac{(At)^k}{k!}.$$

The solution follows from the existence and uniqueness theorem and is derived using the eigenvalues and eigenvectors of A, which are obtained by solving the characteristic equation

$$\det(A - \lambda \mathbb{I}_N) = 0. \tag{2.4}$$

This equation determines the long-term behavior of the system, which is closely related to stability properties.

2.1.3 Stability of fixed points

A fixed point (or equilibrium) of a dynamical system (2.1) is a point $\mathbf{x}^* \in \mathbb{R}^N$ such that

$$\mathbf{f}(\mathbf{x}^*) = 0. \tag{2.5}$$

At such a point, the system remains stationary, meaning $\dot{\mathbf{x}} = 0$.

Classification of fixed points An equilibrium point $\mathbf{x}^*$ of the system (2.1) is called a *hyperbolic* equilibrium point if all eigenvalues of the Jacobian matrix (2.6) evaluated at the equilibrium point $\mathbf{x}^*$ have non-zero real parts.

To classify a fixed point $\mathbf{x}^*$, we consider a linearization about the point $\mathbf{x}^*$ which defines a matrix

$$A := D\mathbf{f}(\mathbf{x}^*) = J(\mathbf{x}^*),$$

where $D\mathbf{f}(\mathbf{x}^*)$ is the Jacobian matrix of the vector field $\mathbf{f}$ evaluated at $\mathbf{x}^*$. The eigenvalues of A determine the local stability and nature of the equilibrium point $\mathbf{x}^*$. The classification is as follows:

- **Stable Node:** An equilibrium $\mathbf{x}^*$ is a stable node or a *sink* if all eigenvalues of A have negative real parts.
- **Unstable Node:** An equilibrium point $\mathbf{x}^*$ is an unstable node or a *source* if all eigenvalues of A have positive real parts.
- **Saddle Point:** An equilibrium point $\mathbf{x}^*$ if it is hyperbolic, but not a sink or a source.
- **Center:** An equilibrium point $\mathbf{x}^*$ is a center if all eigenvalues of A are purely imaginary (i.e., have zero real part).
- **Spiral (Focus):** An equilibrium point $\mathbf{x}^*$ is a spiral (or focus) if the eigenvalues are complex with nonzero real part. If the real parts are negative, the spiral is stable; if positive, it is unstable.

Lyapunov stability A fixed point $\mathbf{x}^*$ is *Lyapunov stable* if for every $\varepsilon > 0$, there exists $\delta > 0$ such that if $\|\mathbf{x}(0) - \mathbf{x}^*\| < \delta$, then for all $t \geq 0$,

$$\|\mathbf{x}(t) - \mathbf{x}^*\| < \varepsilon.$$

That is, trajectories starting sufficiently close to $\mathbf{x}^*$ remain close for all future times.[1]

[1] Lyapunov stability is a local property of the equilibrium, as it is defined in a neighborhood of $\mathbf{x}^*$. Specifically, the initial state $\mathbf{x}(0)$ must start within a distance δ to ensure that it remains within a distance ε of the equilibrium for all time. Since the choice of ε is arbitrary, δ is a function of ε, denoted as $\delta(\varepsilon)$. In some cases,

$$\lim_{\varepsilon \to \infty} \delta(\varepsilon) = \text{constant},$$

implying that Lyapunov stability holds only if $\mathbf{x}(0)$ starts within a fixed distance δ from $\mathbf{x}^*$, reinforcing its local nature. However, if one can show that $\delta(\varepsilon) \to \infty$ as $\varepsilon \to \infty$, then the stability property extends globally.

Asymptotic stability A fixed point $\mathbf{x}^*$ is *asymptotically stable* if it is Lyapunov stable and, in addition,

$$\lim_{t\to\infty} \mathbf{x}(t) = \mathbf{x}^*.$$

This implies that trajectories not only remain close to $\mathbf{x}^*$ but also eventually converge to it.

Neutral stability A fixed point $\mathbf{x}^*$ is *neutrally stable* if it is Lyapunov stable but not asymptotically stable. That is, trajectories starting near $\mathbf{x}^*$ remain within a bounded neighborhood for all time but do not converge to $\mathbf{x}^*$, as $t \to \infty$.

Linear stability A fixed point $\mathbf{x}^*$ of a nonlinear system (2.1) is said to be *linearly stable* if all of its solutions remain bounded for all time as $t \to \infty$, i.e., all the eigenvalues of A have non-positive real parts.

Moreover, any eigenvalue with zero real part must be *semisimple*, meaning that the matrix A has no nontrivial Jordan blocks corresponding to eigenvalues with zero real part. In this case, since the real parts of the eigenvalues are zero, the system exhibits no exponential growth or decay, and the solutions are bounded oscillations.

For a nonlinear system (2.1), the stability of a fixed point $\mathbf{x}^*$ can often be analyzed using the *Jacobian* matrix, given by

$$J(\mathbf{x}^*) = \left.\frac{\partial \mathbf{f}}{\partial \mathbf{x}}\right|_{\mathbf{x}=\mathbf{x}^*}. \tag{2.6}$$

To examine the stability of $\mathbf{x}^*$, we linearize the system by considering a small perturbation $\mathbf{y} = \mathbf{x} - \mathbf{x}^*$, leading to

$$\frac{\mathrm{d}\mathbf{y}}{\mathrm{d}t} = J(\mathbf{x}^*)\mathbf{y}, \quad \text{where } J(\mathbf{x}^*) = \left.\frac{\partial \mathbf{f}}{\partial \mathbf{x}}\right|_{\mathbf{x}=\mathbf{x}^*}. \tag{2.7}$$

This is a linear system whose solution is given by

$$\mathbf{y}(t) = e^{J(\mathbf{x}^*)t}\mathbf{y}_0. \tag{2.8}$$

Thus, the stability of $\mathbf{x}^*$ depends on the eigenvalues λ_i of $J(\mathbf{x}^*)$:

- If all $\mathrm{Re}(\lambda_i) < 0$, then $e^{J(\mathbf{x}^*)t}$ decays exponentially, implying **asymptotic stability**.
- If all $\mathrm{Re}(\lambda_i) \leq 0$, with at least one $\mathrm{Re}(\lambda_i) = 0$, the system is **Lyapunov stable** (solutions remain bounded but do not necessarily decay).
- If any $\mathrm{Re}(\lambda_i) > 0$, then $e^{J(\mathbf{x}^*)t}$ grows exponentially along at least one direction, making $\mathbf{x}^*$ **unstable**.

For cases where $J(\mathbf{x}^*)$ has repeated eigenvalues, the stability depends not only on the eigenvalues but also on the Jordan form of $J(\mathbf{x}^*)$:

- If all eigenvalues satisfy $\mathrm{Re}(\lambda_i) \leq 0$, but there exists a nontrivial Jordan block[2] corresponding to a zero eigenvalue, solutions may grow polynomially over time, indicating **neutral stability with polynomial growth**.
- If the Jordan form consists solely of diagonal blocks and $\mathrm{Re}(\lambda_i) \leq 0$, the system remains **Lyapunov stable**.
- If a nontrivial Jordan block corresponds to an eigenvalue with $\mathrm{Re}(\lambda_i) > 0$, instability is occurred due to polynomial-exponential growth.

Repeated eigenvalues with nontrivial Jordan blocks introduce complexities beyond simple exponential behavior, as transient dynamics may involve polynomial

[2] A Jordan block corresponding to an eigenvalue λ is a matrix of the form

$$J_k(\lambda) = \begin{bmatrix} \lambda & 1 & 0 & \cdots & 0 \\ 0 & \lambda & 1 & \cdots & 0 \\ \vdots & \vdots & \ddots & \ddots & \vdots \\ 0 & 0 & \cdots & \lambda & 1 \\ 0 & 0 & \cdots & 0 & \lambda \end{bmatrix}$$

of size $k \times k$. Nontrivial Jordan blocks ($k > 1$) lead to polynomial terms in the solution, which can result in the solution exhibiting non-exponential growth.

growth. This highlights the necessity of analyzing the full structure of $J(\mathbf{x}^*)$ rather than relying solely on its eigenvalues.

2.2 Bifurcations in Dynamical Systems

Consider a parametrized family of autonomous system (2.1):

$$\frac{\mathrm{d}\mathbf{x}}{\mathrm{d}t} = \mathbf{f}(\mathbf{x}; \mu), \tag{2.9}$$

where $\mu \in \mathbb{R}$ is a real parameter.

A bifurcation occurs at a critical parameter value $\mu = \mu^*$, where the qualitative behavior of the flow map $\phi_t(\mathbf{x}; \mu)$ changes. Bifurcations are broadly categorized as either *local* or *global*, depending on the extent of phase space involved in the qualitative change of the system's behavior.

2.2.1 Local bifurcation

Local bifurcations can be studied by analyzing the Jacobian matrix

$$J(\mathbf{x}^*; \mu) = \left.\frac{\partial \mathbf{f}}{\partial \mathbf{x}}\right|_{(\mathbf{x}^*, \mu)}$$

of the system (2.9) at an equilibrium point $\mathbf{x}^*(\mu)$.

A bifurcation occurs when an eigenvalue of this Jacobian crosses the imaginary axis as μ is varied, i.e., J has an eigenvalue with zero real part.

To understand the dynamics near such critical points, one often reduces the system to its normal form: a simplified version obtained through a local Taylor expansion and coordinate transformations that eliminate non-essential nonlinearities. Normal forms preserve the fundamental dynamical characteristics responsible for the bifurcation and help in demonstrating the universal behavior near the transition. The main types of local bifurcations include:

2.2.2 Saddle-node (fold) bifurcation

A bifurcation in which two fixed points (one stable and one unstable) collide and annihilate each other as the parameter passes through a critical value.

The normal form of the system for a saddle-node bifurcation is given by

$$\dot{\mathbf{x}} = \mu + \mathbf{x}^2, \tag{2.10}$$

where $\mu \in \mathbb{R}$ is a bifurcation parameter.

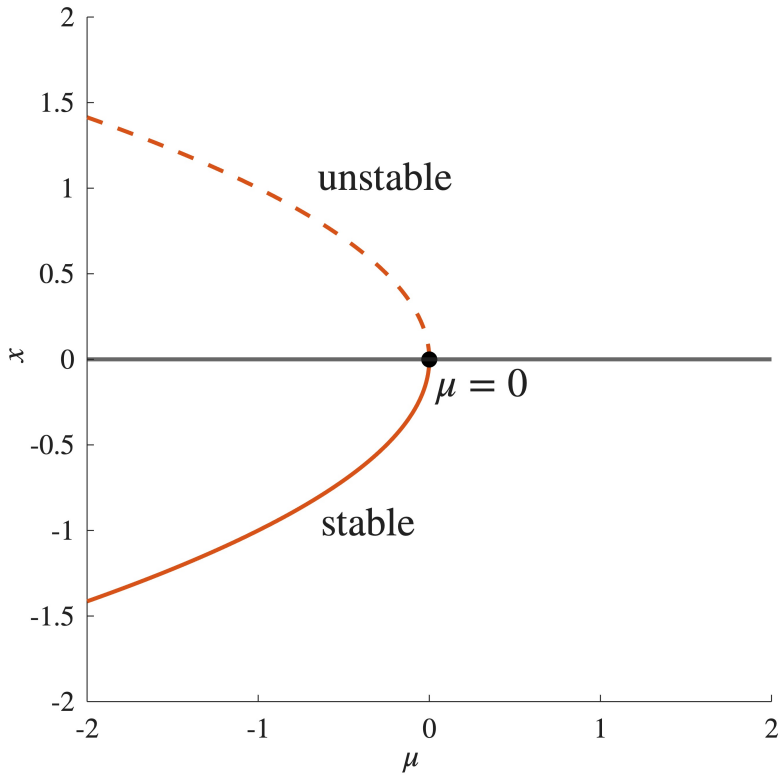

Figure 2.1 Bifurcation diagram for the saddle-node bifurcation.

In one dimension, the fixed points of the system (2.10) are obtained by solving $\dot{x} = 0$, which yields

$$x_* = \pm\sqrt{-\mu}.$$

These fixed points are real only when $\mu < 0$. Specifically:

- For $\mu < 0$, there are two distinct real fixed points: $x_- = -\sqrt{-\mu}$ and $x_+ = \sqrt{-\mu}$.
- For $\mu = 0$, there is a single fixed point at $x = 0$, where the two fixed points coalesce.
- For $\mu > 0$, there are no real fixed points, since the equation $\mu + x^2 = 0$ has no real solutions.

To analyze the stability of the fixed points, we can compute the derivative of the right-hand side of Equation (2.10) with respect to x. A **saddle-node bifurcation** occurs at $\mu = 0$. As the parameter μ increases through zero, two fixed points (one stable and one unstable) collide and annihilate each other. This marks the transition from a system with two real fixed points ($\mu < 0$) to a system with none ($\mu > 0$). The bifurcation diagram for a saddle-node is shown in Figure 2.1.

2.2.3 Transcritical bifurcation

A bifurcation where two fixed points intersect and exchange stability as the parameter varies. The normal form for a transcritical bifurcation is given by

$$\dot{\mathbf{x}} = \mu\mathbf{x} - \mathbf{x}^2, \tag{2.11}$$

where $\mu \in \mathbb{R}$ is a bifurcation parameter.

In one dimension, the fixed points of the system (2.11) are

$$x_* = 0 \quad \text{and} \quad x_* = \mu.$$

To analyze the stability of the fixed points, we compute the derivative of the right-hand side of Equation (2.11) with respect to x,

$$f'(x) = \mu - 2x.$$

- At $x_* = 0, f'(0) = \mu$. Therefore, the fixes point $x_* = 0$ is **stable** when $\mu < 0$ and **unstable** when $\mu > 0$.
- At $x_* = \mu, f'(0) = -\mu$. Therefore, the fixes point $x_* = \mu$ is **stable** when $\mu > 0$ and **unstable** when $\mu < 0$.

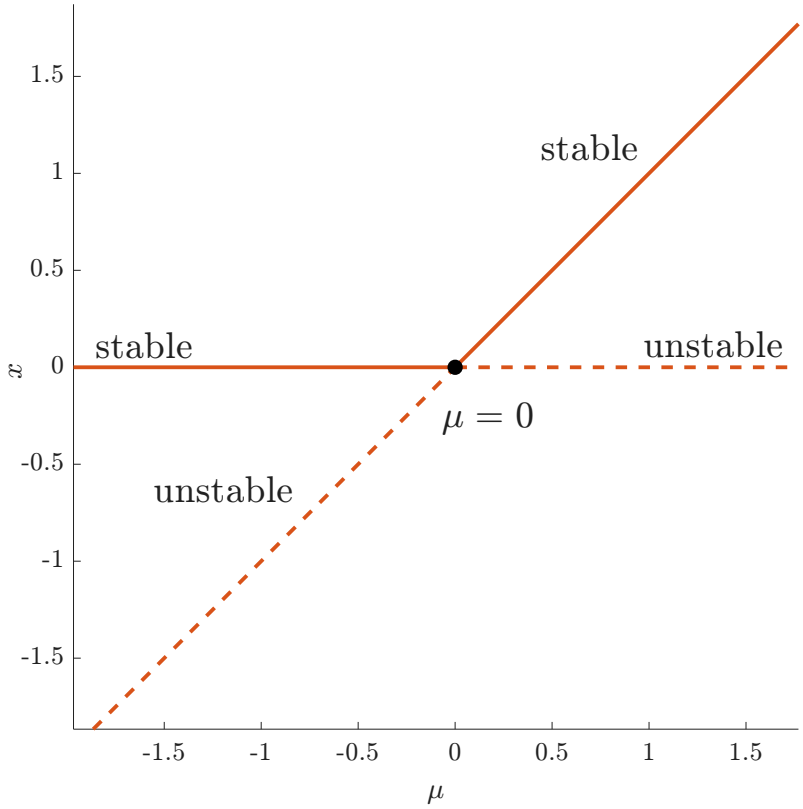

Figure 2.2 Bifurcation diagram for transcritical bifurcation.

As the parameter μ passes through zero, the two fixed points exchange stability. This phenomenon is characteristic of a transcritical bifurcation: both fixed points exist for all values of μ, but their stability changes as μ varies. See Figure 2.3.

2.2.4 Pitchfork bifurcation

A bifurcation involving symmetry, where a single fixed point either splits into three (one unstable and two stable) or merges from three into one, depending on whether the bifurcation is supercritical or subcritical.

The normal form for a pitchfork bifurcation is given by

$$\dot{\mathbf{x}} = \mu\mathbf{x} - \mathbf{x}^3, \tag{2.12}$$

where $\mu \in \mathbb{R}$ is a bifurcation parameter.

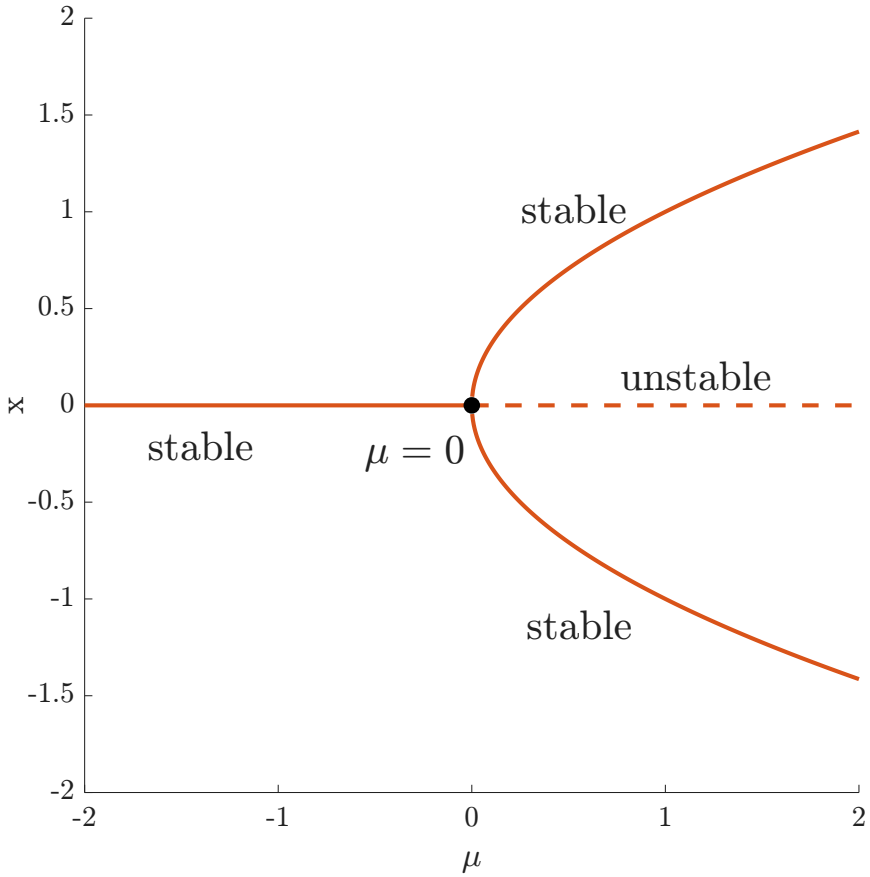

Figure 2.3 Bifurcation diagram for the *supercritical* pitchfork bifurcation.

Depending on the sign of μ, the system (2.12) either has three roots or one root.

- For $\mu < 0$, there is only one fixed point at $x_* = 0$.
- For $\mu > 0$, there are three fixed points: $x_* = 0$ and $x_* = \pm\sqrt{\mu}$.

To analyze the stability:

- At $x_* = 0$, the fixed point is **stable** for $\mu < 0$ and **unstable** for $\mu > 0$.

- The two nonzero fixed points $x_* = \pm\sqrt{\mu}$ (which exist only when $\mu > 0$) are both **stable**.

This behavior describes a *supercritical pitchfork bifurcation*, where the origin loses stability and a pair of symmetric, stable fixed points emerge as the bifurcation parameter μ becomes positive.

A *subcritical pitchfork bifurcation* can be obtained by reversing the sign of the cubic term, leading to symmetric *unstable* fixed points that exist for $\mu < 0$, which disappear as the origin becomes stable when $\mu > 0$.

2.3 Hamiltonian Dynamical Systems

2.3.1 Equations of motion

The Hamiltonian equations of motion describe the evolution of a dynamical system in terms of generalized coordinates $\mathbf{q}$ and generalized momenta $\mathbf{p}$. For any triplet $(\mathbf{q}, \mathbf{p}, t) \in \mathbb{R}^N \times \mathbb{R}^N \times \mathbb{R}$, the Hamiltonian function $H(q_i, p_i, t)$ represents the total energy of the system. The equations of motion are given by:

$$\dot{q}_i = \frac{\partial H}{\partial p_i}, \quad \dot{p}_i = -\frac{\partial H}{\partial q_i}, \tag{2.13}$$

where $i = 1, 2, \cdots, N$. If H is time independent, the system is said to be an autonomous system with N degrees of freedom.

A more compact and geometric formulation of a Hamiltonian system is as follows: Let $\mathbf{z} = (\mathbf{q}, \mathbf{p}) \in \mathbb{R}^{2N}$. For each smooth function $H : \mathbb{R}^{2N} \to \mathbb{R}$ the Hamiltonian vector field $X_H : \mathbb{R}^{2N} \to \mathbb{R}^{2N}$ is defined as

$$X_H(\mathbf{z}) := \left(\mathbb{J}^T\right)^{-1} DH(\mathbf{z}) = -\mathbb{J}DH(\mathbf{z}),$$

where $\mathbb{J}$ is the $2N \times 2N$ symplectic matrix defined as

$$\mathbb{J} := \begin{pmatrix} 0 & \mathbb{I}_N \\ -\mathbb{I}_N & 0 \end{pmatrix}$$

where $\mathbb{I}_N$ is the $N \times N$ identity matrix.

In this notation, Hamilton's equations take the form:

$$\frac{\mathrm{d}\mathbf{z}}{\mathrm{d}t} = \mathbb{J}\nabla H(\mathbf{z}, t). \tag{2.14}$$

2.3.2 Poisson brackets

Poisson brackets play a fundamental role in Hamiltonian mechanics, offering a powerful way to describe the time evolution of dynamical systems, symmetry properties, and conserved quantities.

Given a Hamiltonian system with canonical coordinates (q_i, p_i), the Poisson bracket of two functions $f(\mathbf{q}, \mathbf{p})$ and $g(\mathbf{q}, \mathbf{p})$ is defined as

$$\{f, g\} = \sum_{i=1}^{N} \left(\frac{\partial f}{\partial q_i} \frac{\partial g}{\partial p_i} - \frac{\partial f}{\partial p_i} \frac{\partial g}{\partial q_i} \right). \tag{2.15}$$

For a time-dependent function $f := f(\mathbf{q}, \mathbf{p}; t)$, we have

$$\begin{aligned} \frac{\mathrm{d}f}{\mathrm{d}t} &= \sum_{i=1}^{N} \left(\frac{\partial f}{\partial q_i} \frac{\partial q_i}{\partial t} + \frac{\partial f}{\partial p_i} \frac{\partial p_i}{\partial t} \right) + \frac{\partial f}{\partial t} \\ &= \{f, H\} + \frac{\partial f}{\partial t}. \end{aligned} \tag{2.16}$$

The Poisson brackets of the canonical coordinates in the phase space of $(\mathbf{q}, \mathbf{p})$ satisfy

$$\{p_i, p_j\} = \{q_i, q_j\} = 0, \quad \{q_i, p_j\} = \delta_{ij},$$

where δ_{ij} is the Kronecker delta.

The variables q and p are referred to as *conjugate* variables if and only if

$$\{q, p\} = 1.$$

For any functions $F, G, H \in C^2(\mathbb{R}^N \times \mathbb{R}^N \times \mathbb{R})$, the Poisson bracket is a bilinear operation defined on pairs of functions in $C^2(\mathbb{R}^N \times \mathbb{R}^N \times \mathbb{R})$, which satisfies the following conditions:

$$\begin{aligned} \{F, G\} &= -\{G, F\} && \text{(Antisymmetry)}, \\ \{FG, H\} &= F\{G, H\} + G\{F, H\} && \text{(Leibniz Rule)}, \\ \{aF + bG, H\} &= a\{F, H\} + b\{G, H\} && \text{(Bilinearity)}, \end{aligned}$$

and

$$\{F, \{G, H\}\} + \{G, \{H, F\}\} + \{H, \{F, G\}\} = 0 \quad \text{(Jacobi Identity)}.$$

If the system is governed by a Hamiltonian H, the time evolution of any function $f := f(\mathbf{q}, \mathbf{p})$ is given by:

$$\frac{\mathrm{d}f}{\mathrm{d}t} = \{f, H\}. \tag{2.17}$$

Applying this to the canonical coordinates q and p, we recover Hamilton's equations:

$$\dot{q}_i = +\frac{\partial H}{\partial p_i} = \{q_i, H\} \quad \text{and} \quad \dot{p}_i = -\frac{\partial H}{\partial q_i} = \{p_i, H\}.$$

In Hamiltonian mechanics, two functions f and g of the canonical phase-space coordinates (x, y) are said to be in *involution* if their Poisson bracket vanishes, i.e.,

$$\{f, g\} = 0.$$

This condition plays a fundamental role in integrable systems, where conserved quantities, or *integrals of motion*, govern the system's dynamics.

An *integral of motion* I is a function that remains constant along the flow of a Hamiltonian system if it satisfies

$$\frac{\mathrm{d}I}{\mathrm{d}t} = \{I, H\} = 0.$$

Substituting $f = H$ into Equation (2.16), we obtain:

$$\frac{\mathrm{d}H}{\mathrm{d}t} = \{H, H\} + \frac{\partial H}{\partial t}.$$

Since the Poisson bracket of any function with itself is identically zero,

$$\{H, H\} = 0.$$

Therefore, if the Hamiltonian has no explicit time dependence, i.e., $\frac{\partial H}{\partial t} = 0$, then

$$\frac{\mathrm{d}H}{\mathrm{d}t} = 0.$$

This implies that the Hamiltonian is conserved and serves as an integral of motion in autonomous systems.

2.3.3 Equilibrium points in Hamiltonian systems

In an autonomous Hamiltonian system, an equilibrium point corresponds to a state where the system's variables remain constant over time. These points are critical points of the Hamiltonian function and can be found by solving the Equation (2.14), i.e.,

$$\frac{\partial H}{\partial \mathbf{q}} = 0, \quad \frac{\partial H}{\partial \mathbf{p}} = 0.$$

Equilibrium points in Hamiltonian systems exhibit unique stability properties due to the conservative nature of the system. Since the Hamiltonian represents the system's total energy, it remains constant, preventing the system from having attractors or sinks, as is typical in dissipative systems. This characteristic is in contrast to general linear systems, where the behavior of equilibrium points, such as stable nodes or unstable sources, depends on the eigenvalues of the system's Jacobian matrix.

In Hamiltonian mechanics, equilibrium points are typically classified as either centers, saddles, or parabolics, with no equilibrium points being asymptotically stable. The possible behaviors of these points are:

- **Elliptic (Center):** These occur when the system's Jacobian matrix has purely imaginary eigenvalues, leading to closed, periodic orbits around the equilibrium point. This behavior is characteristic of neutral stability, where trajectories oscillate but do not decay to a fixed point, staying confined to a constant energy surface.
- **Hyperbolic (Saddle):** These points have eigenvalues with both positive and negative real parts, leading to divergent trajectories along certain directions. This indicates instability; however, due to energy conservation, the system does not settle into a steady state.
- **Parabolic (Degenerate):** These points occur when the Jacobian matrix has eigenvalues with zero real parts, causing the system to exhibit degenerate behavior. This can lead to non-oscillatory motion, where trajectories may neither settle to a fixed point nor exhibit typical periodic behavior.

The equilibrium points in Hamiltonian systems therefore exhibit oscillatory or unstable behaviors, but never lead to dissipation or the collapse of the system to a steady state.

2.3.4 Integrability condition and conserved quantities

A set of N integrals of motion in involution forms N *isolating integrals of motion*, restricting the system's trajectory within phase space. Noether's theorem connects

symmetries to conserved quantities: each continuous symmetry corresponds to an integral of motion.

The concept of integrability is closely linked to the Hamiltonian structure of a system, where the evolution is governed by a Hamiltonian function that represents the total energy. In such systems, the presence of conserved quantities can be directly linked to the symmetries of the Hamiltonian. We can draw the following important conclusions about conserved quantities in Hamiltonian systems:

- Invariance under translations in time yields that the value of the Hamiltonian is a conserved quantity (i.e., Energy is conserved).
- Invariance under translations provides conservation of linear momentum.
- Invariance under rotations provides conservation of angular momentum.

For Hamiltonian systems with n degrees of freedom, integrability conditions become more precise. A system is said to be *Liouville integrable* if there exist n functionally independent integrals of motion that are in involution, as they commute with each other. This result is known as Liouville's theorem. A detailed proof can be found in Arnold [8].

In such systems, trajectories in phase space are confined to a lower-dimensional manifold, and the system can, in principle, be solved analytically. The condition of integrability ensures a systematic approach to solving the equations of motion.

If a system with n degrees of freedom possesses k mutually involutive conserved quantities, its phase space can be reduced to $2(n-k)$ dimensions. This reduction occurs because each conserved quantity constrains the system's possible trajectories, effectively decreasing the number of independent variables. The more conserved quantities there are, the more the phase space is reduced.

When $k = n$, the system is said to be *completely integrable*, as all its degrees of freedom are effectively determined by the conserved quantities. In such a case,

the system can be solved in terms of quadratures—that is, by explicitly performing integrals.

CHAPTER 3

THE N POINT VORTEX MODEL

We begin this chapter by deriving the point-vortex solution to Euler's equations for an ideal fluid in Section 3.1. This foundational derivation establishes the governing equations for a system of discrete vortices. In Section 3.2, we extend this analysis to reveal the Hamiltonian structure of point-vortex dynamics, as formulated by Kirchhoff.

3.1 Point-Vortex Model

The point vortex model describes the motion of vortices in an ideal, incompressible, and inviscid fluid. Instead of considering continuous vorticity distributions, this model assumes that vorticity is concentrated at discrete points in the fluid domain. The governing equations for these vortices can be derived from Euler's equations for an ideal fluid.

3.1.1 Eulers equation

The velocity field of a point vortex can be represented by the velocity potential, ϕ, which is a scalar function that satisfies Laplace's equation. Let $\dot{\mathbf{x}} = \mathbf{u}(\mathbf{x}, t) = (u, v, w)$ be the velocity field of the fluid at a point $\mathbf{x} = (x, y, z)$ and $\rho(\mathbf{x}, t)$ be the mass density. The Euler's equations for an inviscid, incompressible flow with no external forces are given by:

$$\frac{\partial \mathbf{u}}{\partial t} + \mathbf{u} \cdot \nabla \mathbf{u} = -\frac{1}{\rho} \nabla \mathbf{p} \qquad \text{(Conservation of Momentum)}$$

$$\nabla \cdot \mathbf{u} = 0 \qquad \text{(Incompressibility Condition)}$$

$$\nabla^2 \phi = 0 \qquad \text{(Laplace's Equation)}$$

3.1.2 Vorticity equation

The vorticity, denoted by $\boldsymbol{\omega}$, is defined as the curl of the velocity field $\mathbf{u} = (u, v, w) \in \mathbb{R}^3$:

$$\boldsymbol{\omega} = \nabla \times \mathbf{u}.$$

A velocity field $\mathbf{u}$ is said to be irrotational if its vorticity $\boldsymbol{\omega}$ vanishes, i.e.,

$$\boldsymbol{\omega} = \nabla \times \mathbf{u} = 0.$$

Taking the divergence of the vorticity equation yields

$$\nabla \cdot \boldsymbol{\omega} = \nabla \cdot (\nabla \times \mathbf{u}) = 0,$$

since the divergence of a curl is always zero. Similarly, applying the curl to the vorticity yields

$$\nabla \times \boldsymbol{\omega} = \nabla \times (\nabla \times \mathbf{u}),$$

and utilizing the vector identity

$$\nabla \times (\nabla \times \mathbf{u}) = \nabla(\nabla \cdot \mathbf{u}) - \nabla^2 \mathbf{u},$$

the equation simplifies to

$$\nabla \times \boldsymbol{\omega} = -\nabla^2 \mathbf{u}.$$

For an *irrotational* incompressible flow, there exists a scalar potential function ϕ such that the velocity field is given by

$$\mathbf{u} = \nabla \phi.$$

This defines a *potential flow*, where the velocity field is derived from a potential function, ensuring irrotationality. If the flow has a rotational component, the *Helmholtz-Hodge decomposition* states that the velocity field $\mathbf{u}$ can be expressed as:

$$\mathbf{u} = \nabla\phi + \nabla \times \boldsymbol{\psi},$$

where:

- $\nabla\phi$ represents the *irrotational (potential) component*, and
- $\nabla \times \boldsymbol{\psi}$ represents the *solenoidal component* associated with vorticity.

Taking the curl, we obtain

$$\begin{aligned}
\nabla \times \mathbf{u} &= \nabla \times (\nabla\phi + \nabla \times \boldsymbol{\psi}) \\
&= \nabla \times \nabla\boldsymbol{\psi} \\
&= \nabla(\nabla \cdot u) - \nabla^2\boldsymbol{\psi} \\
&= -\nabla^2\boldsymbol{\psi}.
\end{aligned}$$

In two dimensions, the Poisson kernel in the plane is given by

$$G(\mathbf{x}) = \frac{1}{2\pi} \log \|\mathbf{x}\|.$$

This kernel can be used to determine the streamfunction $\boldsymbol{\psi}(\mathbf{x})$ from the vorticity distribution $\boldsymbol{\omega}(\mathbf{y})$ via the integral

$$\boldsymbol{\psi}(\mathbf{x}) = \int G(\mathbf{x} - \mathbf{y})\boldsymbol{\omega}(\mathbf{y})\, \mathrm{d}\mathbf{y}.$$

For a two-dimensional velocity field $\mathbf{u} = (u, v, 0)$, the *vorticity* has only one nonzero component,

$$\boldsymbol{\omega} = (0, 0, \omega),$$

where the vorticity $\omega(x, y, t)$ is given by

$$\boldsymbol{\omega} = (\nabla \times \mathbf{u})_z = \frac{\partial v}{\partial x} - \frac{\partial u}{\partial y}.$$

To determine the velocity field, we solve the *Poisson equation*

$$\nabla^2 \boldsymbol{\psi} = -\boldsymbol{\omega}.$$

For a known $\boldsymbol{\psi}$, the velocity components can be obtained from the stream-function using

$$\mathbf{u} = \nabla \times \boldsymbol{\psi} = \left(\frac{\partial \psi}{\partial y}, -\frac{\partial \psi}{\partial x}, 0 \right). \tag{3.1}$$

These equations describe the motion of a particle in the two-dimensional flow field governed by the vorticity-streamfunction formulation.

3.1.3 Discrete point-vortex approximation

Instead of a continuous vorticity field, we assume that vorticity is concentrated at discrete points:

$$\boldsymbol{\omega}(\mathbf{x}) = \frac{1}{2\pi} \sum_i \Gamma_i \delta(\mathbf{x} - \mathbf{x}_i),$$

where Γ_i is the strength of the vortex at the location $\mathbf{x}_i$, and δ is the Dirac delta function.

Given N vortices located at $\mathbf{x}_i = (x_i, y_i)$ with vorticity Γ_i, the solution to the Poisson equation in two dimensions is provided by the Poisson kernel:

$$\begin{aligned}\psi_i(\mathbf{x}) &= -\frac{\Gamma_i}{2\pi}\int \log\|\mathbf{x}-\mathbf{y}\|\delta(\mathbf{x}_i-\mathbf{y})\mathrm{d}\mathbf{y} \\ &= -\frac{\Gamma_i}{2\pi}\int \log\|\mathbf{x}-\mathbf{x}_i\|.\end{aligned}$$

The velocity field at any point in the fluid is expressed as a linear superposition of the velocities induced by individual point vortices. The velocity field at a position $\mathbf{x}$ can thus be written as:

$$\dot{\mathbf{x}} = \sum_{i=1}^{N} \nabla \times \boldsymbol{\psi}_i(\mathbf{x}, t),$$

where $\nabla \times \boldsymbol{\psi}_i(\mathbf{x}, t)$ represents the induced velocity due to the i-th point vortex, and N is the total number of vortices in the system.

Each vortex moves according to the velocity field generated by all other vortices, resulting in a system of coupled equations of motion. Consequently, the equation of motion for each point vortex in the system is:

$$\dot{\mathbf{x}}_j = \sum_{i\neq j}^{N} \nabla \times \boldsymbol{\psi}_i(\mathbf{x}_j, t).$$

The equations of motion can be written in component form using Equation (3.1)

$$\dot{x}_i = -\frac{1}{2\pi}\sum_{i\neq j}^{N} \Gamma_j \frac{(y_i - y_j)}{\|\mathbf{x}_i - \mathbf{x}_j\|^2}, \tag{3.2a}$$

$$\dot{y}_i = +\frac{1}{2\pi}\sum_{i\neq j}^{N} \Gamma_j \frac{(x_i - x_j)}{\|\mathbf{x}_i - \mathbf{x}_j\|^2}. \tag{3.2b}$$

3.2 The Hamiltonian N-Vortex Formulation

In this section, we review the Hamiltonian framework for the N-vortex problem. Consider a system consisting of N point vortices in the plane, each with position coordinates $\mathbf{r}_i = (x_i, y_i)$ and $2\pi\Gamma_i$ representing a non-zero circulation of the ith vortex, respectively. The dynamics of the system of $2N$ ordinary differential equations describing the N-vortex motion was first described by Helmholtz [22]:

$$\frac{\mathrm{d}x_i}{\mathrm{d}t} = -\sum_{j\neq i}^{N} \Gamma_j \frac{(y_i - y_j)}{\|\mathbf{r}_i - \mathbf{r}_j\|^2}, \quad \frac{\mathrm{d}y_i}{\mathrm{d}t} = \sum_{j\neq i}^{N} \Gamma_j \frac{(x_i - x_j)}{\|\mathbf{r}_i - \mathbf{r}_j\|^2}. \tag{3.3}$$

In 1876, Kirchhoff observed that this system admits a Hamiltonian formulation, albeit in a non-canonical form [27]. Unlike standard Hamiltonian mechanics, where momenta are naturally conjugate to position coordinates, the Hamiltonian formulation of point vortices requires a modification due to the dependence of the equations of motion on vorticity.

The dynamics of N point vortices can be expressed in terms of the Hamiltonian function

$$H(\mathbf{r}_1, \ldots, \mathbf{r}_N) = -\frac{1}{2} \sum_{i<j}^{N} \Gamma_i \Gamma_j \log \|\mathbf{r}_i - \mathbf{r}_j\|^2. \tag{3.4}$$

Kirchhoff's key insight was that the equations of motion could be rewritten in Hamiltonian form as

$$\Gamma_i \frac{\mathrm{d}x_i}{\mathrm{d}t} = \frac{\partial H}{\partial y_i}, \quad \Gamma_i \frac{\mathrm{d}y_i}{\mathrm{d}t} = -\frac{\partial H}{\partial x_i}, \tag{3.5}$$

where the position coordinates themselves play the role of conjugate variables. The presence of Γ_i modifies the usual Hamiltonian structure, leading to a non-canonical Poisson bracket formulation. The corresponding Poisson brackets are

$$\{f, g\} = \sum_{i=1}^{N} \frac{1}{\Gamma_i} \left(\frac{\partial f}{\partial x_i} \frac{\partial g}{\partial y_i} - \frac{\partial f}{\partial y_i} \frac{\partial g}{\partial x_i} \right),$$

with the fundamental bracket relation

$$\{x_i, y_i\} = \frac{1}{\Gamma_i}\delta_{ij}.$$

In addition, the system (3.3) has three well-known conservation laws, which we denote as:

$$\mathbf{M} = \langle Q, P\rangle = \sum_{i=1}^{N} \Gamma_i \mathbf{r}_i, \quad \text{and} \quad \Theta = \sum_{i=1}^{N} \Gamma_i \|\mathbf{r}_i\|^2. \tag{3.6}$$

The quantities $\mathbf{M}$ and Θ are known as the linear and angular impulses, respectively. They remain invariant under translations and rotations, respectively. As discussed in Subsection 2.3.4, Noether's theorem implies that, in addition to the Hamiltonian H, the system (3.5) possesses three constants of motion: $\mathbf{M}$ and Θ, i.e.

$$\{Q, H\} = \{P, H\} = \{\Theta, H\} = 0. \tag{3.7}$$

However, direct computation shows that these quantities do not generally commute under the Poisson bracket:

$$\{Q, P\} = \sum_{i=1}^{N} \Gamma_i, \quad \{P, \Theta\} = -2Q, \quad \{Q, \Theta\} = 2P. \tag{3.8}$$

This structure indicates that, in general, $\mathbf{M}$ and Θ are not in involution. However, in the special case where the total circulation vanishes, i.e.,

$$\sum_{i=1}^{N} \Gamma_i = 0,$$

it follows that $\{Q, P\} = 0$, implying that Q and P are in involution.

It is useful to define a new set of coordinates,

$$q_j = \sqrt{|\Gamma_j|}x_j \quad \text{and} \quad p_j = \sqrt{|\Gamma_j|}\text{sgn}(\Gamma_j)y_j. \tag{3.9}$$

With these new coordinates, the Poisson bracket between two functions f and g is simply given by the expression in Equation (2.15). These coordinates are canonical, meaning they satisfy the fundamental relation

$$\{q_i, p_j\} = \delta_{ij},$$

where δ_{ij} is the Kronecker delta.

Additionally, the evolution of the coordinates q_i and p_i is governed by the standard equations of motion:

$$\frac{\mathrm{d}q_i}{\mathrm{d}t} = +\frac{\partial H}{\partial p_i} \quad \text{and} \quad \frac{\mathrm{d}p_i}{\mathrm{d}t} = -\frac{\partial H}{\partial q_i}.$$

This normalization effectively removes the dependence on the parameter Γ_i from both the Poisson bracket and the equations of motion.

3.3 Integrability of the N Point-Vortex System

In this section, we analyze the integrability of the point-vortex system for arbitrary N, with a particular focus on the cases where $N \leq 3$. The system is completely integrable for $N \leq 3$, as it possesses enough conserved quantities to satisfy Liouville's criterion. For $N = 1$, a single vortex remains stationary, while for $N = 2$, the vortices either translate parallel to each other or rotate mutually, depending on their circulations. For $N = 3$, integrability is ensured by the existence of independent first integrals, which we derive using Hamiltonian mechanics and Poisson brackets.

However, for $N \geq 4$, the dynamics typically become chaotic, with integrability only possible under specific constraints, such as vanishing net circulation and linear impulse. The case of $N = 4$ is discussed further in Chapter 7.

3.3.1 One-vortex motion

For the single point vortex with the intensity Γ_1 at $\mathbf{r}_1 = (x_1, y_1)$, the Hamiltonian from Equation (3.4) is

$$H(\mathbf{r}_1) = 0, \tag{3.10}$$

which shows H is time-independent. Since the Hamiltonian is time-independent and the vortex's position is conserved, the system trivially admits integrability.

3.3.2 Two-vortex motion

Consider a system consisting of two vortices with circulations Γ_1 and Γ_2, respectively. The first vortex is located at $\mathbf{r}_1 = (x_1, y_1)$, while the second vortex is situated at $\mathbf{r}_2 = (x_2, y_2)$. From Equation (3.4), the Hamiltonian for this system is given by the following expression:

$$H(\mathbf{r}_1, \mathbf{r}_2) = -\frac{\Gamma_1 \Gamma_2}{4} \log \|\mathbf{r}_1 - \mathbf{r}_2\|^2. \tag{3.11}$$

The behavior depends on whether the net circulation is zero, so each case will be considered separately.

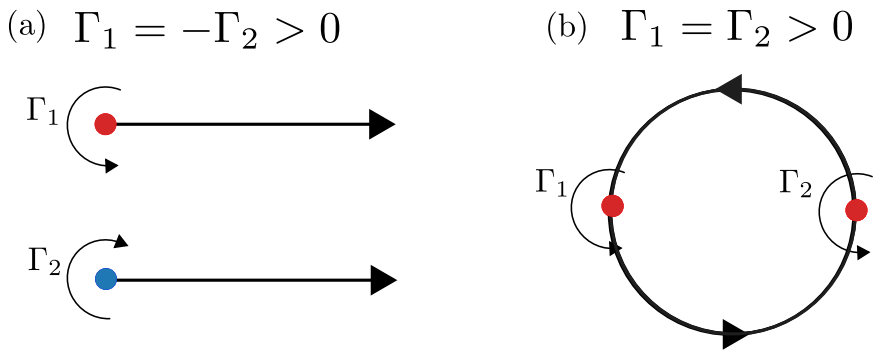

Figure 3.1 (a) Opposite-signed vortices move in parallel along straight lines. (b) Like-signed vortices move along a circular path, Behring [10].

Case I: $\Gamma_1 + \Gamma_2 \neq 0$

Since H depends only on the relative positions of the vortices, we introduce the following canonical transformation:

$$\mathbf{c} = \frac{\Gamma_1 \mathbf{r}_1 + \Gamma_2 \mathbf{r}_2}{\Gamma_1 + \Gamma_2}, \quad \mathbf{d} = \mathbf{r}_1 - \mathbf{r}_2, \quad D = \|\mathbf{d}\|. \tag{3.12}$$

From this definition, we obtain:

$$\mathbf{r}_1 = \mathbf{c} + \frac{\Gamma_2}{\Gamma_1 + \Gamma_2}\mathbf{d}, \quad \mathbf{r}_2 = \mathbf{c} - \frac{\Gamma_1}{\Gamma_1 + \Gamma_2}\mathbf{d}. \tag{3.13}$$

Since c is the conserved linear impulse the Hamiltonian simplifies to:

$$H = -\frac{\Gamma_1 \Gamma_2}{4} \log \|\mathbf{d}\|^2.$$

The system is Liouville integrable, with the conserved quantities in involution.

To determine the motion of the vortices, we differentiate Equation (3.12) with respect to time:

$$\dot{\mathbf{d}} = i\frac{\partial H}{\partial \mathbf{d}^*} \tag{3.14}$$

Since the center of vorticity $\mathbf{c}$ is a constant of motion, we have $\dot{\mathbf{c}} = 0$. The evolution of $\mathbf{d}$ is governed by the point vortex equations:

$$\dot{\mathbf{d}} = \boldsymbol{\Omega} \times \mathbf{d}, \tag{3.15}$$

where $\boldsymbol{\Omega}$ is the angular velocity of the relative motion. Using the known result from point vortex dynamics, the angular velocity of rotation is given by:

$$\omega = \frac{\Gamma_1 + \Gamma_2}{2\|\mathbf{d}\|^2}. \tag{3.16}$$

Thus, the two vortices undergo circular motion around $\mathbf{c}$ with angular velocity ω, maintaining a fixed separation $\|\mathbf{d}\|$. This confirms that in the case $\Gamma_1 + \Gamma_2 \neq 0$, the vortices exhibit rigid-body rotation about their common center of vorticity.

Case II: $\Gamma_1 + \Gamma_2 = 0$

When $\Gamma_1 + \Gamma_2 = 0$, the center-of-vorticity $\mathbf{c}$ is not well-defined, as the transformation (3.12) is no longer well-defined. However, from the definition of the linear impulse:

$$\mathbf{M} = \sum_i \Gamma_i \mathbf{r}_i = (Q, P),$$

we see that $\mathbf{M}$ is independently conserved. Fixing the linear impulse to lie along the y-axis with $Q = 0$ and $P = D$, and normalizing the circulations such that $\Gamma_1 = -\Gamma_2 = 1$, we obtain:

$$\mathbf{M} = \mathbf{r}_1 - \mathbf{r}_2 = (0, D).$$

That is, $x_1 = x_2$ and $y_1 = y_2 + D$, meaning the x-components are identical, while the difference in y-components is D. From the equations of motion:

$$\dot{x}_1 = \dot{x}_2 = \frac{1}{D}, \quad \dot{y}_1 = \dot{y}_2 = 0,$$

we conclude that the vortices move in parallel along the x-axis with a constant velocity of $\frac{1}{D}$. Therefore, the system is Liouville integrable, with the conserved quantity $\mathbf{M}$ representing the linear impulse and the relative distance D remaining constant throughout the motion.

Thus, for both $\Gamma_1 + \Gamma_2 \neq 0$ and $\Gamma_1 + \Gamma_2 = 0$, the two-vortex system satisfies the Liouville integrability conditions and is completely integrable for $N = 2$.

3.3.3 Three-vortex motion

The integrability of the three-vortex problem was first established by Gröbli [20]. Building on this, Henri Poincaré was the first to explicitly identify the first three integrals of the N-vortex problem, which were later examined in greater detail by Poincaré [43] and Synge [47]. After remaining largely unstudied for about 25 years, the problem was revisited by Novikov [38] in the special case of equal vortex strengths. Aref [2] then extended this analysis to general vortex strengths.

In this section, we examine the integrability of the system of point vortices for $N = 3$. Using Equation (3.8), we compute Poisson bracket of $Q^2 + P^2$ with Θ:

$$\{Q^2 + P^2, \Theta\} = 2Q\{Q, \Theta\} + 2P\{P, \Theta\} = 4PQ - 4PQ = 0.$$

This shows that $Q^2 + P^2$ is conserved under the evolution generated by Θ. Moreover, we verify the invariance of other quantities:

$$\{H, \Theta\} = 0, \quad \{H, Q^2 + P^2\} = 0.$$

Thus, the system possesses three independent integrals of motion: H, Θ, and $Q^2 + P^2$. According to Liouville's theorem, the existence of these integrals guarantees the system's integrability for $N = 3$, independent of the vortex strength values [3]. For a more detailed mathematical discussion on the integrability of the three-vortex problem, see Adams and Ratiu [34].

The integrability of the three-vortex problem enables us to analyze its Hamiltonian structure. In Chapter 4, we present a systematic reduction procedure that simplifies the dynamics of the three-vortex interactions while preserving the fundamental properties of the system.

CHAPTER 4

HAMILTONIAN REDUCTION TO THE THREE VORTEX SYSTEM

4.1 Canonical Reduction

Canonical reduction is a systematic approach to simplifying Hamiltonian systems with multiple symmetries by reducing them sequentially, eliminating one symmetry at a time while preserving the Hamiltonian structure. This methodology allows for a more tractable representation of the dynamics by transforming the phase space into a lower-dimensional manifold while maintaining its fundamental properties.

In the context of vortex dynamics, two key reductions are discussed in Sections 4.2 and 4.3:

- **Jacobi Coordinates Reduction** (Section 4.2): This transformation introduces a systematic redefinition of variables by incorporating the center of vorticity as a new coordinate. By iteratively redefining position variables, the Jacobi transformation reduces the degrees of freedom while preserving the Hamiltonian structure. This reduction is useful in all vortex circulations regime, but takes a different form when the total circulation vanishes.
- **Lie-Poisson Reduction** (Section 4.3): This reduction exploits the underlying symmetries of the vortex system, transforming the equations of motion into a reduced phase space governed by a Lie-Poisson structure. The introduction of the momentum map facilitates this process, leading to an alternative representation of the system where the dynamics are described in terms of conserved quantities and symmetry-adapted variables.

The combination of these reductions provides a robust framework for analyzing vortex motion in Hamiltonian systems. In the initial step, Jacobi coordinates eliminate translation symmetry, preserving the diagonal form of the Poisson bracket. Subsequently, the Lie-Poisson reduction eliminates rotational symmetry. Together, they lead to a systematic pathway for obtaining a reduced system that retains all essential dynamical features while being more amenable to analysis and computation.

4.2 Jacobi Coordinates Reduction

In celestial mechanics, Jacobi coordinates is a standard tool for reducing N body problems. It introduces a new set of coordinates that take into account the center of mass and relative distances between particles [26].

In a point-vortex model, the Jacobi coordinate transformation offers a systematic method to introduce the center of vorticity, $\mathbf{z}_0$, as a variable through a canonical change of variables. In these models, the mass of a particle is replaced by the circulation strength of a vortex. The Jacobi coordinate reduction method fails when the net circulations of the vortices are zero. However, in the case where $\gamma_1 = \sum_{j=1}^{N} \Gamma_j \neq 0$, then

$$\mathbf{z}_0 = \frac{\mathbf{M}}{\gamma_1}, \tag{4.1}$$

defines the conserved center of vorticity.

Since $\mathbf{z}_0$, defined in Equation (4.1), remains constant, Jacobi coordinates eliminate systems translation invariance and effectively reduce the system's degrees of freedom by one. In the case where the net circulation of the vortices vanishes, Equation (4.1) becomes undefined. We will discuss this scenario in more detail later in Section 5.6.

Beyond redefining the coordinates z_j, the procedure also modifies the structure of the Poisson bracket (2.15) by introducing new circulation variables $\tilde{\Gamma}_j$. The transformation is applied iteratively, replacing two conjugate variable pairs at each step, and continues for $N-1$ steps until all variables have been transformed. This approach naturally extends from the case of $N = 2$, which serves as the foundation for the iterative process.

Consider a Hamiltonian system of the form (3.4) with $N = 2$ and $\Gamma_1 + \Gamma_2 \neq 0$. Define the new position variables and *reduced circulations*

$$\begin{aligned} \tilde{z}_1 &= z_1 - z_2; & \tilde{\Gamma}_1 &= \frac{\Gamma_1 \Gamma_2}{\Gamma_1 + \Gamma_2}; \\ \tilde{z}_2 &= \frac{\Gamma_1 z_1 + \Gamma_2 z_2}{\Gamma_1 + \Gamma_2}; & \tilde{\Gamma}_2 &= \Gamma_1 + \Gamma_2. \end{aligned} \tag{4.2}$$

When $N \geq 3$, the transformation to Jacobi coordinates is iterative. The initial step involves the change of variables (4.2), preserving the variables with subscripts $3 \ldots N$. Subsequently, combine $\tilde{z}_2$ with z_3 using formulas analogous to (4.2), and continue this process with coordinates labeled k and $(k+1)$ until all position variables and circulations have been transformed. Figure 4.2 illustrates the case $N = 3$.

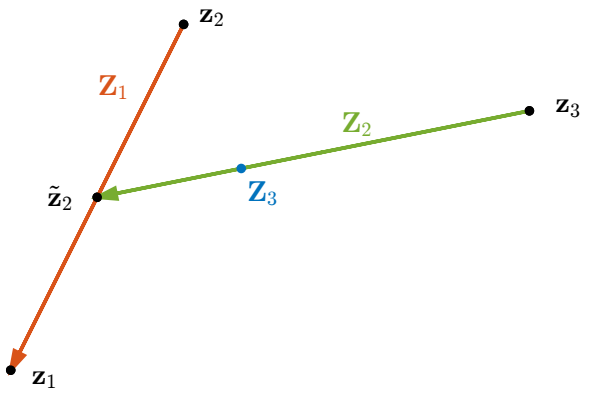

Figure 4.1 The Jacobi coordinates for three particles with nonzero total circulation are illustrated. $\mathbf{Z}_1$ represents the vector from $\mathbf{z}_2$ to $\mathbf{z}_1$, and $\mathbf{Z}_2$ denotes the vector from $\mathbf{z}_3$ to $\tilde{\mathbf{z}}_2$, which is the center of vorticity for the first two particles. The transformed variable $\mathbf{Z}_3$ serves as the conserved center of vorticity.

At step k, the change of variables becomes undefined if $\sum_{j=1}^{k+1} \Gamma_j = 0$. However, if the total circulation is nonzero, a particle ordering always exists that ensures this condition never arises.

The procedure yields a new position vector $\mathbf{Z} = (Z_1, \ldots, Z_{N-1})$ and a reduced circulation vector $(\kappa_1, \ldots, \kappa_{N-1})$. We have omitted the Nth position and reduced circulation since the former represents the conserved center of mass. Since the

Hamiltonian does not depend on this quantity, the system effectively has one degree of freedom less.

Jacobi coordinates have been implemented in the reduction to a three-vortex problem [24, 30], but each of them take distinct reduction strategy in its second step.

In the next section, we concentrate our discussion on the second stage of the Hamiltonian reduction to obtain the reduced system.

4.2.1 Jacobi coordinates for vanishing circulation

In case when the net circulations of vortices vanish, we require an alternative to the reduction described by Equations (4.2) that is applicable in the dipole case when $\Gamma_1 + \Gamma_2 = 0$. Ohsawa has identified the necessity for a distinct reduction method when the total circulation is zero [39].

Consider a system with two vortices. Referring to Figure 4.2, we define two position coordinates, Q_j, and momentum vectors, P_j, as follows:

$$\begin{aligned} Q_1 &= \frac{x_1 + x_2}{2}, \quad Q_2 = \frac{y_1 + y_2}{2}, \\ P_1 &= y_1 - y_2, \quad\quad P_2 = -x_1 + x_2. \end{aligned} \tag{4.3}$$

The Hamiltonian becomes:

$$H = \frac{\Gamma_1^2}{2} \log\left(P_1^2 + P_2^2\right).$$

The Poisson bracket and, consequently, the evolution equations, preserve the dependence on the magnitudes of the circulations but not their signs.

$$\begin{aligned} \frac{\mathrm{d}Q_j}{\mathrm{d}t} &= \frac{1}{\Gamma_1}\frac{\partial H}{\partial P_j}, \\ \frac{\mathrm{d}P_j}{\mathrm{d}t} &= -\frac{1}{\Gamma_1}\frac{\partial H}{\partial Q_j} = 0, \quad \text{for } j = 1, 2. \end{aligned}$$

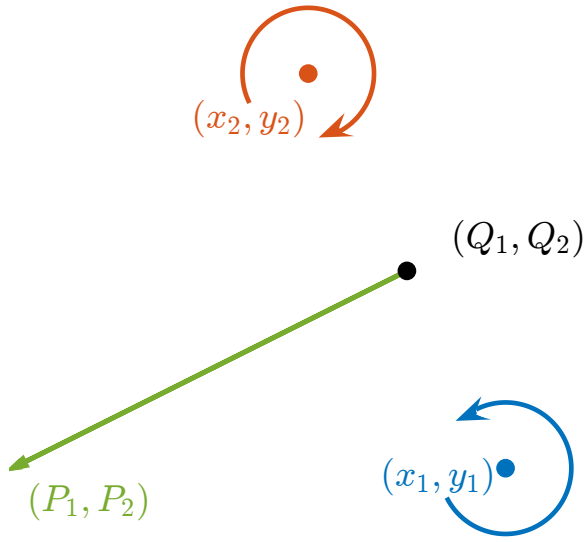

Figure 4.2 The alternative to Jacobi coordinates for two point-vortices with $-\Gamma_2 = \Gamma_1 > 0$.

The momenta are conserved since H is Q_j independent, and the particles move in a straight line at constant velocity:

$$\frac{\mathrm{d}}{\mathrm{d}t}(Q_1, Q_2) = \frac{\Gamma_1}{P_1^2 + P_2^2} \cdot (P_1, P_2)\,.$$

By selecting the orientation of the reference frame, we can set one component of the momentum, for instance, P_2, to zero.

This formulation differs from the Hamiltonian formulation (3.5), where the x and y coordinates represent positions. Here, we return to the standard case where Q variables represent positions and P variables represent momenta.

4.3 Lie-Poisson Reduction

Lie-Poisson structures were originally introduced by Sophus Lie [29] in the context of his work on Lie groups and their representation through canonical transformations. The functional maps defined in the subsequent sections that lead to the Jacobi-Lie-Poisson reduction, we recommend referring to the Appendix C for a review of the definitions and theory of Lie-Poisson dynamics.

4.3.1 Momentum map

Given a Hamiltonian system with a Lie group G acting on a symplectic manifold (M, ω), the momentum map

$$\mathbf{J} : M \to \mathfrak{g}^* \tag{4.4}$$

assigns to each point in phase space an element of the dual of the Lie algebra $\mathfrak{g}^*$, capturing the conserved quantities that arise from Noether's theorem.

The reduced dynamics then evolve on a Poisson manifold structured by the *Lie-Poisson bracket*

$$\{F, G\}(\xi) = \langle \xi, [\nabla F, \nabla G] \rangle, \quad \xi \in \mathfrak{g}^*, \tag{4.5}$$

where $[\cdot, \cdot]$ denotes the Lie bracket on $\mathfrak{g}$. This non-canonical bracket replaces the standard symplectic structure of Hamiltonian mechanics, resulting in an elegant geometric formulation, for reference, see Appendix C .

A concrete instance of such a reduction arises in the context of vortex dynamics, where the invariance of both the Poisson bracket (2.15) and the Hamiltonian (3.4) under the $\mathbb{S}^1$ action on $\mathbb{C}^N$ leads to a natural momentum map formulation. The group action

$$\mathbb{S}^1 \times \mathbb{C}^N \to \mathbb{C}^N; \left(e^{\mathrm{i}\psi}, \mathbf{z}\right) \mapsto e^{\mathrm{i}\psi}\mathbf{z}. \tag{4.6}$$

induces a reduction in phase space, where the momentum map

$$\mathbf{J} : \mathbb{C}^N \to \mathfrak{u}(N); \quad \mathbf{z} \mapsto \mu = \mathrm{i}\mathbf{z}\mathbf{z}^* \tag{4.7}$$

transforms the complex coordinates into a new variable μ, where $\mathfrak{u}(N)$ is the Lie-Algebra of Unitary Group $U(N)$.

This Lie-algebra is the space of $N \times N$ skew-Hermitian matrices, for a detailed proof, see Section C.14.

Since the Hamiltonian is invariant to $\mathbb{S}^1$ transformations of the form (4.6), it can be rewritten as a function of μ. If the Hamiltonian $H(\mathbf{z})$ is invariant under the $\mathbb{S}^1$ action, then it factors through the momentum map:

$$H(\mathbf{z}) = h(\mu), \quad \text{where } \mu = \mathbf{J}(\mathbf{z}). \tag{4.8}$$

Thus we may write the Hamiltonian as $h(\mu)$, where

$$H = h \circ \mathbf{J}. \tag{4.9}$$

The dynamics of μ follow from a Lie-Poisson structure defined on $\mathfrak{u}(N)^*$. The evolution equation [40]

$$\dot{\mu} = \mathsf{D}_\Gamma^{-1} \frac{\delta h}{\delta \mu} \mu - \mu \frac{\delta h}{\delta \mu} \mathsf{D}_\Gamma^{-1}, \tag{4.10}$$

where $\mathsf{D}_\Gamma := \operatorname{diag}(\Gamma_1, \ldots, \Gamma_N)$ demonstrates that the change of variables induced by the momentum map is a Poisson transformation, ensuring that the reduced dynamics remain Hamiltonian.

To establish the Poisson nature of this transformation, we introduce $\mathfrak{u}(N)_\Gamma$ as the space of skew-Hermitian matrices equipped with the bracket

$$[\xi, \eta]_\Gamma = \xi \mathsf{D}_\Gamma^{-1} \eta - \eta \mathsf{D}_\Gamma^{-1} \xi. \tag{4.11}$$

This bracket satisfies the Jacobi identity, making $\mathfrak{u}(N)_\Gamma$ a Lie algebra, see Section C.14. Now, we define an inner product on $\mathfrak{u}(N)_\Gamma$ as

$$\langle \xi, \eta \rangle = \frac{1}{2} \operatorname{tr}(\xi^* \eta)\,, \tag{4.12}$$

we can identify the dual space $\mathfrak{u}(N)_\Gamma^*$ with elements of $\mathfrak{u}(N)_\Gamma$, leading to the Poisson bracket

$$\{f, g\}_\Gamma(\mu) := \left\langle \mu, \left[\frac{\delta f}{\delta \mu}, \frac{\delta h}{\delta \mu}\right]_\Gamma \right\rangle. \tag{4.13}$$

It is easy to verify that the above momentum map is a Poisson map, i.e.,

$$\{f \circ \mathbf{J}, h \circ \mathbf{J}\} = \{f, h\}_\Gamma \circ \mathbf{J}. \tag{4.14}$$

Consequently, the reduced variables μ evolve under

$$\frac{\mathrm{d}}{\mathrm{d}t} f(\mu) = \{f, h\}_\Gamma. \tag{4.15}$$

For reference, see Section C.13. On applying Equation (4.15) to the components μ, we obtain the evolution Equation (4.10). For further details, we refer to Ohsawa [39, 40, 41] for applications in vortex dynamics and to Marsden and Ratiu [33] for the broader geometric mechanics framework.

In the next section, we make use of the theory introduced in Sections 4.2 and 4.3 to derive the reduced dynamics for the three-vortex system, specifically the $N = 3$ case.

CHAPTER 5

JACOBI-LIE-POISSON REDUCTION TO THE THREE VORTEX SYSTEM

5.1 Reduction to Three-Vortex System

In this section, we work on the reduction to the three-vortex system for $N = 3$. We define the three symmetric polynomials in three circulations to be

$$\gamma_1 = \Gamma_1 + \Gamma_2 + \Gamma_3; \quad \gamma_2 = \Gamma_1\Gamma_2 + \Gamma_2\Gamma_3 + \Gamma_1\Gamma_3; \quad \gamma_3 = \Gamma_1\Gamma_2\Gamma_3 \tag{5.1}$$

that will be frequently used in subsequent sections.

We begin by performing one stage of the Jacobi coordinates reduction, Equation (4.2). We assume that $\Gamma_1 + \Gamma_2 \neq 0$ to ensure the validity of the reduction process. Now, the next step depends on whether the total circulation is zero. In this context, we initially address the scenario where the total circulation is non-zero.

The second step when $\gamma_1 \neq 0$ is to apply the same change of variable to the variables $\tilde{z}_2$ and $\tilde{z}_3$. We call the transformed position coordinates Z_j and the virtual circulations κ_j, and

$$\begin{aligned} Z_1 &= z_1 - z_2; & \kappa_1 &= \frac{\Gamma_1\Gamma_2}{\Gamma_1 + \Gamma_2}; \\ Z_2 &= \frac{\Gamma_1 z_1 + \Gamma_2 z_2}{\Gamma_1 + \Gamma_2} - z_3; & \kappa_2 &= \frac{(\Gamma_1 + \Gamma_2)\Gamma_3}{\Gamma_1 + \Gamma_2 + \Gamma_3}; \\ Z_3 &= \frac{\Gamma_1 z_1 + \Gamma_2 z_2 + \Gamma_3 z_3}{\Gamma_1 + \Gamma_2 + \Gamma_3}; & \kappa_3 &= \Gamma_1 + \Gamma_2 + \Gamma_3. \end{aligned} \tag{5.2}$$

The variable Z_3 is the conserved center of vorticity. Without loss of generality, we may choose our coordinates to set $Z_3 = 0$. In this case, the Hamiltonian (3.4) becomes

$$H = \frac{-\Gamma_1\Gamma_2}{2}\log|Z_1|^2 - \frac{\Gamma_2\Gamma_3}{2}\log\left|Z_2 - \frac{\kappa_1}{\Gamma_2}Z_1\right|^2 - \frac{\Gamma_1\Gamma_3}{2}\log\left|Z_2 + \frac{\kappa_1}{\Gamma_1}Z_1\right|^2, \tag{5.3}$$

and

$$\Theta = \kappa_1 |Z_1|^2 + \kappa_2 |Z_2|^2. \tag{5.4}$$

The Poisson bracket and evolution equations in these variables depend on the *virtual positions* Z_1 and Z_2 and the *virtual circulations* κ_1 and κ_2 in the same way that Equations (2.15) and (3.5) depend on the physical positions z_j circulations Γ_j.

5.1.1 Reduction to Lie-Poisson form

We now apply the momentum-map reduction introduced in Subsection 4.3.1 to the reduced system in Z_j and κ_j with $N = 2$. The evolution in $\mathbf{Z} = (Z_1, Z_2)^\mathsf{T}$ is still invariant under $\mathbb{S}^1$ action on $\mathbb{C}^2$, defined as

$$\mathbb{S}^1 \times \mathbb{C}^2 \to \mathbb{C}^2; \left(e^{\mathrm{i}\psi}, \mathbf{Z}\right) \mapsto e^{\mathrm{i}\psi}\mathbf{Z}. \tag{5.5}$$

The momentum map, defined in Equation (4.7) for $N = 2$, is the function

$$\mathbf{J} : \mathbb{C}^2 \to \mathfrak{u}(2); \tag{5.6}$$

such that

$$\mathbf{Z} \mapsto \mu = \mathrm{i}\mathbf{Z}\mathbf{Z}^* = \mathrm{i}\begin{bmatrix} |Z_1|^2 & Z_1 Z_2^* \\ Z_1^* Z_2 & |Z_2|^2 \end{bmatrix} \tag{5.7}$$

From Equation (4.8), the Hamiltonian is invariant to $\mathbb{S}^1$ transformations of the form (5.5). Utilizing Equation (4.9), we can derive the evolution equation from Equation (4.10)

$$\dot{\mu} = \mathsf{D}_\kappa^{-1} \frac{\delta h}{\delta \mu} \mu - \mu \frac{\delta h}{\delta \mu} \mathsf{D}_\kappa^{-1}, \tag{5.8}$$

where

$$\mathsf{D}_\kappa := \mathrm{diag}(\kappa_1, \kappa_2). \tag{5.9}$$

A principal advantage of the Jacobi reduction is that it preserves the diagonal form of the matrix D_κ.

For the case $N = 2$, and using the inner product defined in Equation (4.12) induces an identification between $\mathfrak{u}(2)_\kappa$ and its dual space $\mathfrak{u}(2)^*_\kappa$. Specifically, the dual $\mathfrak{u}(2)^*_\kappa$ consists of all linear functionals on $\mathfrak{u}(2)_\kappa$, and each $\alpha \in \mathfrak{u}(2)^*_\kappa$ corresponds uniquely to an element $\alpha^\sharp \in \mathfrak{u}(2)_\kappa$ such that

$$\alpha(\mu) = \langle \alpha^\sharp, \mu \rangle$$

for all $\mu \in \mathfrak{u}(2)_\kappa$. This identification allows us to define the **Lie–Poisson bracket** on smooth functions f, g on $\mathfrak{u}(2)^*_\kappa \cong \mathfrak{u}(2)_\kappa$ by Equation (4.13).

Finally, the functional derivative $\frac{\delta f}{\delta \mu}$ is characterized by the property that for any $\mu, \nu \in \mathfrak{u}(2)^*_\kappa$,

$$\left\langle \nu, \frac{\delta f}{\delta \mu} \right\rangle = \frac{\mathrm{d}}{\mathrm{d}s}\bigg|_{s=0} f(\mu + s\nu). \tag{5.10}$$

For an element $\mu \in \mathfrak{u}(2)^*_\kappa$ of the form

$$\mu = \mathrm{i} \begin{bmatrix} \mu_1 & \mu_3 + \mathrm{i}\mu_4 \\ \mu_3 - \mathrm{i}\mu_4 & \mu_2, \end{bmatrix} \tag{5.11}$$

we obtain

$$\frac{\delta f}{\delta \mu} = \mathrm{i} \begin{bmatrix} 2\frac{\partial f}{\partial \mu_1} & \frac{\partial f}{\partial \mu_3} + \mathrm{i}\frac{\partial f}{\partial \mu_4} \\ \frac{\partial f}{\partial \mu_3} - \mathrm{i}\frac{\partial f}{\partial \mu_4} & 2\frac{\partial f}{\partial \mu_2} \end{bmatrix}, \tag{5.12}$$

Putting this all together, we can now say precisely how the momentum map is canonical. It is a *Poisson map* with respect to the Poisson brackets (2.15) and (4.13), which is defined in Equation (4.14).

Therefore, any smooth function $f(\mu)$ evolves under

$$\frac{\mathrm{d}}{\mathrm{d}t} f(\mu) = \{f, h\}_\kappa.$$

Applying this to the components of μ gives the evolution Equation (4.10).

From the map defined in Equation (5.7), we can interpret the μ_j coordinates geometrically. Consider the triangle formed by the variables Z_1 and Z_2, interpreted as vectors in $\mathbb{R}^2$. Writing $Z_j = R_j e^{\mathrm{i}\phi_j}$ and $\phi = \phi_1 - \phi_2$, we obtain

$$\mu_1 = R_1^2, \qquad \mu_2 = R_2^2, \qquad \mu_3 = R_1 R_2 \cos\phi, \qquad \mu_4 = R_1 R_2 \sin\phi. \tag{5.13}$$

In these variables, the angular impulse defined in Equation (5.4) is

$$\Theta = \kappa_1 \mu_1 + \kappa_2 \mu_2, \tag{5.14}$$

and we may consider the evolution Equations (5.8) as describing the behavior of a vector in $\mathbb{R}^4$.

Given that μ is defined as the exterior product of two vectors, its rank is at most one. Consequently, the two rows are redundant. To effectively utilize this fact, note that its determinant must vanish. For the matrix in Equation (5.11), this leads to the single real equation

$$\mu_1 \mu_2 - \mu_3^2 - \mu_4^2 = 0. \tag{5.15}$$

Since Θ is conserved, as is apparent from the first two components of system (5.20), it is worthwhile to make one more change of variables, defining

$$Z := \kappa_1 \mu_1 - \kappa_2 \mu_2 \quad \text{and} \quad X + \mathrm{i}Y := \mu_3 + \mathrm{i}\mu_4. \tag{5.16}$$

Then, the rank-one condition in Equation (5.15) becomes

$$\Theta^2 = Z^2 + 4\kappa_1\kappa_2 \left(X^2 + Y^2\right) = Z^2 + \frac{4\gamma_3}{\gamma_1}\left(X^2 + Y^2\right), \tag{5.17}$$

where the symmetric variables γ_1 and γ_3 are defined in Equation (5.1). Since Θ is conserved, trajectories are confined to a quadric surface in three-dimensional (X, Y, Z) space. Without loss of generality, we can assume that $\gamma_1 > 0$.

- The surface is a spheroid if one or three circulations are positive and the third is negative. A spheroid is an ellipsoid with two equal axes. In this case, $\Theta > 0$, and Z may take either sign.
- The surface is one sheet of a two-sheeted hyperboloid of rotation if two circulations are positive and the third is negative. A hyperboloid of rotation is a hyperboloid with two equal axes. In this case, $\gamma_3 < 0$, which implies $Z > 0$, but Θ may take either sign.
- If $\Theta = 0$, the hyperboloidal surface degenerates into an upper half-cone.

The distinction between spheroidal and hyperboloidal phase surfaces was noted in References [23, 24] using action-angle coordinates for Z_1 and Z_2.

5.2 Equations of Motion

In this section, we derive the equations of motion for the general three-vortex system, along with the fixed points and singularities of the system. From the notations defined in the Equations (5.1), (5.16), and (5.17), we may write the Hamiltonian (5.3) as:

$$\begin{aligned} h(X, Y, Z; \Theta) = &- \frac{\Gamma_1\Gamma_2}{2} \log(Z + \Theta) \\ &- \frac{\Gamma_1\Gamma_3}{2} \log\Big(4\gamma_3 X + (\gamma_1\Gamma_1 - \Gamma_2\Gamma_3)Z + (\Gamma_1 + \Gamma_2)(\Gamma_1 + \Gamma_3)\Theta\Big) \\ &- \frac{\Gamma_2\Gamma_3}{2} \log\Big(-4\gamma_3 X + (\gamma_1\Gamma_2 - \Gamma_1\Gamma_3)Z + (\Gamma_1 + \Gamma_2)(\Gamma_2 + \Gamma_3)\Theta\Big). \end{aligned} \tag{5.18}$$

Since the Hamiltonian is independent of the Y variable, using $\frac{\partial h}{\partial Y} = 0$ yields the evolution equations:

$$\frac{\mathrm{d}}{\mathrm{d}t}\begin{bmatrix} X \\ Y \\ Z \end{bmatrix} := \mathbf{F}(X,Y,Z) = \begin{bmatrix} -4h_Z Y \\ 4h_Z X - \frac{\gamma_1}{\gamma_3} h_X Z \\ 4h_X Y \end{bmatrix}. \tag{5.19}$$

This formula is valid regardless of sign γ_3 and thus unifies the two systems of equations derived in [1]. This system, like those, can be shown to be a *Nambu bracket* formulation of the equations, defined in terms of the Casimir Θ. A formal definition of a Casimir function along with its properties is discussed in the Section C.15.

It is also important to observe using the Equation (5.18), $\frac{\partial h}{\partial \mu_4} = 0$, so μ evolves according to

$$\frac{\mathrm{d}\mu}{\mathrm{d}t} = \begin{bmatrix} \frac{2}{\kappa_1}\frac{\partial h}{\partial \mu_3}\mu_4 \\ -\frac{2}{\kappa_2}\frac{\partial h}{\partial \mu_3}\mu_4 \\ 2\left(\frac{\frac{\partial h}{\partial \mu_2}}{\kappa_2} - \frac{\frac{\partial h}{\partial \mu_1}}{\kappa_1}\right)\mu_4 \\ 2\mu_3\left(\frac{\frac{\partial h}{\partial \mu_1}}{\kappa_1} - \frac{\frac{\partial h}{\partial \mu_2}}{\kappa_2}\right) + \frac{\partial h}{\partial \mu_3}\left(\frac{\mu_2}{\kappa_1} - \frac{\mu_1}{\kappa_2}\right) \end{bmatrix}. \tag{5.20}$$

We observe that the Hamiltonian (5.18) exhibits singularities when two vortices collide, and the argument of the corresponding logarithmic term becomes zero. These three singularities all occur for $Y = 0$ and must satisfy Equation (5.17). They are:

$$\begin{aligned} \mathcal{S}_{12} &= (0, 0, -\Theta)\,, \\ \mathcal{S}_{13} &= \left(\frac{-\gamma_1\Theta}{(\Gamma_1+\Gamma_2)(\Gamma_1+\Gamma_3)}, 0, \frac{(\gamma_1\Gamma_1 - \Gamma_2\Gamma_3)\Theta}{(\Gamma_1+\Gamma_2)(\Gamma_1+\Gamma_3)}\right), \\ \mathcal{S}_{23} &= \left(\frac{\gamma_1\Theta}{(\Gamma_1+\Gamma_2)(\Gamma_2+\Gamma_3)}, 0, \frac{(\gamma_1\Gamma_2 - \Gamma_1\Gamma_3)\Theta}{(\Gamma_1+\Gamma_2)(\Gamma_2+\Gamma_3)}\right). \end{aligned} \tag{5.21}$$

The subscripts denote the labels of the two vortices that coincide at the singularities. The coordinates of the singularities diverge if any pair of circulations satisfies $\Gamma_j + \Gamma_k \to 0$.

The relative fixed points of system (3.5) correspond to fixed points of system (6.2). For the three-vortex problem, there exist two primary families of relative fixed points: equilateral triangle configurations and collinear configurations.

5.2.1 Equilateral configurations

When $Y = 0$, the three vortices are collinear, so any equilateral configuration must have $Y \neq 0$. Such configurations are characterized by the conditions $h_X = 0$, $h_Z = 0$, and the rank-one constraint (5.17). Solving this system yields two solutions:

$$\mathcal{E}^{\pm}_{\text{tri}} = \frac{\Theta}{\gamma_2}\left(\frac{(\Gamma_1 - \Gamma_2)\gamma_1}{2(\Gamma_1 + \Gamma_2)},\ \pm\frac{\sqrt{3}\gamma_1}{2},\ \Gamma_1\Gamma_2 - \frac{(\Gamma_1^2 + \Gamma_2^2)\Gamma_3}{\Gamma_1 + \Gamma_2}\right). \tag{5.22}$$

These fixed points diverge as $\gamma_2 \to 0$. Geometrically, the condition $\gamma_2 = 0$ corresponds to the circle that circumscribes the central shaded triangle in Figure 5.1.

5.2.2 Collinear configurations

For all collinear configurations, $Y = 0$, so that $\frac{\mathrm{d}X}{\mathrm{d}t}$ and $\frac{\mathrm{d}Z}{\mathrm{d}t}$ vanish identically by Equation (6.2). Consequently, such configurations must satisfy both the condition $\frac{\mathrm{d}Y}{\mathrm{d}t} = 0$ and the rank-one constraint (5.17) evaluated at $Y = 0$. Both of these conditions are rational in the variables X and Z, and therefore their solutions correspond to the roots of a polynomial system of equations.

5.3 Stability Analysis to the Three-Vortex Motion

In this section, we delve into the stability analysis of the three-vortex motion. At the heart of this work lies a bifurcation diagram introduced by Conte in his 1979

dissertation and subsequently refined by the same author and Aref [4, 15, 16]. Figure 5.1 illustrates this diagram.

Our analysis provides a more intuitive interpretation of this diagram compared to previous treatments and expands its applicability. These configurations are naturally represented in terms of scaled circulations. We define these scaled circulations by assuming $\gamma_1 \neq 0$ in Equation (5.1) and setting

$$\eta_j = \frac{\Gamma_j}{\gamma_1}, \quad j = 1, \ldots, 3, \tag{5.23}$$

so that

$$\eta_1 + \eta_2 + \eta_3 = 1. \tag{5.24}$$

The parameters η_j thus serve as affine coordinates on the parameter space. Given three points (x_j, y_j) in the plane, any point can be expressed as

$$(x, y) = \sum_{j=1}^{3} \eta_j \cdot (x_j, y_j).$$

Choosing the reference points (x_j, y_j) as the vertices of an equilateral triangle is particularly convenient. This choice reflects the permutation symmetry of the vortex labels and simplifies the geometric interpretation of the system. Further details on these coordinates can be found in Appendix B. In terms of the scaled circulation variables, the condition for the phase surface to be a spheroid is $\eta_1\eta_2\eta_3 > 0$, which corresponds to the shaded regions in Figure 5.1. In contrast, when this product is nonpositive—i.e., in the unshaded regions—the phase surface becomes a hyperboloid.

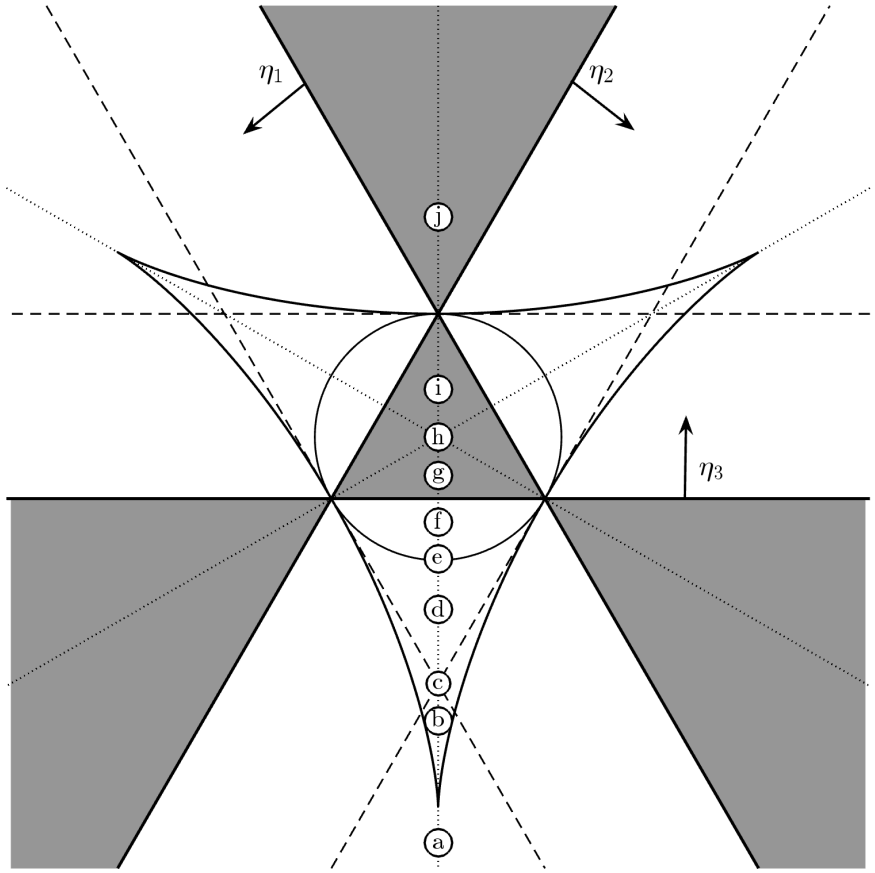

Figure 5.1 The trilinear diagram illustrates the different phases of phase space behavior. Each arrow indicates the direction in which the corresponding scaled circulation is positive, vanishing on the line from which it originates. In the shaded region the phase space is a spheroid, as defined by the quadric surface in Equation (5.17), while in the unshaded region, it is a hyperboloid.

To determine the linear stability of an equilibrium, we must linearize the system (6.2) about it. The Jacobian of this matrix is

$$D\mathbf{F} = \begin{bmatrix} -4h_{XZ}Y & -4h_Z & -4h_{ZZ}Y \\ \frac{-\gamma_1}{\gamma_3}h_{XX}Z + 4\left(h_{XZ}X + h_Z\right) & 0 & \frac{-\gamma_1}{\gamma_3}(h_X + h_{XZ}Z) + 4h_{ZZ}X \\ 4h_{XX}Y & 4h_X & 4h_{XZ}Y \end{bmatrix}, \quad (5.25)$$

where subscripts denote partial derivatives. The trace of this matrix is identically zero, and its determinant is given by

$$\begin{aligned} \det D\mathbf{F} = \; -16Y \Bigg[& \frac{\gamma_1 h_X}{\gamma_3}\left(h_X h_{XZ} - h_{XX}(h_Z + h_{ZZ}Z) + h_{XZ}^2 Z\right) \\ & + 4h_Z\left(h_{ZZ}(h_X + h_{XX}X) - h_{XZ}^2 X - h_{XZ}h_Z\right)\Bigg]. \end{aligned} \quad (5.26)$$

We now analyze the equilibrium by linearizing the system about the triangular solutions. In this case, the Jacobian (5.25) has the characteristic polynomial

$$\chi_{\text{tri}}(\lambda) = -\lambda^3 - \frac{3\gamma_2^3}{\Theta^2\gamma_1^2}\lambda. \quad (5.27)$$

The quadratic term vanishes because $\operatorname{tr} D\mathbf{F} \equiv 0$ and the constant term vanishes because the determinant (5.26) vanishes when $h_X = h_Z = 0$. As a result, the system always has one eigenvalue $\lambda = 0$. The remaining two eigenvalues determine the linear stability:

- The system is *linearly stable* when $\gamma_2 > 0$ (corresponding to points inside the circle),
- The system is *unstable* when $\gamma_2 < 0$ (outside the circle).

Computing the resultant of these two polynomials using `Mathematica`, as described in Section D.1, we can eliminate X from the system, resulting in the condition:

$$\rho(Z;\Gamma_1,\Gamma_2,\Gamma_3,\Theta) = -64\gamma_1\gamma_3^2(Z-Z_{12})(Z-Z_{13})(Z-Z_{23})\,p_3(Z;\Theta,\Gamma_1,\Gamma_2,\Gamma_3), \tag{5.28}$$

where the Z_{ij} terms are the Z-components of singularities found in Equation (5.21) and p_3 is a cubic polynomial in Z with Θ and the three circulations appearing as parameters. Since the three singularities cannot be solutions, the system will have one or three real roots, except at bifurcation points where there are two.

The number of solutions alters at parameter values where the discriminant of $p_3(Z)$, which is proportional to the resultant of p_3 and p_3', becomes zero; this is also discussed in Section D.2. We compute this in Mathematica. It factors into the product of low-degree terms that we can interpret:

$$\mathrm{Disc}_{p_3}(\Gamma_1,\Gamma_2,\Gamma_3) = 64\Theta^6(\Gamma_1-\Gamma_2)^2(\Gamma_1+\Gamma_2)^2\,{\gamma_1}^2{\gamma_2}^2{\gamma_3}^6\left(32\gamma_2{\gamma_1}^2-36\gamma_3\gamma_1-3{\gamma_2}^2\right). \tag{5.29}$$

We now review each of these factors.

5.4 The Factors

In this section, we will review of the factors that appears in the Equation (5.29).

The Factor Θ^6

When $\Theta \neq 0$, the evolution Equations (6.2) depend on X, Y, and Z solely through terms of the form $\frac{X}{\Theta}$, $\frac{Y}{\Theta}$, and $\frac{Z}{\Theta}$. Consequently, for fixed values of the circulations, the phase space and fixed points scale with Θ as long as sign (Θ) remains unchanged. This corresponds to the scale invariance of the general N-vortex problem.

As previously mentioned, when the conservation law (5.17) represents a spheroid, $\Theta > 0$; however, when it represents a hyperboloid, Θ can assume either positive or negative values or be equal to zero, resulting in three distinct families of phase planes.

The Factors $(\Gamma_1 - \Gamma_2)^2(\Gamma_1 + \Gamma_2)^2$

Given that the system of equations is invariant under permutations of the circulations, the bifurcations's locations must solely depend on the circulations through the symmetric polynomials. Consequently, any factors that depend on non-symmetric combinations of the circulations must be an artifact of the reduction method and do not signify bifurcations. It is important to remember that the vanishing discriminant is necessary but not sufficient for the two polynomials to vanish jointly. Specifically, the null vector may not conform to the form specified in Equation (D.1).

The Factor ${\gamma_2}^2$

This factor vanishes at the same points where we discovered the equilateral configurations lose stability: the circle in Figure 5.1. Since this term is a perfect square, the discriminant vanishes on the circle but does not change signs, and the number of solutions remains unchanged, except at the three points where the circle and deltoid (defined below) are tangent. However, as the circle is approached at other points, the coordinates of the two collinear relative equilibria diverge to infinity.

The Factor ${\gamma_3}^6$

We can expand this factor as ${\Gamma_1}^6{\Gamma_2}^6{\Gamma_3}^6$. Consequently, it vanishes when any circulations vanish, but it does not change signs as the circulations cross these lines,

as each is raised to an even power. Crossing these lines, the phase-surface topology transforms from a spheroid to a hyperboloid.

The Factor $(32{\gamma_1}^2\gamma_2 - 36\gamma_3\gamma_1 - 3{\gamma_2}^2)$

This factor is quartic in the circulations. Figure 5.1 illustrates the locus of solutions as a curved triangle with cusps at the three corners. This curve, known as the deltoid or Steiner's hypocycloid, is defined as the projection of a point on the circumference of a unit circle onto the inside of a circle of radius three. We confirmed this by computing the explicit form of the curve as a function of the Cartesian (x, y) variables necessary to input it into plotting software.

Within the deltoid, the system possesses three collinear equilibria; outside, it has only one. Where triple of circulations intersects the deltoid at any point other than the cusps or the vertices of the central triangular region, two equilibria undergo saddle node bifurcation. This bifurcation manifests as a pitchfork if the triple traverses the cusp along the deltoid's symmetry axis. This behavior exemplifies the *cusp catastrophe*.

In the next section, we apply this analysis to the collinear equilibria obtained in Subsection 5.2.2.

5.4.1 Linear stability of collinear fixed points

In this section, we analyze the linear stability of the collinear equilibria. As previously discussed, the fixed points are collinear when $Y = 0$. Substituting $Y = 0$ into the Jacobian (5.25), we observe that the four entries at the corners of the matrix vanish identically. Consequently, the characteristic polynomial takes the form:

$$\chi_{\text{coll}}(\lambda) = -\lambda^3 - r(\mathcal{E})\lambda, \tag{5.30}$$

where

$$r(\mathcal{E}) = \frac{-4\gamma_1}{\gamma_3}\left((h_X)^2 + h_X h_{XZ} Z - h_{XX} h_Z Z\right) - 16\left(-h_X h_{ZZ} X + h_{XZ} h_Z X + (h_Z)^2\right)$$

is a rational function in X and Z whose coefficients depend on Θ and the circulations Γ_j. An equilibrium $\mathcal{E}$ is stable when $r(\mathcal{E}) > 0$.

The collinear fixed points correspond to the roots of the cubic polynomial $p_3(Z)$ defined in Equation (5.28). Although this polynomial can, in principle, be solved using Cardano's formula, the resulting expressions are too complicated to yield any practical insight. Consequently, unlike the case of the triangular equilibria treated in Equation (5.27), we cannot directly evaluate $r(\mathcal{E})$ at a collinear equilibrium to derive a simple stability criterion.

Instead, we seek values of the circulations at which the stability undergoes a transition. At such points, we have $Y = 0$, and the remaining variables X and Z must satisfy three conditions: the rank-one constraint in Equation (5.17), the stationarity condition $\frac{\mathrm{d}Y}{\mathrm{d}t} = 0$, and the vanishing of the stability function $r(\mathcal{E}) = 0$.

To eliminate X and Z from this system, we compute a sequence of resultants. First, we select two pairs of equations and eliminate X from each pair, yielding two equations solely in Z. Then, we compute a third resultant to eliminate Z from these two. Carrying out this procedure in `Mathematica`, we find that the resulting condition for a stability transition takes the form:

$$\Theta^{24} p_{30}(\Gamma_1, \Gamma_2, \Gamma_3) \gamma_{12}^2 \gamma_{13}^2 \gamma_{23}^2 {\gamma_1}^{16} {\gamma_2}^4 {\gamma_3}^{24} \left(32{\gamma_2}{\gamma_1}^2 - 36\gamma_3\gamma_1 - 3{\gamma_2}^2\right) = 0, \tag{5.31}$$

where $\gamma_{ij} = (\Gamma_i + \Gamma_j)$.

All the factors are symmetric in the three circulations except for $p_{30}(\Gamma_1, \Gamma_2, \Gamma_3)$, a degree-30 homogeneous polynomial in the circulations. Like the $(\Gamma_1 - \Gamma_2)^2(\Gamma_1 + \Gamma_2)^2$ terms found in the discriminant formula above, the zeros of p_{30} do not correspond to

meaningful bifurcations, since p_{30} is not symmetric in the circulations. The factors

$$\gamma_1^{16}\gamma_2^4\gamma_3^{24}\left(32\gamma_2\gamma_1^2 - 36\gamma_3\gamma_1 - 3\gamma_2^2\right)$$

vanish on the same sets as the discriminant (5.29). The only new symmetric factor that appears in Equation (5.31) but is not present in the discriminant is

$$\gamma_{12}^2\gamma_{13}^2\gamma_{23}^2 = (\Gamma_1+\Gamma_2)^2(\Gamma_1+\Gamma_3)^2(\Gamma_2+\Gamma_3)^2.$$

This factor vanishes when two vortices have equal and opposite circulation and can form a dipole. This occurs along the three dashed lines in Figure 5.1. As these lines are approached, the coordinates of the two collinear fixed points diverge to infinity. However, this factor does not change sign along these lines and therefore does not indicate a change in stability.

5.4.2 The collinear equilibria when $\Gamma_1 = \Gamma_2$

We obtain more explicit and intuitive results by assuming $\Gamma_1 = \Gamma_2$, which corresponds to the y-axis in Figure 5.1. For simplicity, we set $\gamma_1 = 1$, so that $\Gamma_1 = \Gamma_2 = \frac{1-\Gamma_3}{2}$. Under this symmetry, the cubic polynomial $p_3(Z)$ in the resultant (5.28) factors into a linear and a quadratic term, revealing three collinear equilibria:

$$\begin{aligned}
\mathcal{E}_1 &= \frac{\Theta}{(1+\Gamma_3)(1+3\Gamma_3)}\left(\sqrt{\frac{5+3\Gamma_3}{1-\Gamma_3}},\, 0,\, -3\Gamma_3^2-6\Gamma_3+1\right),\\
\mathcal{E}_2 &= \frac{\Theta}{(1+\Gamma_3)(1+3\Gamma_3)}\left(-\sqrt{\frac{5+3\Gamma_3}{1-\Gamma_3}},\, 0,\, -3\Gamma_3^2-6\Gamma_3+1\right),\\
\mathcal{E}_3 &= (0,\, 0,\, \Theta)\,.
\end{aligned} \tag{5.32}$$

The equilibria $\mathcal{E}_1$ and $\mathcal{E}_2$ exist when the square root is real, i.e., for $-\frac{5}{3} < \Gamma_3 < 1$. As noted following (5.17), in the hyperboloid case $Z \geq 0$ implies that $\mathcal{E}_3$ exists only when $\Theta \geq 0$.

These bounds have geometric meaning in Figure 5.1: at $\Gamma_3 = -\frac{5}{3}$, the deltoid's cusp lies on the y-axis; at $\Gamma_3 = 1$, the upper edge of the deltoid is reached, where Γ_1 and Γ_2 vanish, reducing the system to a single-vortex problem. We now examine the Θ-dependence of the equilibria:

- **Spheroidal phase surface:** $\Gamma_3 > 0, \Theta > 0$
- **Hyperboloid phase surface:**

$$Z > 0 \Rightarrow \mathcal{E}_3 \text{ exists only if } \Theta > 0,$$
$$\mathcal{E}_1 \text{ and } \mathcal{E}_2 \text{ exist for } \begin{cases} \Theta > 0 & \text{if } -\frac{5}{3} < \Gamma_3 < -1, \\ \Theta < 0 & \text{if } -1 < \Gamma_3 < -\frac{1}{3}. \end{cases}$$

The stability function $r(\mathcal{E})$ from Equation (5.30) evaluates to

$$r(\mathcal{E}_1) = r(\mathcal{E}_2) = \frac{(\Gamma_3 - 1)^2(3\Gamma_3 + 1)^3(3\Gamma_3 + 5)}{64\Theta^2}, \qquad r(\mathcal{E}_3) = \frac{3(\Gamma_3 - 1)^3(3\Gamma_3 + 5)}{16\Theta^2}.$$

We observe that

- $r(\mathcal{E}_1) < 0$ for $-\frac{5}{3} < \Gamma_3 < -\frac{1}{3}$, indicating that $\mathcal{E}_1$ and $\mathcal{E}_2$ are centers;
- $r(\mathcal{E}_1) > 0$ for $-\frac{1}{3} < \Gamma_3 < 1$, so the equilibria are saddles;
- $r(\mathcal{E}_3)$ is positive for $-\frac{5}{3} < \Gamma_3 < 1$, implying that $\mathcal{E}_3$ is a saddle inside the deltoid and a center outside.

Figure 5.2 shows the bifurcation diagram for $\eta_1 = \eta_2$ and varying η_3, with separate panels for $\Theta = -1$ and $\Theta = 1$. Collinear and equilateral equilibria are shown, along with singularities. The bifurcation at $\eta_3 = -1$ is a pitchfork, while other bifurcations involve fixed points diverging to or returning from infinity, sometimes transitioning between the $\Theta = \pm 1$ surfaces. For $\eta_3 > 0$, the phase surface becomes spheroidal, and hence $\Theta < 0$ is not allowed.

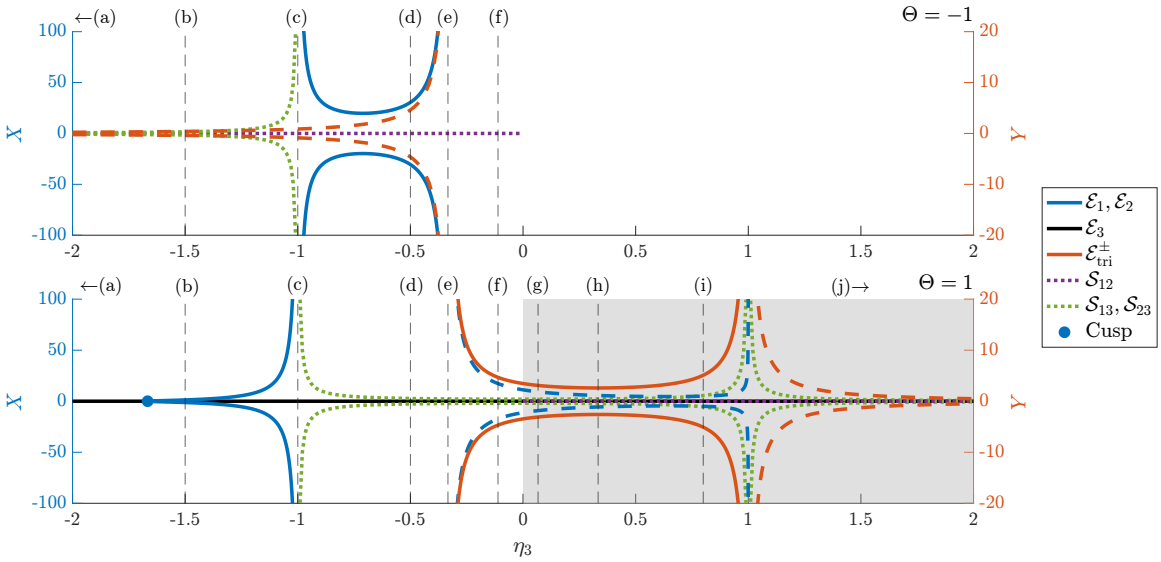

Figure 5.2 Bifurcation diagram displaying the equilibria and singularities defined by Equations (5.21), (5.22) and (5.32) for $\Theta = -1$ and $\Theta = 1$ as a function of η_3 along the vertical center line of Figure 5.1. The X-component of the collinear equilibria and singularities is shown using the y-axis scale on the left. The Y component of the triangular equilibria is shown using the y-axis scale on the right and the same shade of red as the Y-scale along the right edge of the figure. Solid lines show stable equilibria, dashed lines show unstable equilibria, and dotted lines show singularities. Dashed vertical lines show the η_3 values indicated by the letter labels in Figure 5.1. Cases **a** and **j** lie outside the plotted region.

5.5 Global Phase Portraits

In this section, we explore the global dynamics of the three-vortex system by examining representative phase portraits corresponding to different regions of the bifurcation diagram, including transitions across the boundaries. Particular attention is given to the nature of trajectories, fixed points, and connecting orbits, which together shape the topology of the phase space.

To simplify the analysis, we rescale the circulations and assume $\gamma_1 = 1$. With this normalization, the distinction between absolute circulations Γ_i and the scaled circulations defined in Equation (5.23) disappears. For consistency with earlier discussions of equilibria and singularities, we continue to denote the circulations by Γ_i throughout.

The structure of trajectories is closely tied to the geometry of the underlying phase surface. When the phase surface is a spheroid, all trajectories are necessarily bounded. In contrast, for hyperboloidal surfaces, unbounded motion is possible, although for most values of the circulations and angular impulse Θ, the trajectories remain bounded. The topology of phase space is also shaped by the configuration and connectivity of saddle points, with separatrices organizing families of periodic orbits and indicating potential transitions in qualitative behavior.

5.5.1 Two equal vortices

In this section, we focus our attention on a symmetric case in which $\Gamma_1 = \Gamma_2 = \frac{1-\Gamma_3}{2}$, corresponding to points on the vertical symmetry axis of the bifurcation diagram (Figure 5.1). Along this line, the fixed points and singularities are derived in Subsections 5.2.1 and 5.4.2. The phase surface is a spheroid for $\Gamma_3 > 0$ and becomes a hyperboloid for $\Gamma_3 < 0$, leading to a clear topological distinction in the global phase portraits. We consider a sequence of values labeled **a**–**j** along this symmetry axis to demonstrate how the phase space evolves as Γ_3 varies. In the spheroidal regime, the compactness of the surface ensures that all motion is bounded. In the hyperboloidal regime, though the phase surface is unbounded, bounded motion predominates, with unbounded trajectories arising only in special cases, which we identify explicitly.

Each diagram in this sequence depicts the equilibria and singularities relevant to that configuration, separatrix orbits emanating from hyperbolic points, and representative periodic orbits. These portraits provide insight into the global dynamics and how they are constrained by the underlying geometry.

To interpret the phase diagrams more intuitively, we recall the geometric meaning of the variables X and Y, defined in Equation (5.16). Referring to Equation (5.2) and Figure 4.2, the complex variable Z_1 represents the vector from vortex two to vortex one, while Z_2 denotes the vector from vortex three to the center of circulation of vortices one and two. Along the symmetry line $\Gamma_1 = \Gamma_2$, this center lies midway

between the two vortices. The variable Y equals the signed area of the parallelogram spanned by Z_1 and Z_2, and hence vanishes precisely when the three vortices are collinear. The variable X, being the dot product of these vectors, vanishes when they are orthogonal—a condition that corresponds to isosceles triangle configurations with vortex three at the apex opposite the equal sides. It is important to note that this orthogonality no longer implies isosceles geometry when $\Gamma_1 \neq \Gamma_2$.

5.5.2 Shperoidal phase surfaces

In this section, we will analyze the cases for values of Γ_3 for which the dynamics is confined to a spheroid, and we can assume $\Theta = 1$. We will visualize the spheroidal phase surfaces as spheres, disregarding the varying lengths of their axes. We will plot $Y = 0$ as the equator and the north and south poles at $Y = \pm 1$.

Point h: $\Gamma_3 = \frac{1}{3}$

The choice $\Gamma_3 = \frac{1}{3}$ yields the most symmetric case, in which all three vortices have equal circulation. This configuration corresponds to point **h** in Figure 5.1, with the associated global phase space shown in Figure 5.3.

The system features five equilibria. Three lie on the equator—$\mathcal{E}_1$, $\mathcal{E}_2$, and $\mathcal{E}_3$, each representing a collinear state. Due to symmetry, these equilibria are equally spaced. They are saddles, connected pairwise by heteroclinic orbits. The remaining two equilibria, denoted $\mathcal{E}^{\pm}_{\text{tri}}$, correspond to equilateral triangle configurations located at the north and south poles.

In addition, three singularities derived from Equations (5.21) lie along the equator, each situated midway between a pair of collinear equilibria.

On the front face of the phase space sphere, one observes the equilibrium $\mathcal{E}_3$ along with the singularities $\mathcal{S}_{13}$ and $\mathcal{S}_{23}$. The back face displays $\mathcal{E}_1$, $\mathcal{E}_2$, and the singularity $\mathcal{S}_{12}$.

The six heteroclinic orbits connecting the collinear saddles partition the sphere into five dynamically distinct regions, each containing a family of periodic orbits. Each heteroclinic connection corresponds to an exchange between a vortex at the end of a collinear segment and the one at its center. A family of periodic orbits surrounds each of the singularities on the equator. This family converges to a heteroclinic cycle connecting two collinear relative equilibria. An additional family of periodic orbits surrounds each of the equilateral equilibria. These families converge to a heteroclinic cycle connecting all three collinear equilibria.

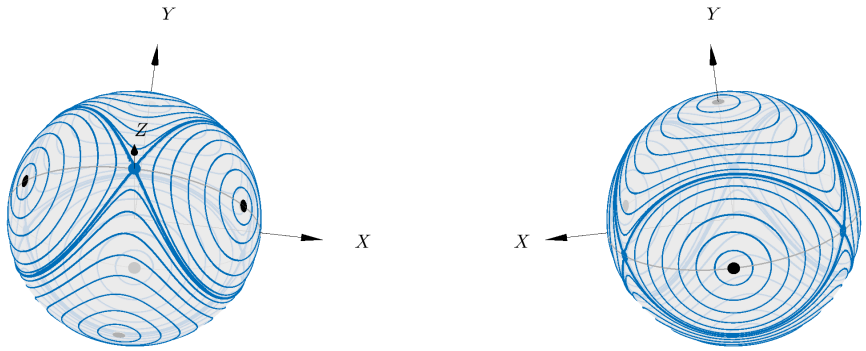

Figure 5.3 The global phase space corresponding to the case **h** with $\Gamma_3 = \frac{1}{3}$ is shown, presenting both the "front" and "back" views of the sphere. Singularities are indicated by black dots, collinear equilibria by blue dots, and triangular equilibria by gray dots. Separatrix orbits are depicted with thicker curves compared to periodic orbits. The equilibrium point $\mathcal{E}_3$ lies along the positive Z-axis in this and all subsequent plots. The periodic orbits shown are approximately equally spaced to ensure visual clarity, rather than spacing the level sets of the Hamiltonian evenly—an approach that would result in an accumulation of trajectories near each singularity. This marking convention is maintained consistently across all remaining figures.

Point g: $\Gamma_3 = \frac{1}{15}$

We now move downward to the point **g** in the figure, selecting $\Gamma_3 = \frac{1}{15}$; see Figure 5.4. No local bifurcations occur between this and the previous configuration; however, the two phase spheres differ in the topology of their periodic orbits and associated connecting trajectories. The collinear equilibrium $\mathcal{E}_3$ now lies on a different level set of

the Hamiltonian than the other two equilibria. Its invariant manifolds generate a pair of homoclinic orbits, each enclosing a family of periodic orbits that asymptotically approach a singularity. Additionally, four heteroclinic orbits connect the equilibria $\mathcal{E}_1$ and $\mathcal{E}_2$. The triangular equilibria $\mathcal{E}_{\text{tri}}^{\pm}$ have migrated closer to $\mathcal{E}_3$.

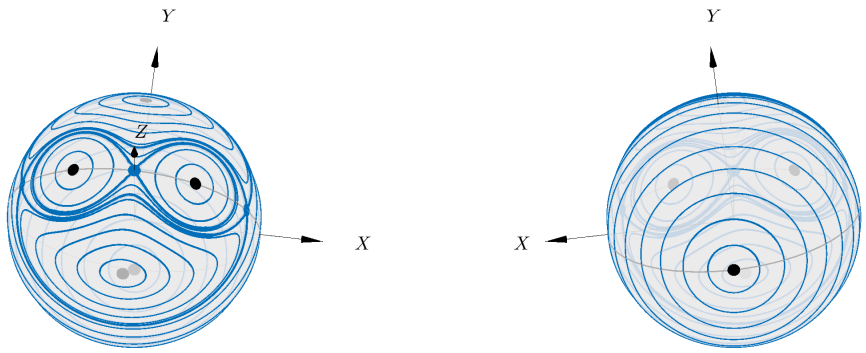

Figure 5.4 The global phase space for case **g** with $\Gamma_3 = \frac{1}{15}$. The invariant manifolds connected to $\mathcal{E}_3$ are homoclinic orbits oriented along the equator. The collinear equilibria $\mathcal{E}_1$ and $\mathcal{E}_2$ have migrated to the front.

Point i: $\Gamma_3 = \frac{4}{5}$

Proceeding to point **i** in the figure (see Figure 5.5), we observe that, as at point **g**, a pair of homoclinic orbits emanates from $\mathcal{E}_1$. In this case, however, they are oriented longitudinally, and each encloses a triangular equilibrium $\mathcal{E}_{\text{tri}}^{\pm}$. Four heteroclinic orbits once again connect the equilibria $\mathcal{E}_1$ and $\mathcal{E}_2$, though their configuration has changed relative to point **g**. The equilibria $\mathcal{E}_{\text{tri}}^{\pm}$, $\mathcal{E}_1$, and $\mathcal{E}_2$ have all migrated to the rear side of the phase space sphere. As Γ_3 continues to increase toward 1, these equilibria converge toward $\mathcal{E}_3$ when the phase surface is normalized to a unit sphere. In absolute coordinates, however, they diverge, as indicated by Equations (5.22) and (5.32).

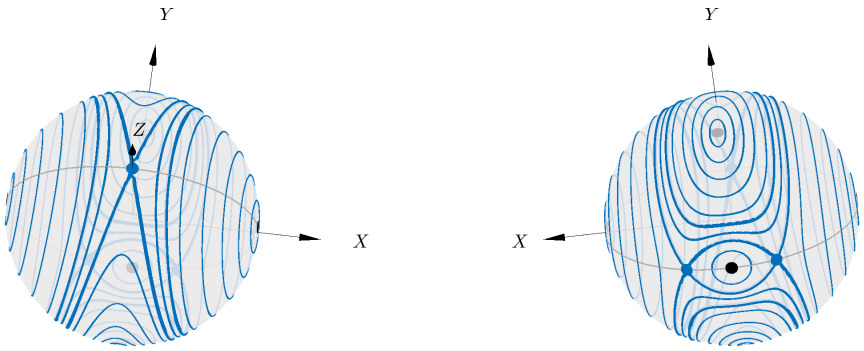

Figure 5.5 The global phase space for case **i** with $\Gamma_3 = \frac{4}{5}$, showing a reorganization of the homoclinic and heteroclinic structure compared to previous images.

Point j: $\Gamma_3 > 1$

The global phase space for $\Gamma_3 = 5$ is shown in Figure 5.6. At $\Gamma_3 = 1$, where $\Gamma_1 = \Gamma_2 = 0$, the dynamics degenerate to that of a single vortex. As Γ_3 increases beyond 1, the parameter point moves from the central shaded triangle in Figure 5.1 to the unbounded shaded region above it. The collinear equilibria $\mathcal{E}_1$ and $\mathcal{E}_2$ vanish, as they exist only within the deltoid region. Meanwhile, the triangular equilibria $\mathcal{E}_{\text{tri}}^{\pm}$ undergo a bifurcation on the circle, changing from centers to saddles. Heteroclinic cycles connecting the equilibria $\mathcal{E}_{\text{tri}}^{\pm}$ now encircle each of the three collinear singularities along with their surrounding families of periodic orbits. The stability of the remaining collinear equilibrium also changes—from unstable to stable—now surrounded by periodic orbits.

5.5.3 Hyperboloid phase surfaces

As Γ_3 crosses zero, the circulation parameters move into the unshaded region of the diagram in Figure 5.1, corresponding to a hyperboloid phase surface. We project this surface onto the plane $Z = 0$ and represent the resulting trajectories in a two-dimensional phase plane. All phase planes with $\Theta < 0$ are equivalent up to scaling, forming one equivalence class. Those with $\Theta > 0$ constitute a second equivalence class, while the phase plane corresponding to $\Theta = 0$ is qualitatively distinct. Accordingly,

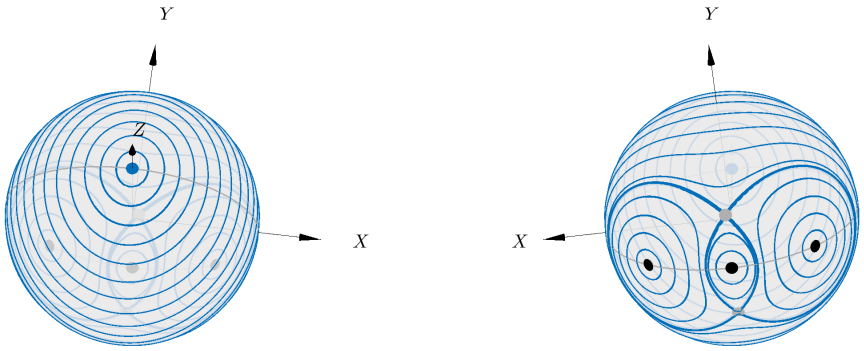

Figure 5.6 The global phase space for the case **j** with $\Gamma_3 = 5$. Only the single collinear equilibrium $\mathcal{E}_3$ remains and is a center. The two equilateral triangular equilibria $\mathcal{E}^{\pm}_{\text{tri}}$ are now saddles.

for each value of Γ_3, we present three phase planes—one for each case. The three vortices are positioned collinearly along the line $Y = 0$ and form an isosceles triangle, with vortex three located at the apex on the line $X = 0$. As discussed following Equation (5.32), the sign of Θ governs the existence of the various equilibria and singularities.

Point f: $\Gamma_3 = \frac{-1}{9}$

The phase plane corresponding to point **f**, with $\Gamma_3 = -\frac{1}{9}$, is shown in Figure 5.7. The dynamics for $\Theta < 0$ resemble those on the back face of the phase sphere, with periodic orbits surrounding the singularity $\mathcal{S}_{12}$. For $\Theta > 0$, the dynamics closely mirror those on the front face of the phase sphere in case **g** (see Figure 5.4). This configuration includes two stable equilateral equilibria and three unstable collinear equilibria, along with the singularities $\mathcal{S}_{13}$ and $\mathcal{S}_{23}$.

Point e: $\Gamma_3 = \frac{-1}{3}$

Point **e** lies on the circle $\gamma_2 = 0$ in Figure 5.1. This case is significant because, at this parameter value, solutions that collapse in finite time are observed. As this point

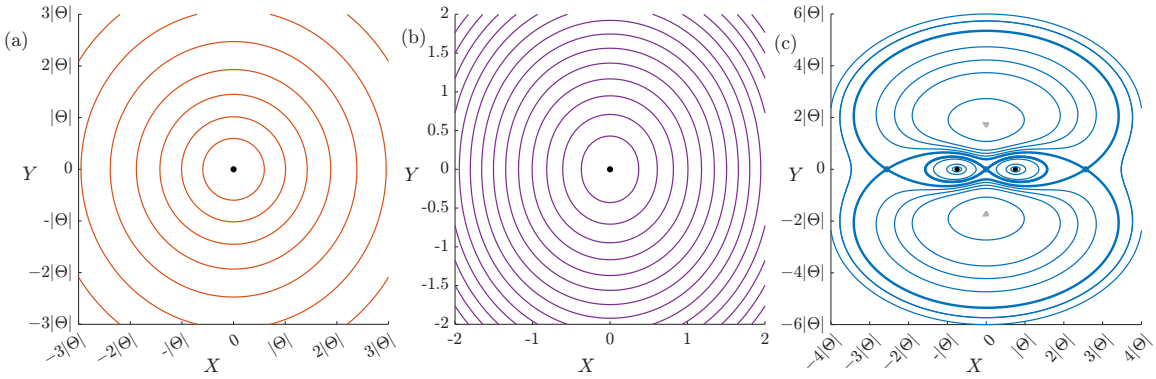

Figure 5.7 The XY phase planes in case **f** with $\Gamma_3 = \frac{-1}{9}$. (a) The case $\Theta < 0$. (b) The case $\Theta = 0$. (c) The case $\Theta > 0$. Markings are similar to the spherical case: Gray triangles mark the equilateral equilibria; black dots mark the singularities, and blue (or red) dots mark collinear equilibria.

is approached, the radius of the triangular equilibria diverges according to Equation (5.22), and their stability type undergoes a transformation as specified by Equation (5.27). Similarly, the two collinear equilibria $\mathcal{E}_1$ and $\mathcal{E}_2$ diverge, and their stability also undergoes a change. Consequently, precisely on this circle, the number of fixed points diminishes from five to one, with only the saddle point $\mathcal{E}_3$ remaining. This observation is corroborated by comparing the plot for $\Theta > 0$ in Figure 5.8.

Previous literature has established that $\gamma_2 = 0$ is a prerequisite for finite-time collapse [2, 20, 28]. This phenomenon occurs when $\Theta = 0$. At this value, the system exhibits unbounded trajectories. The Hamiltonian assumes a particularly straightforward form:

$$H = \frac{1}{9} \log \left(\frac{4Z^2 - 3X^2}{Z^2} \right). \tag{5.33}$$

Using Equation (5.17) with $\Theta = 0$ to eliminate Z and using polar coordinates for X and Y yields:

$$H = \frac{1}{9} \log \left(\frac{X^2 + 4Y^2}{X^2 + Y^2} \right) = \frac{1}{9} \log \left(5 - 3\cos 2\theta\right),$$

Since H is independent of r, the level sets of H are rays emanating from the origin. A brief calculation reveals that r evolves according to the differential equation:

$$\frac{\mathrm{d}r}{\mathrm{d}t} = \frac{2\sqrt{3}\sin(2\theta)}{3\cos(2\theta) - 5}.$$

Consequently, for (X, Y) in the first or third quadrant, $\frac{\mathrm{d}r}{\mathrm{d}t}$ is negative and constant. The solution converges to zero within a finite time while preserving a constant triangular shape. Similarly, in the second and fourth quadrants, the solution collapses into the origin in negative time. This provides the most elementary mathematical description of the observed phenomenon. The visual representation remains essentially unchanged, when $\Gamma_2 \neq \Gamma_1$, with the exception that the angles of the rays separating growing from decaying motions, for parameter combinations on the circle changes.

The $\Theta < 0$ phase surface is characterized by closed orbits surrounding the singularity $\mathcal{S}_3$. The $\Theta > 0$ phase surface contains a single equilibrium $\mathcal{E}_3$, from which emerge a pair of homoclinic orbits, each encircling the singularity $\mathcal{S}_1$ or $\mathcal{S}_2$.

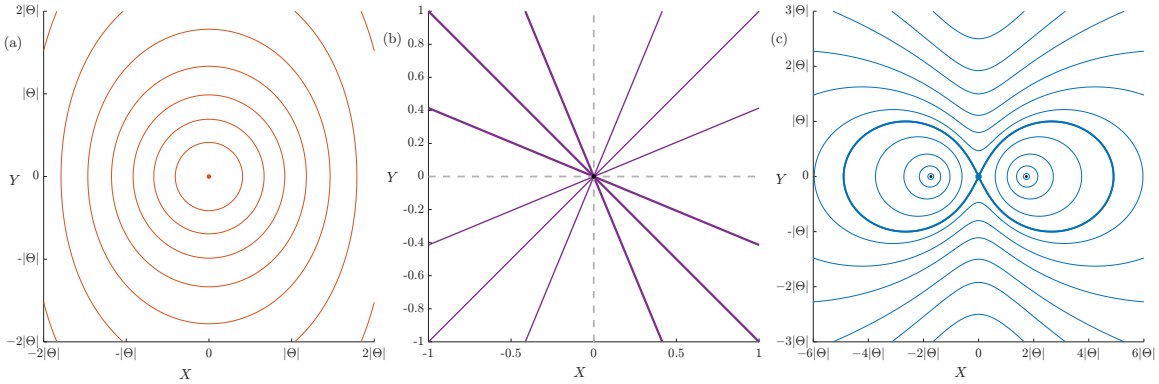

Figure 5.8 The XY phase planes in case **e** with $\Gamma_3 = \frac{-1}{3}$. The trajectories in the $\Theta = 0$ case are rays through the origin and correspond to triangles that shrink to zero in finite forward time (quadrants one and three), finite backward time (quadrants two and four), or do not change size (the X- and Y-axes).

Point d: $\Gamma_3 = \frac{-1}{2}$

As Γ_3 decreases past the critical value $\frac{-1}{3}$, four equilibria reappear from infinity and emerge on the phase surfaces for $\Theta < 0$, now with their stability types exchanged:

the two triangular configurations $\mathcal{E}_{\text{tri}}^{\pm}$ become saddles, while the collinear equilibria $\mathcal{E}_1$ and $\mathcal{E}_2$ become centers. The saddle points are connected by two distinct pairs of heteroclinic orbits. One pair encloses the singularity $\mathcal{S}_3$ at the origin, while the other, more extended pair, makes wide excursions around the collinear equilibria $\mathcal{E}_1$ and $\mathcal{E}_2$.

On the surface $\Theta = 0$, all trajectories are closed orbits. The $\Theta > 0$ phase surface remains unchanged from the previous configuration. However, interpreting the $\Theta < 0$ phase portrait requires some care. Two of the connections between the triangular saddles are long and stretch across a wide area of the phase surface. The left panel of Figure 5.9, these big arcs hide the smaller details: at this scale, the equilibria, singularities, and other curves are not clear. To see these details, Figure 5.10 shows a closer look at the important part, revealing the inner structure of the phase portrait.

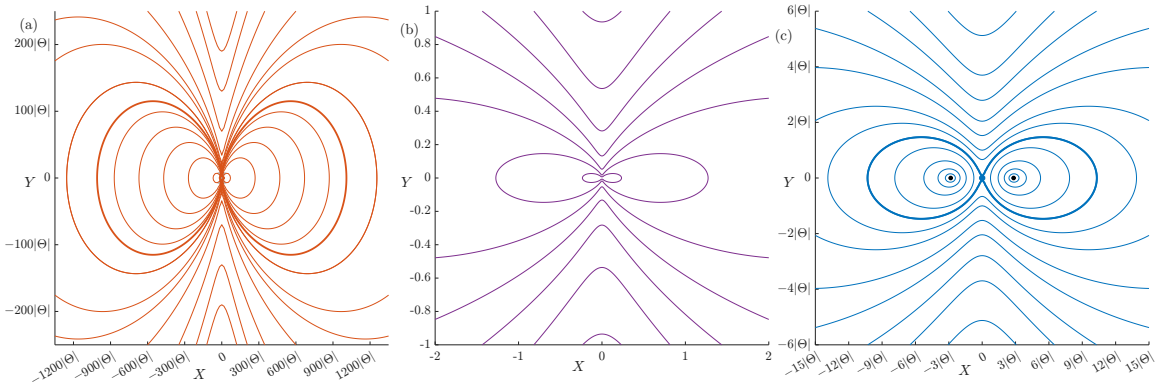

Figure 5.9 The XY phase planes of system in case **d** with $\Gamma_3 = \frac{-1}{2}$. The two equilibria $\mathcal{E}_1$ and $\mathcal{E}_2$ have moved to the $\Theta < 0$ surfaces and become centers. The two equilibria $\mathcal{E}_{\text{tri}}^{\pm}$ have returned to the $\Theta < 0$ surfaces but have become centers. A thicker curve denotes the larger loops of the heteroclinic orbits, but the smaller segments are invisible at this magnification. Therefore, we show a closeup of the left image in Figure 5.10.

Point c: $\Gamma_3 = -1$

As Γ_3 approaches -1, the collinear equilibria $\mathcal{E}_1$ and $\mathcal{E}_2$ diverge to $X = \pm\infty$, as do the singularities $\mathcal{S}_{13}$ and $\mathcal{S}_{23}$. At $\Gamma_3 = -1$, they all cease to exist. This is because at $\Gamma_3 = -1$, vortex 3 may form a dipole with either of the other two vortices. Since the

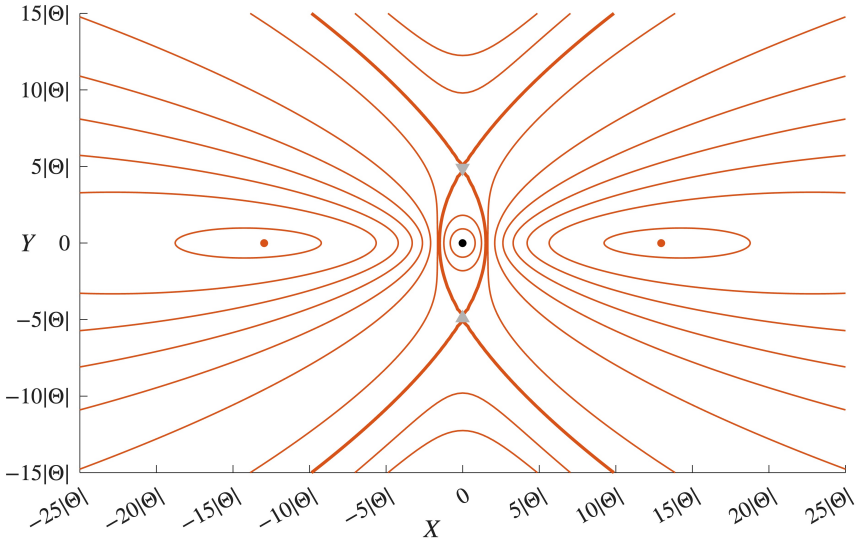

Figure 5.10 A closeup of the $\Theta < 0$ phase surface showing the singularities and equilibria as well as the smaller components of the heteroclinic curves.

total circulation of the two vortices forming the dipole vanishes, their joint center of vorticity sits at infinity.

This is the second case in which unbounded orbits exist. They correspond to orbits in which a vortex dipole scatters off a third, initially stationary vortex. We analyze the scattering dynamics when the third vortex has arbitrary circulation. This occurs for circulations along either of the dashed lines through point **c** in Figure 5.1. We will revisit this case in Section 6.2, where we provide a comprehensive explanation of this scattering phenomenon.

For this value of Γ_3, when $\Theta = 0$, the three vortices must always lie a the corners of a right triangle, a fact observed by Gröbli [20]. As such, the area formed by this triangle cannot vanish and $Y \neq 0$. Hence the X-axis is singular on this phase surface, as represented by the gray line in the center panel of Figure 5.11.

Point b: $\Gamma_3 = \frac{-3}{2}$

The phase surface for point **b** with $\Gamma_3 = \frac{-3}{2}$, shown in Figure 5.12 looks almost unchanged from the surface at point **d**, but there is one crucial difference. The

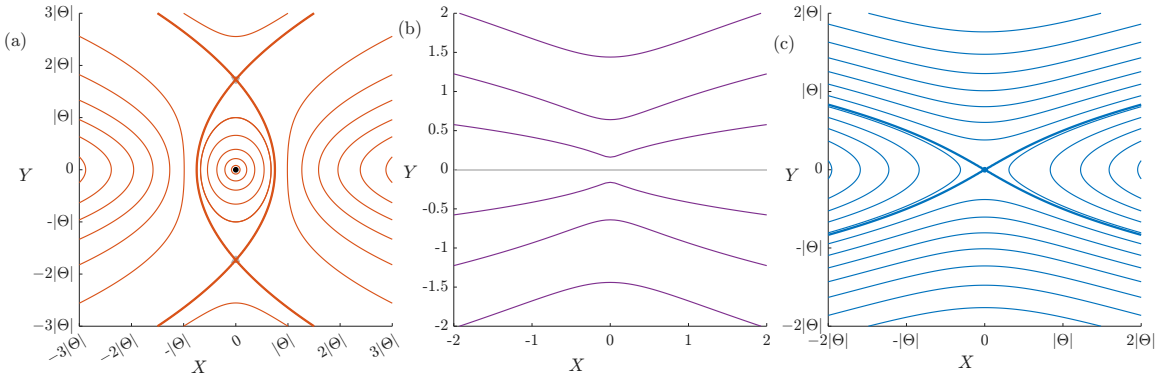

Figure 5.11 The XY phase planes for case **c** with $\Gamma_3 = -1$. (a) The case $\Theta < 0$ with singularity X_{12} at the origin and triangular configurations (X, Y, Z) at the intersections of the thick curves. (b) The case $\Theta = 0$. The gray line $Y = 0$ is singular. (c) The case $\Theta > 0$ with collinear equilibrium at the origin.

equilibria and singularities that diverged to infinity at point **c** have returned from infinity, only now the two singularities $\mathcal{S}_{13}$ and $\mathcal{S}_{23}$ lie on the $\Theta < 0$ surface and the collinear equilibria $\mathcal{E}_1$ and $\mathcal{E}_2$ lie on the $\Theta > 0$ surface.

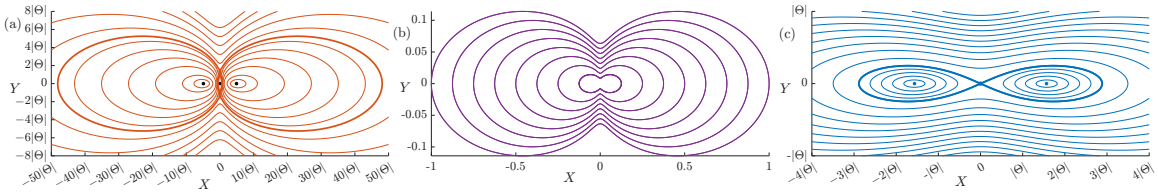

Figure 5.12 The XY phase planes of system in case **b** with $\Gamma_3 = \frac{-3}{2}$.

Point a: $\Gamma_3 = \frac{-17}{3}$

Finally, as Γ_3 is further decreased below $\Gamma_3 = \frac{-5}{3}$, where the deltoid has its cusp in Figure 5.1, to point **a**, the three collinear equilibria collide in a pitchfork bifurcation. Only $\mathcal{E}_3$ survives, changing from an unstable saddle to a stable center.

5.6 Three-Vortex Interactions with Vanishing Total Circulation

In this section, we will discuss the scenario where the sum of the circulations of three vortices is zero. In such cases, the final step of the Jacobi reduction cannot be applied if the total circulation is zero, and an alternative procedure is used. We can always

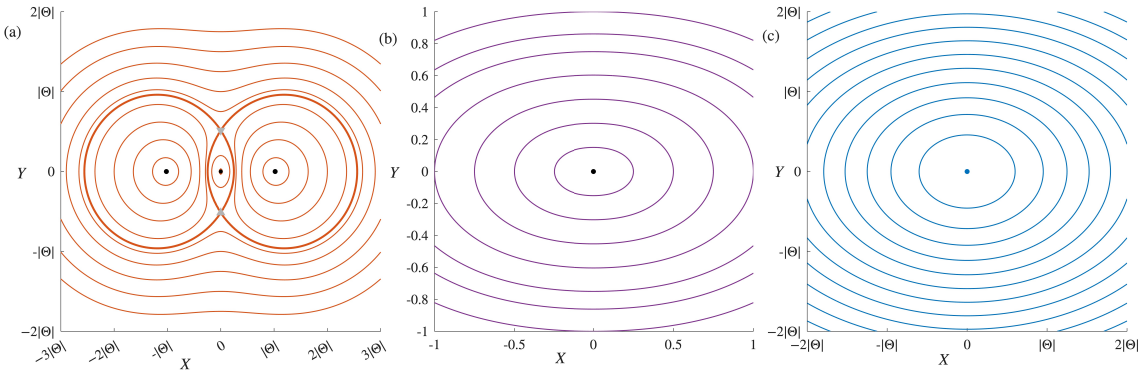

Figure 5.13 The XY phase planes in case **a** with $\alpha = \frac{-17}{3}$.

label the particle in such a way that the sequence of transformations works at each step except the last.

For the three-vortex problem with $\gamma_1 = 0$, or equivalently, $\Gamma_3 = -\Gamma_1 - \Gamma_2 \neq 0$. We perform the first step of the Jacobi reduction as before, arriving at system (4.2). However, the second recursive application of the Jacobi coordinate reduction leading to Equation (5.2) is no longer feasible. Instead, we apply the transformation (4.3) to the coordinates $\tilde{z}_2$ and $\tilde{z}_3$.

Without loss of generality, we may take $P_2 = 0$. If $P_3 \neq 0$, we may scale it to $P_3 = 1$ without loss of generality. Letting $Q_1 = X$ and $P_1 = Y$, ignoring additive constants, we obtain a Hamiltonian

$$\begin{aligned} H = &- \frac{\Gamma_1\Gamma_2}{2} \log\left(X^2 + Y^2\right) \\ &+ \frac{(\Gamma_1 + \Gamma_2)\,\Gamma_1}{2} \log\left((\Gamma_1 + \Gamma_2(X-1))^2 + \Gamma_2^2 Y^2\right) \\ &+ \frac{(\Gamma_1 + \Gamma_2)\,\Gamma_2}{2} \log\left((\Gamma_2 + \Gamma_1(X+1))^2 + \Gamma_1^2 Y^2\right). \end{aligned} \tag{5.34}$$

The three singularities occur at $Y = 0$ and

$$X_{12} = 0, \quad X_{13} = 1 - \frac{\Gamma_1}{\Gamma_2}, \quad X_{23} = -1 - \frac{\Gamma_2}{\Gamma_1}.$$

Rott and Aref independently derived this system through distinct methods that were considerably more difficult than the current derivation [5, 45]. Behring derived the equivalent system when $\Gamma_1 = \Gamma_2$ [9].

When $P_2 = P_3 = 0$, this reduces further to

$$H = \frac{\Gamma_1^2 + \Gamma_2\Gamma_1 + \Gamma_2^2}{2} \log\left(X^2 + Y^2\right), \tag{5.35}$$

again ignoring an additive constant.

The system described by Hamiltonian (5.34) exhibits equilateral relative equilibria at the following points:

$$\mathcal{E}_{\text{tri}}^{\pm} = \left(\frac{\Gamma_2^2 - \Gamma_1^2}{2\left(\Gamma_1^2 + \Gamma_2\Gamma_1 + \Gamma_2^2\right)}, \pm \frac{\sqrt{3}\left(\Gamma_1 + \Gamma_2\right)^2}{2\left(\Gamma_1^2 + \Gamma_2\Gamma_1 + \Gamma_2^2\right)} \right), \tag{5.36}$$

A standard computation demonstrates that these equilibria are saddles connected pairwise by heteroclinic orbits. One such phase plane is illustrated in Figure 5.14.

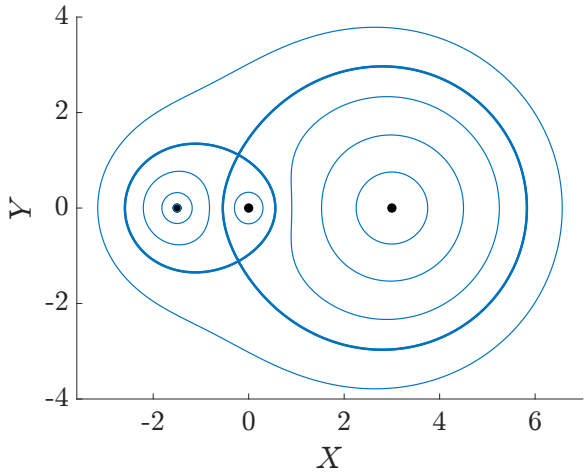

Figure 5.14 A phase plane exhibiting vanishing total circulation, $(\Gamma_1, \Gamma_2, \Gamma_3) = (2, 1, -3)$.

When $\Gamma_1 = \Gamma_2$, the formula simplifies considerably, but there are no bifurcations. Conversely, when $P_2 = 0$, the dynamics of Hamiltonian (5.35) exhibits a lone singularity at the origin, corresponding to a triple collision.

CHAPTER 6

SCATTERING IN A POINT-VORTEX MODEL

This chapter presents a detailed investigation into the dynamics and scattering behavior of a three-point vortex system with circulations $(1, 1, -1)$, as well as its generalization to asymmetric with circulations $(\Gamma, 1, -\Gamma), 0 < \Gamma \neq 1$. The approach integrates geometric reduction techniques, phase-space analysis, and scattering theory to explain governing vortex interactions.

In Section 6.1, we specify the reduction of previous sections to the symmetric case $(1, 1, -1)$. The four variables (X, Y, Z, Θ), each representing a crucial geometric aspect of the vortex configuration. These variables are reinterpreted in terms of the positions of the vortices, aided by a parallelogram construction that offers geometric insights.

Section 6.2 examines the phenomenon of vortex dipole scattering within the reduced system. By analyzing representative trajectories, two distinct scattering behaviors—*direct* and *exchange*—are identified. Parameter regimes corresponding to each behavior are characterized, with the *scattering angle* $\Delta\alpha$ serving as the primary observable. Plots of $\Delta\alpha$ as a function of the initial offset ρ reveal singular structures that signal transitions between the scattering regimes.

In Subsection 6.2.1, action-angle variables are introduced to recover angular information not captured by the initial set of reduced variables. Through a canonical transformation, the physical scattering angle is reconstructed from the reduced dynamics. An explicit expression for the rate of change of this angle is derived and integrated along scattering trajectories.

Subsection 6.3.2 focuses on the special case $\Theta = 0$, which marks the marks a change in the phase space topology. This degenerate case exhibits distinctive

geometric and dynamical characteristics, which are highlighted through a set of explicit solution examples.

The phase-space structure of the system is explored in Section 6.3. Trajectories in the (X, Y) plane are plotted for various fixed values of Θ, providing a visual representation of how the system's topology governs scattering dynamics and highlighting qualitative differences in behavior across parameter ranges.

Finally, Section 6.4 extends the analysis to asymmetric systems with circulations $(\Gamma, 1, -\Gamma)$, where $0 < \Gamma \neq 1$. In this generalized setting, the symmetry of the original problem is broken, and the possibility of exchange scattering is lost.

6.1 The Three-Vortex Problem with Circulations 1:1:-1

In this section, we reduce the general three-vortex system derived in Chapter 5 by setting

$$(\Gamma_1, \Gamma_2, \Gamma_3) = (1, 1, -1).$$

This transformation yields the following circulations:

$$\kappa_1 = \frac{1}{2}, \kappa_2 = -2, \kappa_3 = 1.$$

The Hamiltonian in Equation (5.18) reduces to

$$h = -\frac{1}{2}\log\left(Z + \Theta\right) + \frac{1}{2}\log\left(Z^2 - 4X^2\right). \tag{6.1}$$

and the angular impulse is given by Equation (5.17). The evolution equations are

$$\frac{\mathrm{d}X}{\mathrm{d}t} = -\frac{4X}{Z^2 - 4X^2}; \tag{6.2a}$$

$$\frac{\mathrm{d}Y}{\mathrm{d}t} = -\frac{1}{2(Z+\Theta)} + \frac{Z}{Z^2 - 4X^2}; \tag{6.2b}$$

$$\frac{\mathrm{d}Z}{\mathrm{d}t} = \frac{8XZ}{(Z^2 - 4X^2)^2}. \tag{6.2c}$$

It is worthwhile to relate the (X, Y, Z, Θ) coordinate system to the physical coordinates, providing a straightforward geometric interpretation. Consider Figure 6.1. By assumption (4.1), the center of vorticity is located at the origin. We denote the vector from the origin to vortex j as $\mathbf{v}_j$. Relation (4.1) implies that $\mathbf{v}_3 = \mathbf{v}_1 + \mathbf{v}_2$, resulting in the positions of the three vortices and the origin forming a parallelogram, as mentioned by Gröbli in [20]. We define ϕ as the angle between $\mathbf{v}_1$ and $\mathbf{v}_2$. Subsequently, we determine the coordinates of the vortices by following the sequence of transformations as:

$$\begin{aligned} X &= -\|\mathbf{v}_1\|^2 + \|\mathbf{v}_2\|^2; \\ Y &= 2\,(\mathbf{v}_1 \times \mathbf{v}_2) \cdot \mathbf{k} = 2\|\mathbf{v}_1\|\|\mathbf{v}_2\| \sin\phi; \\ Z &= \quad \|\mathbf{v}_1\|^2 + \|\mathbf{v}_2\|^2; \\ \Theta &= -2\,\mathbf{v}_1 \cdot \mathbf{v}_2 = -2\|\mathbf{v}_1\|\|\mathbf{v}_2\| \cos\phi. \end{aligned} \tag{6.3}$$

Several observations regarding these coordinates are as follows:

- X is the signed difference between the lengths of $\mathbf{v}_1$ and $\mathbf{v}_2$, and it vanishes when the triangle of vortices is isosceles.
- The three vortices are collinear when $Y = 0$, which is not a singularity of the coordinate system.
- For $\Theta = 0$, $\cos\phi = 0$, implying that at all times, the three vortices form a right triangle, with vortex 1 positioned at the right angle. Consequently, it is impossible for them to be collinear, ensuring that $Y \neq 0$. This conclusion can also be derived from the singularity of the Hamiltonian (6.1) when $\Theta = 0$.

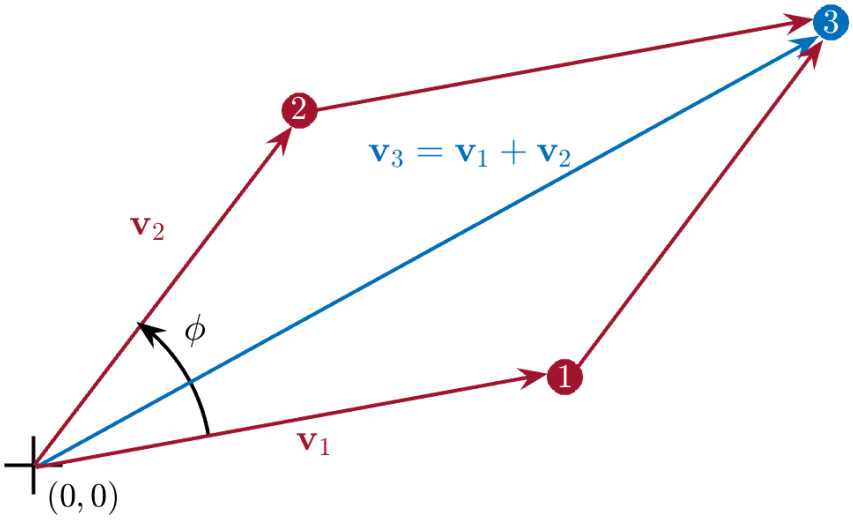

Figure 6.1 Diagram used to interpret the (X, Y, Z, Θ) coordinates. See the text for an explanation.

6.2 Scattering in a Point-Vortex Model

A *dipole* in the point vortex model refers to a system consisting of two vortices with equal magnitudes of circulation but opposite orientations. As shown in Subsection 3.3.2, the dipole moves at a constant velocity in a direction perpendicular to the line connecting the vortices, with a speed inversely proportional to the square of their separation distance.

The presence of a third vortex deflects or *scatters* of the dipole's motion, leading to two distinct types of scattering behavior:

- **Exchange Scattering:** In this scenario, the dipole that exits the interaction region is not composed of the same two vortices as the dipole that entered. This type of scattering involves a rearrangement of the vortices, where they exchange positions during the interaction.
- **Direct Scattering:** In contrast, direct scattering occurs when the same two vortices form the dipole before and after the interaction. In this case, the dipole maintains its original structure throughout the scattering process.

Three representative scattering solutions are shown in Figure 6.2. While these solutions satisfy similar initial conditions (as the time $t \to -\infty$), their behavior

as $t \to \infty$ differs significantly. Subfigures (a) and (b) illustrate examples of *exchange scattering*, whereas subfigure (c) depicts *direct scattering*.

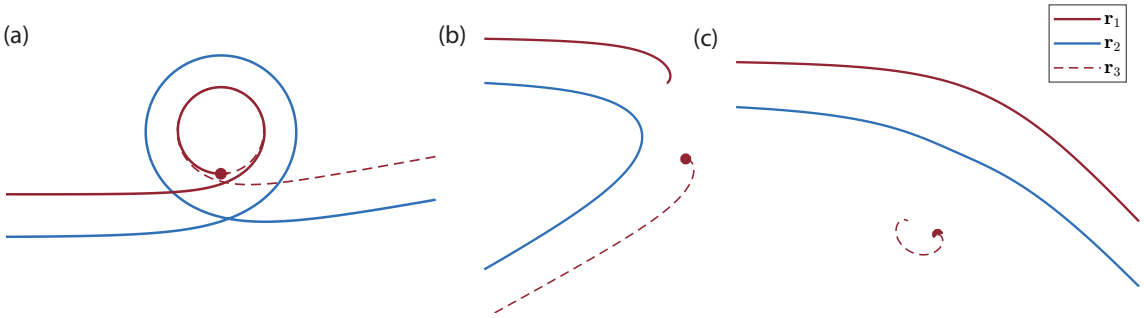

Figure 6.2 Three solutions of the scattering problem, illustrating (a) exchange scattering for $\rho = -0.999$, (b) exchange scattering for $\rho = 2.5$, and (c) direct scattering for $\rho = 3.8$. The vortex dipole originates from $-\infty$ and travels parallel to the x-axis. Vortex 3 remains stationary at the designated point as t approaches $-\infty$.

A central question in this scattering problem is whether a given initial configuration results in *direct* or *exchange* scattering. A related question concerns the change in orientation, $\Delta\alpha$, between the incoming and outgoing dipoles. Aref originally derived a formula addressing both aspects by integrating the governing ordinary differential equations, without relying on the phase diagram shown in Figure 1.1(b) [2]. However, Aref's plot of $\Delta\alpha$ as a function of initial conditions contained a sign error, which was later corrected by Lydon et al. [31].

The reduced system of equations permits a phase-space-based interpretation of the scattering process, which we briefly review here. A schematic of the scattering setup is shown in Figure 6.3.

A dipole, composed of a positive-circulation vortex at $\mathbf{r}_1 = \langle -L, \rho + \frac{1}{2} \rangle$ and a negative-circulation vortex at $\mathbf{r}_3 = \langle -L, \rho - \frac{1}{2} \rangle$, approaches from the left toward a stationary positive-circulation vortex located at $\mathbf{r}_2 = \langle 0, -1 \rangle$. These positions are chosen such that the center of vorticity satisfies, $\mathbf{r}_0 = 0$, and we take $d = 1$ without loss of generality. We refer to ρ as the scattering parameter.

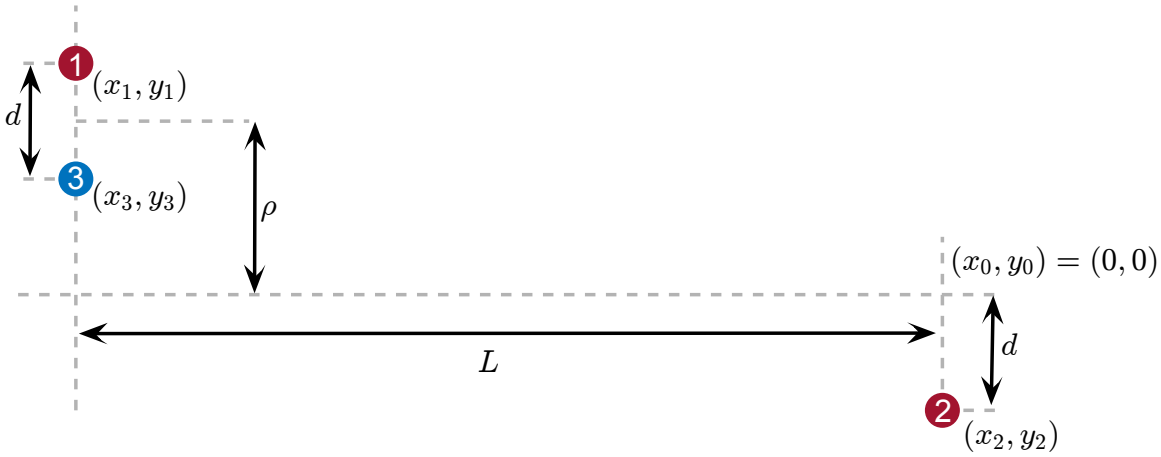

Figure 6.3 Setup of the scattering problem. The dipole formed by vortices 1 and 3 propagates toward the target, vortex 2.

Eventually, vortex 3 escapes to infinity, forming a new dipole. If the outgoing dipole consists of vortices 1 and 3, the scattering is classified as *direct*. If it consists of vortices 2 and 3, the event is classified as *exchange* scattering.

Examples of the two types of scattering are illustrated in Figure 6.2. The initial conditions follow the schematic setup, with exchange scattering demonstrated in panels (a) and (b), and direct scattering shown in panel (c). Since vortex 3 has circulation opposite to that of the other two vortices, it must be part of both the incoming and outgoing dipoles.

We define the *scattering angle* $\Delta\alpha$ as the change in heading of vortex 3; see Equation (6.7). The dependence of $\Delta\alpha$ on the initial offset ρ is plotted in Figure 6.4, with the points corresponding to the three examples in Figure 6.2 indicated.

For large offsets, $|\rho| \gg 1$, the interaction with the stationary vortex is weak, and the dipole is only slightly deflected, resulting in direct scattering. The figure confirms, as have shown that *exchange scattering* occurs within the interval $-1 < \rho < \frac{7}{2}$, and *direct scattering* occurs outside this interval. The values $\rho = -1$ and $\rho = \frac{7}{2}$ mark sharp transitions between scattering regimes. As ρ approaches either of these boundaries, the scattering angle $\Delta\alpha$ diverges [2, 31].

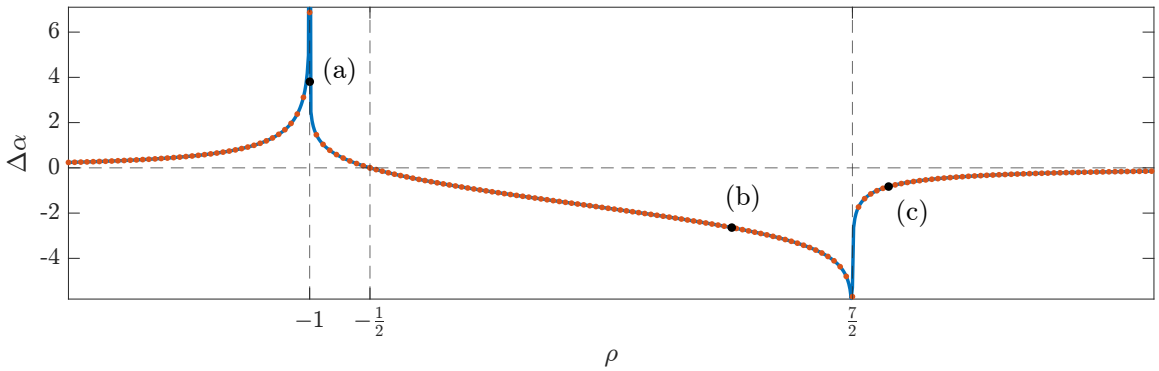

Figure 6.4 The deflection of the angle of vortex 3 plotted as a function of the distance ρ, revealing singularities at $\rho = -1$ and $\rho = \frac{7}{2}$, as anticipated. The solid line represents the outcome of direct simulation, while the red dots correspond to the formulas derived in Appendix A. The points marked (a)–(c) correspond to the three simulations shown in Figure 6.2.

6.2.1 Recovering some angles

In this section, we introduce action-angle variables to recover angular information that is lost in the previous formulation.

Equation (6.3) demonstrates that the variables (X, Y, Z, Θ) are invariant under rigid rotations of the parallelogram shown in Figure 6.1 about the origin. As such, they do not capture the *scattering angle*, which depends on the absolute orientation of the system. To remedy this, we introduce a canonical form of polar coordinates—namely, the action-angle variables of a harmonic oscillator—which allow us to recover this missing angular degree of freedom.

The generalized Hamiltonian obtained in the Equation (5.3) can be further simplified. We normalize the system using Equation (3.9) and the values of κ_j from Equation (5.2), resulting in

$$\begin{aligned} Q_1 &= \frac{1}{\sqrt{2}} X_1, \quad P_1 = \frac{1}{\sqrt{2}} Y_1, \\ Q_2 &= \sqrt{2} X_2, \quad P_2 = -\sqrt{2} Y_2. \end{aligned} \tag{6.4}$$

Defining $\mathcal{R}_i = \langle Q_i, P_i \rangle$ and $\bar{\mathcal{R}}_i = \langle Q_i, -P_i \rangle$, the conserved quantities become (up to an additive constant)

$$H = -\frac{1}{2}\log \|\mathcal{R}_1\|^2 + \frac{1}{2}\log \left\|\mathcal{R}_1 + \bar{\mathcal{R}}_2\right\|^2 + \frac{1}{2}\log \left\|\mathcal{R}_1 - \bar{\mathcal{R}}_2\right\|^2, \tag{6.5}$$

and

$$\Theta = \|\mathcal{R}_1\|^2 - \|\mathcal{R}_2\|^2. \tag{6.6}$$

We express the coordinates $\mathcal{R}_1$ and $\mathcal{R}_2$ in polar form as:

$$\mathcal{R}_1 = \begin{pmatrix} \sqrt{2I_1}\sin\theta_1 \\ \sqrt{2I_1}\cos\theta_1 \end{pmatrix}, \quad \mathcal{R}_2 = \begin{pmatrix} \sqrt{2I_2}\sin\theta_2 \\ \sqrt{2I_2}\cos\theta_2 \end{pmatrix}.$$

Two observations are important here. First, the Hamiltonian depends on the angles only through the combination $\theta_1+\theta_2$. Second, the vector $\mathbf{v}_3$ in the figure has argument $\theta_2 - \frac{\pi}{2}$. Therefore, we make one additional canonical transformation

$$\psi_1 = \theta_1 + \theta_2, \quad \psi_2 = \theta_2, \quad J_1 = I_1, \quad J_2 = I_2 - I_1.$$

In these variables, the Hamiltonian takes the form (again disregarding additive constants):

$$H = \frac{1}{2}\log\left(4J_1^2\sin^2\psi_1 + 4J_1J_2\sin^2\psi_1 + J_2^2\right) - \frac{1}{2}\log(J_1).$$

Since the equation is cyclic in ψ_2, the action $J_2 = -\Theta/2$ is conserved. The dynamics of J_1 and ψ_1 are equivalent to system (6.2). We may recover the evolution of $\theta_2 = \psi_2$ by integrating

$$\dot{\psi}_2 = \frac{2J_1\sin^2\psi_1 + J_2}{4J_1^2\sin^2\psi_1 + 4J_1J_2\sin^2\psi_1 + J_2^2}$$

along a scattering trajectory.

In terms of the variables defined in Equation (6.3), this becomes

$$\dot{\theta}_2 = \frac{2Y^2\sqrt{\Theta^2 + X^2 + Y^2} - 2\Theta X^2}{(X^2 + Y^2)(\Theta^2 + Y^2)}.$$

The angle just calculated describes the argument of $\mathbf{v}_3$ in Figure 6.1, which is distinct from the scattering angle $\alpha = \arg\left(\frac{\mathrm{d}z_3}{\mathrm{d}t}\right)$ plotted in Figure 6.4.

In terms of the reduced coordinates, we find that

$$\frac{\mathrm{d}\alpha}{\mathrm{d}t} = -\frac{8\Theta Y^2}{(X^2 + Y^2)(\Theta^2 + Y^2)}. \tag{6.7}$$

Integrating this over a trajectory then gives $\Delta\alpha$. This calculation is described in Appendix A. It is equivalent to a calculation by Lydon [31].

6.3 Phase Space and Scattering Analysis for the System with Circulations 1:1:-1

We first derive the fixed points and singularities of system (6.2) before visualizing the system's phase space. We set the right-hand sides of system (6.2) to zero while enforcing the constraints (5.17) and $Z \geq 0$. Similarly, we find singularities where the argument of either logarithmic term in the Hamiltonian (6.1) vanishes, enforcing the same two constraints. Which equilibria and singularities exist depends on Θ. Referring to Equations (5.21) and (5.22), we can determine the singularities and equilibria in this case.

When $\Theta < 0$, the system has two equilibria $\mathcal{E}^{\pm}_{\text{tri}}$ and a singularity $\mathcal{S}_{12}$ found by setting $Z + \Theta = 0$, which requires $X = Y = 0$. These are

$$\mathcal{E}^{\pm}_{\text{tri}} = \begin{pmatrix} 0 \\ \pm\frac{\sqrt{3}}{2}\Theta \\ -2\Theta \end{pmatrix} \quad \text{and} \quad \mathcal{S}_{12} = \begin{pmatrix} 0 \\ 0 \\ -\Theta \end{pmatrix}.$$

When $\Theta = 0$, there are no equilibria, but the system is singular when $Z = |X|$, which requires $Y = 0$. When $\Theta > 0$, the system has a single equilibrium

$$\mathcal{E}_3 \equiv \begin{pmatrix} X_0 \\ Y_0 \\ Z_0 \end{pmatrix} = \begin{pmatrix} 0 \\ 0 \\ \Theta \end{pmatrix}$$

and no singularities.

For both equilibria $X = 0$ implies $\|\mathbf{v}_1\| = \|\mathbf{v}_2\|$. The equilibrium $\mathcal{E}^{\pm}_{\text{tri}}$ exists for $\Theta < 0$. For the equilibrium $\mathcal{E}^{\pm}_{\text{tri}}$, the value of the component $Z = -2\Theta$ implies that $\phi = \pm\frac{\pi}{3}$ and the three vortices lie at the vertices of an equilateral triangle, motivating the naming convention. The equilibrium $\mathcal{E}_3$ exists for $\Theta > 0$. This implies $\phi = \pi$ so that the three vortices are collinear with the two positive vortices equally spaced from the negative vortex at the center. The subscript -1 indicates that the vortex with circulation -1 sits at the center. By similar reasoning, we find that at the singularity $\mathcal{S}_{12}$, the two vortices with circulation $+1$ coincide, again motivating the notation.

By the conservation law (5.17), the phase space of system is the upper sheet of a two-sheeted hyperbola. We visualize the dynamics by projecting this surface into the XY plane in Figure 6.5. The conserved angular impulse Θ is a bifurcation parameter, but up to scaling when $\Theta \neq 0$, there are only three possible phase planes.

For $\Theta < 0$ in panel (a), the point at the origin is the singularity $\mathcal{S}_{12}$. The two equilibria $\mathcal{E}^{\pm}_{\text{tri}}$ sit on the Y axis and are saddle points connected by a pair of homoclinic orbits. The two homoclines surround a family of periodic orbits, which shrink to a point at $\mathcal{S}_{12}$. Each corresponds to a hierarchical orbit in which the two positive vortices orbit about each other rapidly while their mutual center of vorticity and the third vortex orbit each other; Gröbli computed this orbit in closed form and plotted it in Gröbli [[20], Figure 1]. As the diameter of these closed orbits goes to zero, the rotation rate of this tightly bound pair diverges, and the orbits approach

the singularity $\mathcal{S}_{12}$. The unbounded portions of the stable and unstable manifolds separate the remainder of the phase plane into four unbounded quadrants. This will be important for the scattering problem.

When $\Theta = 0$ in panel (b), the entire X axis is singular, and all solutions are confined to the upper or lower half-planes. For $\Theta > 0$ in panel (c), the collinear equilibrium $\mathcal{E}_3$ at the origin is a saddle point. Its invariant manifolds also separate the plane into four unbounded quadrants.

The phase plane for $\Theta < 0$ in panel (a) corresponds to the upper disconnected component of $\mathcal{D}_{\text{phys}}$ in Figure 1.1(b), the phase plane for $\Theta = 0$ in panel (b) to Figure 1.1(c), and phase plane for $\Theta > 0$ in panel (c) to the lower disconnected component of $\mathcal{D}_{\text{phys}}$ in Figure 1.1(b).

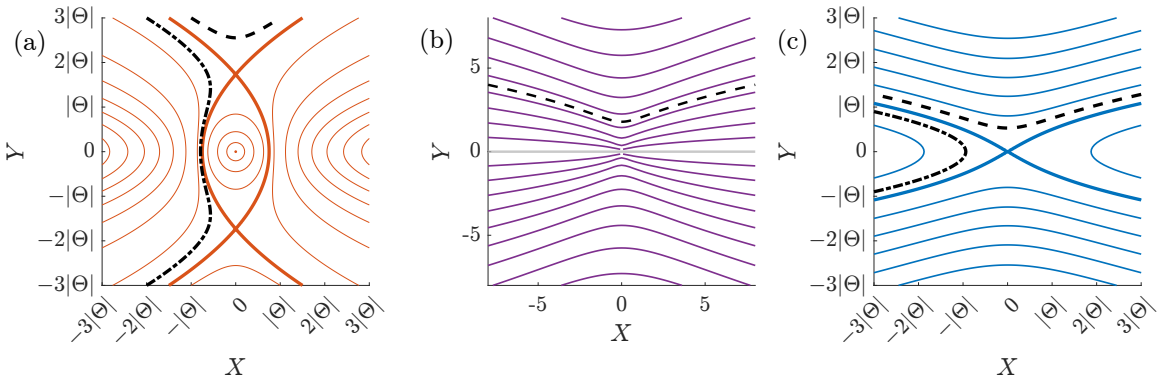

Figure 6.5 The XY phase planes of system (6.2). (a) The case $\Theta < 0$ with singularity $\mathcal{S}_{12}$ (point) and triangular configurations at the intersections of the thick curves. (b) The case $\Theta = 0$. The gray line $Y = 0$ is singular. (c) the case $\Theta > 0$ with collinear equilibrium $\mathcal{E}_3$. Note that the contours are not evenly-spaced level sets of the energy (6.1) but were chosen to illustrate the topology clearly.

Finally, note that rescaling X and Y by $|\Theta|$ and t by $|\Theta|^{-1}$ (when $\Theta \neq 0$) shows that the dynamics for any negative (respectively, positive) value of Θ has a phase plane equivalent to that shown in panel (a) (respectively, panel (c)).

6.3.1 Explaining the scattering

In this section, we explain the behavior of the three-vortex scattering problem depicted in Figure 6.3. In the vortex system, the most probable explanation for

the transition from direct scattering to exchange scattering and back at $\rho = -1$ and $\rho = \frac{7}{2}$, and the divergence of the scattering angle near these points, appears to hinge on the crossing of separatrices.

The separatrices shown in Figure 6.5 divide the phase plane into families of trajectories with identical topology, and the topology of the phase plane is determined, in turn, by the conserved parameter Θ. Panel (a) depicts the case $\Theta < 0$, where the energy level of the separatrices equals that of the rotating triangular configurations $\mathcal{E}_{\text{tri}}^{\pm}$, given by

$$E(\mathcal{E}_{\text{tri}}^{\pm}) = \frac{1}{2}\log(-4\Theta). \tag{6.8}$$

The energy in the two regions to the left and right of $\mathcal{E}_{\text{tri}}^{\pm}$ (those containing the X-axis) is lower than $E(\mathcal{E}_3)$, while the energy in the regions above and below the separatrices is higher than $E(\mathcal{E}_{\text{tri}}^{\pm})$.

Panel (c) illustrates the scenario where $\Theta > 0$. In this case, the energy levels of the separatrices are equal to that of the collinear equilibrium $\mathcal{E}_3$, which we calculate to be

$$E(\mathcal{E}_3) = \frac{1}{2}\log\frac{\Theta}{2}. \tag{6.9}$$

The energy in the two regions to the left and right of $\mathcal{E}_3$ (those containing the X-axis) is lower than $E(\mathcal{E}_3)$, while the energy in the regions above and below the separatrices is higher than $E(\mathcal{E}_3)$.

We must compare these energies with those of the pre-scattering condition depicted in Figure 6.3. In this arrangement, the center of vorticity is at the origin, allowing us to compute the limiting behavior of X and Y using the equations in (6.3). We directly compute that, regardless of L,

$$\Theta = 1 + 2\rho. \tag{6.10}$$

We assume that as $t \to -\infty$, $L \to \infty$, so $\|\mathbf{v}_1\| \to \infty$ while $\|\mathbf{v}_2\|$ remains finite. Consequently, $X \to -\infty$, and this implies that $Y \to \infty$. Therefore, for the situation depicted in Figure 6.3, trajectories in the phase planes depicted in Figure 6.5 originate from infinity in the northwest direction and head southeast.

Suppose the initial energy exceeds the separatrix energy. In that case, the trajectory begins above the separatrix and crosses the Y-axis, where $\frac{\mathrm{d}Y}{\mathrm{d}t} = 0$, before escaping to infinity in the northeast direction. Since $X \to +\infty$ as $t \to \infty$, $\|\mathbf{v}_2\|$ must diverge, indicating an exchange scattering event. At the instant the solution crosses $X = 0$, $\|\mathbf{v}_1\| = \|\mathbf{v}_2\|$, and the vectors $\mathbf{v}_1$ and $\mathbf{v}_2$ form the legs of an isosceles triangle.

If, instead, the initial energy lies below the separatrix energy, the trajectory begins below the separatrix. It crosses the X-axis at which point $\frac{\mathrm{d}X}{\mathrm{d}t} = 0$. When $Y = 0$, $\sin\phi = 0$, and the three vortices are collinear. Since $X < 0$ along the entire trajectory and $X \to \infty$ as $t \to \infty$, $\|\mathbf{v}_1\| \to \infty$, and this solution represents a direct scattering event.

For $\Theta < 0$, or equivalently, for $\rho < -\frac{1}{2}$, the critical energy is given by Equation (6.8). Combining this with Equation (6.10) yields a critical scattering parameter:

$$\rho_{\text{crit}}^{-} = -1. \tag{6.11}$$

For $\Theta > 0$, or equivalently, for $\rho > -\frac{1}{2}$, the critical energy is given by Equation (6.9). Combining this with Equation (6.10), we obtain a critical scattering parameter:

$$\rho_{\text{crit}}^{+} = \frac{7}{2}. \tag{6.12}$$

Figure 6.4 illustrates the deflection in the angle of vortex 3 following the interaction becomes singular as $\rho \to -1$ and $\rho \to \frac{7}{2}$, as expected.

To calculate the scattering angle, we need to integrate Equation (6.7) over each scattering trajectory. This calculation is equivalent to that performed by Lydon et al. [31], and we defer it to Appendix A.

We conclude this section by noting that the values $\rho = 1$ ($\Theta = -1$), $\rho = -\frac{1}{2}$ ($\Theta = 0$), and $\rho = \frac{7}{2}$ ($\Theta = 8$) divide the space of initial conditions into four distinct intervals. Gröbli made a similar observation (using a constant $\lambda = \frac{\Theta}{2}$) as did Lydon et al. [20, 31], but without explicitly referring to a phase plane to organize the orbits. Both prior works focus on integrating the ODE system by quadrature, so these intervals are primarily distinguished by the change in the algebraic forms of the integrals rather than the phase space topology.

The approach presented here is particularly illuminating for the transition at $\Theta = 0$, where there is an algebraic change in the form of the integrals but no visible discontinuity in the scattering angle as depicted in Figure 6.4. We will discuss this further in the next section.

6.3.2 The borderline case $\Theta = 0$

In this section, we will examine the case where $\Theta = 0$. Evidently, the critical values of ρ that separates exchange scattering from direct scattering are those for which the initial condition's energy, as L approaches infinity, equals that of the separatrices, i.e., the energy of the hyperbolic fixed points. From Equation (6.10), we observe

$$\Theta > 0 \quad \text{for} \quad \rho > -\frac{1}{2} \quad \text{and} \quad \Theta < 0 \quad \text{for} \quad \rho < -\frac{1}{2}. \tag{6.13}$$

The singular case $\Theta = 0$, where the conservation law (6.3) confines the dynamics to a cone, corresponds to $\rho = -\frac{1}{2}$. The schematic in Figure 6.3, which is defined for finite L, is somewhat misleading, as the trajectories of all three vortices lie along straight lines parallel to the line connecting vortices 2 and 3 in the figure and are not horizontal. Rotating the coordinate system so that the trajectories are horizontal, we

find that

$$x_1 = \frac{t - \sqrt{t^2+4}}{2}, \qquad x_2 = \frac{t + \sqrt{t^2+4}}{2}, \qquad x_3 = t;$$
$$y_1 = -1, \qquad y_2 = -1, \qquad y_3 = -2.$$

The dynamics of this case are depicted in Figure 6.6 and were previously known to Gröbli [20]. Vortex 1 slows down and comes to rest at $x = 0$, transferring its energy to vortex 2.

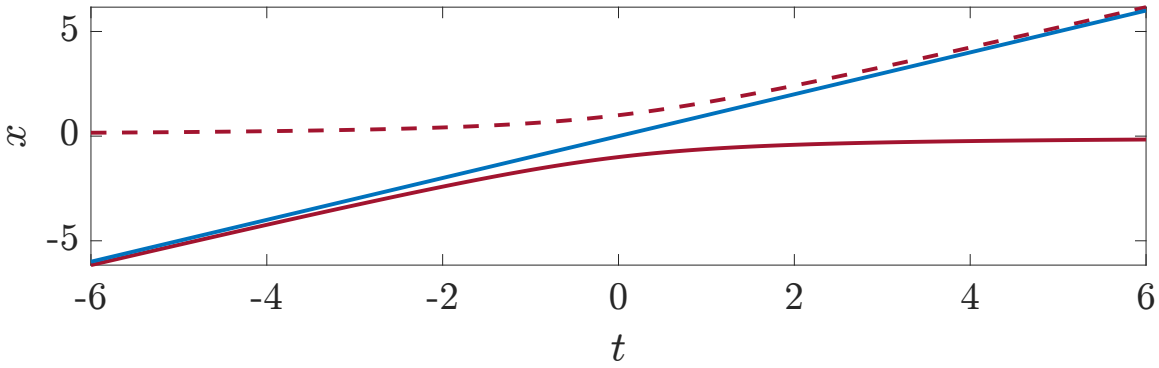

Figure 6.6 The x-component of the solution for $\rho = 0$, corresponding to a trajectory in the middle phase plane of Figure 6.5.

6.4 Vortex-Dipole Scattering with More General Circulations

In this section, we will generalize to the case in which

$$\Gamma_1 = -\Gamma_3 = \Gamma, \quad \text{and} \quad \Gamma_2 = 1, \quad \text{with } 0 < \Gamma \neq 1. \tag{6.14}$$

In this case, exchange scattering is no longer possible since vortices 2 and 3 can no longer form a dipole and escape.

Consequently, some bifurcation must reconfigure the phase plane dynamics depicted in Figure 6.5. Referring back to the Jacobi coordinate reduction defined

in the Equation (5.2) yields transformed circulations

$$\kappa_1 = \frac{\Gamma}{1+\Gamma}, \quad \kappa_2 = -\Gamma(1+\Gamma), \quad \kappa_3 = 1.$$

In this instance, $\kappa_2 < 0$. The Hamiltonian defined in Chapter 5 by Equation (5.18) for the vortex circulations $(\Gamma, 1, -\Gamma)$ is now expressed as

$$\begin{aligned} h(X,Y,Z,\Theta) =& \frac{\Gamma}{2}\log\big(Z(\Gamma^2+1) - (1-\Gamma^2)\Theta - 4\Gamma^2 X\big) \\ & - \frac{\Gamma}{2}\log(Z+\Theta) + \frac{\Gamma^2}{2}\log(2Z+4X\Gamma). \end{aligned}$$

6.4.1 Singularities and equilibria

In this section, we write down the singularities and fixed points derived in Chapter 5 for circulation satisfying (6.14). Since the sum of circulations of vortex 1 and 3 is zero, the equilibria that we obtain from the Equations (5.22) and (5.32) are

$$\mathcal{E}^{\pm}_{\text{tri}} = \Theta \begin{pmatrix} \frac{(1-\Gamma)}{2\Gamma^2(\Gamma+1)} \\ \pm\frac{\sqrt{3}}{2\Gamma^2} \end{pmatrix}, \text{ for } \Theta < 0; \tag{6.15a}$$

$$\mathcal{E}_{-\Gamma} = \frac{\Theta}{2\Gamma^2(\Gamma^2-1)} \begin{pmatrix} 2-\Gamma^2+\Gamma\sqrt{4-3\Gamma^2} \\ 0 \end{pmatrix}, \text{ for } \Theta > 0 \text{ and } \Gamma > \frac{2}{\sqrt{3}}; \tag{6.15b}$$

$$\mathcal{E}_{1} = \frac{\Theta}{2\Gamma^2(\Gamma^2-1)} \begin{pmatrix} 2-\Gamma^2-\Gamma\sqrt{4-3\Gamma^2} \\ 0 \end{pmatrix}, \text{ for } \Theta > 0 \text{ and } 1 < \Gamma < \frac{2}{\sqrt{3}}; \tag{6.15c}$$

$$\mathcal{E}_{\Gamma} = \frac{\Theta}{2\Gamma^2(\Gamma^2-1)} \begin{pmatrix} 2-\Gamma^2-\Gamma\sqrt{4-3\Gamma^2} \\ 0 \end{pmatrix}, \text{ for } \Theta < 0 \text{ and } \Gamma < 1. \tag{6.15d}$$

These final two equilibria are governed by the same mathematical expression but correspond to distinct vortex configurations. They are valid for different sets of parameter values. Only the X and Y coordinates are shown; the Z coordinate satisfies

the Equation (5.17). Using Equation (5.21), this system also has singularities at

$$\begin{aligned}\mathcal{S}_{12} &= (0, 0, -\Theta)\,, \text{ for } \Theta < 0 \text{ and } \Gamma > 0;\\ \mathcal{S}_{23} &= \left(\frac{\Theta}{(1-\Gamma^2)}, 0, \frac{(1+\Gamma^2)\Theta}{(1-\Gamma^2)}\right), \text{ for } \Theta(1-\Gamma) > 0.\end{aligned} \tag{6.16}$$

The equilibria and singularities of the system are most effectively visualized using a bifurcation diagram, shown in Figure 6.7. Based on this diagram, we can make some key observations.

- **For $\Gamma = 1$:** The equilibria $\mathcal{E}^{\pm}_{\text{tri}}$ and $\mathcal{E}_{-\Gamma}$, along with the singularity $\mathcal{S}_{12}$, are present.
- **Divergence behavior near $\Gamma = \pm 1$:** All other equilibria and singularities lie on the plane $Y = 0$ and diverge with $X \to +\infty$ as $\Gamma \to \pm 1$. In particular, the points $\mathcal{S}_{23}$, $\mathcal{E}_1$, and $\mathcal{E}_\Gamma$ diverge to infinity as $\Gamma \to 1^{\pm}$.
- **Bifurcation structure:** A saddle-node bifurcation occurs at the critical value $\Gamma = \frac{2}{\sqrt{3}}$, where the equilibria $\mathcal{E}_{-\Gamma}$ and $\mathcal{E}_\Gamma$ coalesce and annihilate.

6.4.2 Phase plane analysis when $\Gamma \neq 1$

In this section, we analyze the structure of the phase space as the parameter Γ varies, focusing on the projection of the upper sheet of the hyperboloid onto the XY plane. Throughout this analysis, we assume $\Gamma \neq 1$, which corresponds to the absence of exchange scattering. The objective of this phase plane analysis is to understand the dynamical behavior that emerges in place of exchange scattering when $\Gamma \neq 1$.

Point a: $\Gamma = \frac{10}{17}$

First, we show the case $\Gamma < 1$ as shown in Figure 6.8. For $\Theta < 0$, a collinear state $\mathcal{E}_1$ appears on the X-axis to the right of the region of closed orbits seen in Figure 6.5, while for $\Theta > 0$ a new singular state $\mathcal{S}_{23}$ appears on the positive X-axis.

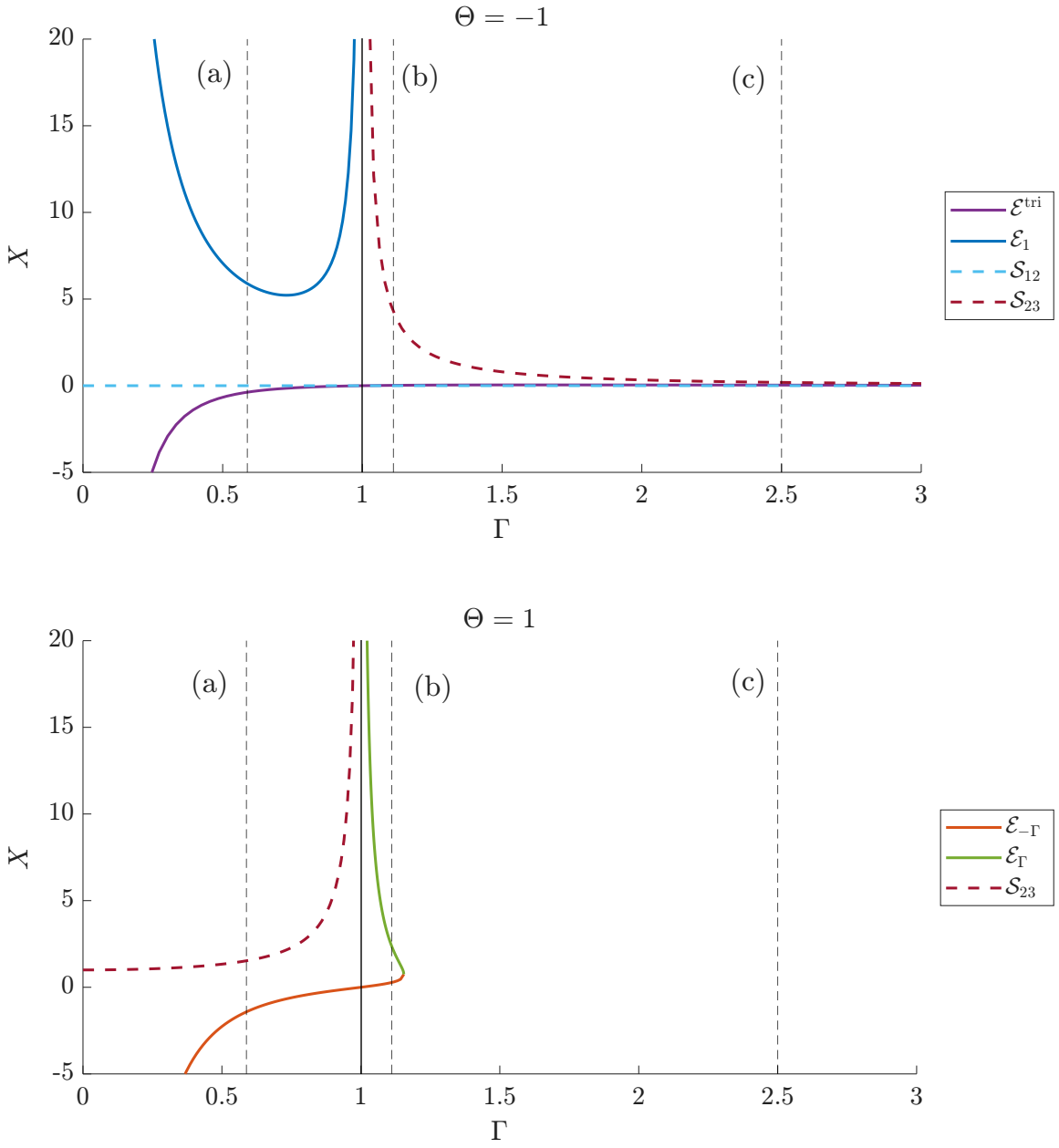

Figure 6.7 The X component of the equilibria (solid lines) and singularities (dashed lines) given in Equations (6.15) and (6.16). Figures 6.5, 6.8, 6.10 and 6.11 show phase plane diagrams at the Γ values indicated by the vertical lines.

Each of these are surrounded by a family of periodic orbits that limit to a separatrix. In contrast with Figure 6.5, all orbits in the right half plane cross the X-axis and do not extend to ∞.

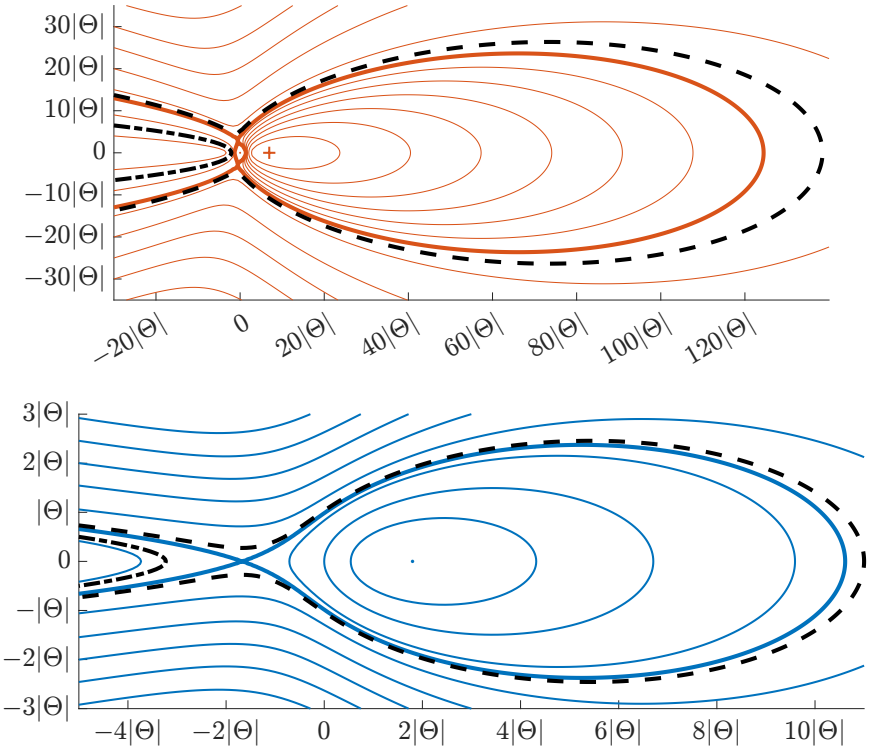

Figure 6.8 The phase planes for $\Gamma = \frac{10}{17} < 1$. Top: $\Theta < 0$ case showing the equilibria $\mathcal{E}^{\pm}_{\text{tri}}$ at the separatrix intersections, the singular point $\mathcal{S}_{12}$ (point) and the collinear state $\mathcal{E}_1$ (+). Bottom: $\Theta > 0$ case with singular point $\mathcal{S}_{23}$ (point) and collinear state $\mathcal{E}_{-\Gamma}$ at the separatrix intersection.

The family of unbounded orbits corresponding to exchange scattering is replaced by a new class of trajectories that cross the X-axis and extend toward infinity in a southwest direction. We refer to as *extended direct scattering orbits*. An example with $\Gamma = 2$ is shown in Figure 6.9. Notably, the coordinates of this trajectory, but not its time-parameterization, are provided by Gröbli and are presented in the dissertation [20, Equations (7.17), (7.19), and (7.20), and Figure 5].

As $t \to \pm\infty$, vortices 1 and 3 form a dipole that moves along a nearly straight trajectory. In contrast, vortex 2, for a finite duration, has switched partners with vortex 3, forming a dipole with vortex 2 and moving along a nearly circular orbit.

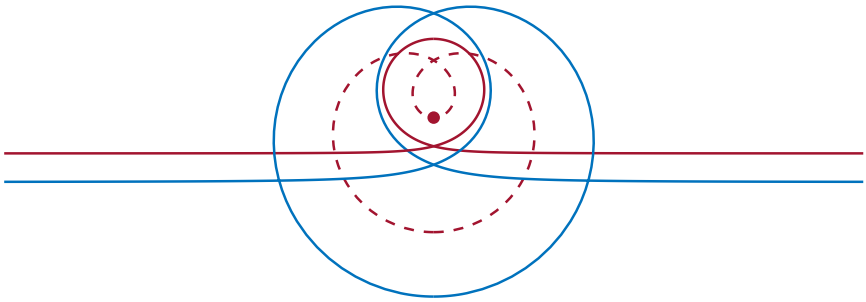

Figure 6.9 An extended direct scattering solution with $\Gamma = 2$ and $\rho = -\frac{9}{2}$. This is a direct simulation of a solution whose trajectory Gröbli computed in closed form.

Point b: $\Gamma = \frac{10}{9} \in \left(1, \frac{2}{\sqrt{3}}\right)$

In this regime, where $1 < \Gamma < \frac{2}{\sqrt{3}}$, the system exhibits qualitative changes in the phase portrait structure. While the overall topology remains similar to that in earlier cases, the nature of the singularities and fixed points evolves with Γ. Figure 6.10 presents representative phase portraits for the case $1 < \Gamma < \frac{2}{\sqrt{3}}$.

For $\Theta < 0$, the singularity $\mathcal{S}_{12}$ remains unchanged from Figure 6.8; however, the fixed point $\mathcal{E}_1$ located to the right of the origin is now replaced by the singularity $\mathcal{S}_{23}$.

In contrast, for $\Theta > 0$, the fixed point $\mathcal{E}_{-\Gamma}$ is preserved from the earlier case, while the singularity $\mathcal{S}_{23}$ is replaced by a new equilibrium point $\mathcal{E}_{\Gamma}$.

Point c: $\Gamma = 2.5$

In this case, we choose $\Gamma > \frac{2}{\sqrt{3}}$. The Figure 6.11 illustrates phase planes for $\Gamma = 2.5$. The phase plane for $\Theta < 0$ is equivalent to that in Figure 6.10. However, the phase plane for $\Theta > 0$ has undergone a substantial transformation.

At $\Gamma = \frac{2}{\sqrt{3}}$, the equilibria $\mathcal{E}_{\Gamma}$ and $\mathcal{E}_{-\Gamma}$ collide and annihilate in a saddle-node bifurcation. As a result, the phase plane features no equilibria or singularities. Consequently, all orbits for $\Theta > 0$ exhibit the direct scattering type.

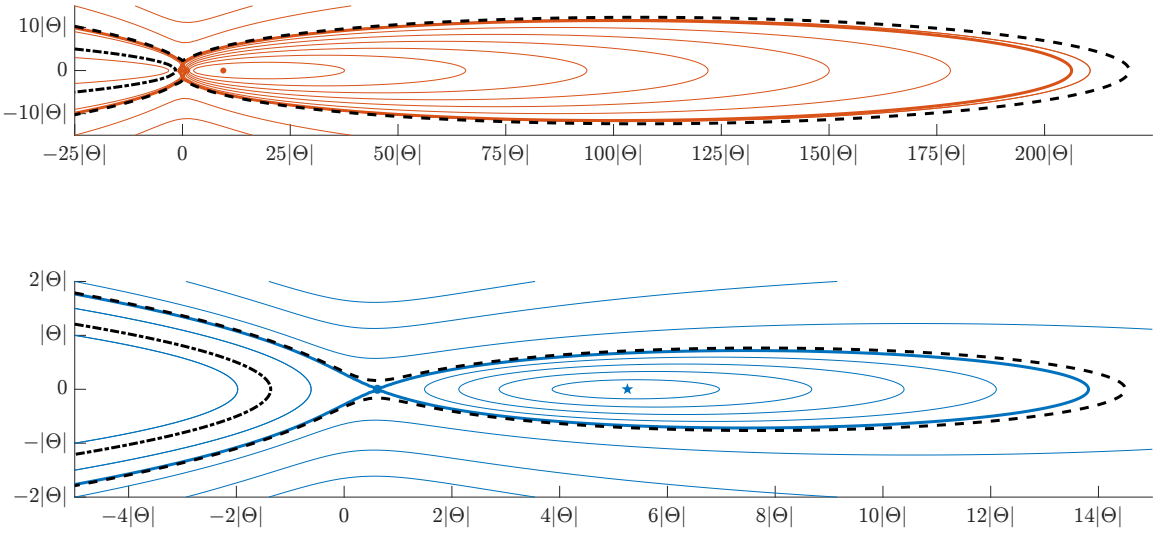

Figure 6.10 The phase planes for $\Gamma = \frac{10}{9} \in \left(1, \frac{2}{\sqrt{3}}\right)$. Top: The $\Theta < 0$ case, showing two singular points, $\mathcal{S}_{12}$ and $\mathcal{S}_{23}$ (points), and two equilibria $\mathcal{E}^{\pm}_{\text{tri}}$ at the separatrix intersections. Bottom: The $\Theta > 0$ case, showing collinear equilibria $\mathcal{E}_{\Gamma}$ ($\star$) and $\mathcal{E}_{-\Gamma}$ at the separatrix intersection.

6.4.3 Explaining the scattering for $\Gamma \neq 1$

The setup of the three-vortex scattering phenomenon in the generalized system is depicted in Figure 6.3. In this configuration, the vortices have circulations $(\Gamma, 1, -\Gamma)$, where $0 < \Gamma \neq 1$. A vortex dipole—comprising a positive-circulation vortex at position at $\mathbf{r}_1^0 = \langle -L, \rho + \frac{d}{2} \rangle$ and a negative-circulation vortex at $\mathbf{r}_3^0 = \langle -L, \rho - \frac{d}{2} \rangle$ propagates to the right toward a single vortex of positive circulation located at $\mathbf{r}_2^0 = \langle 0, -\Gamma d \rangle$. The physical configuration remains as shown in Figure 6.3, with the primary modification being the introduction of the more general circulation parameter Γ. It is easy to verify that the center of vorticity is at the origin, that is,

$$\begin{aligned}
\mathbf{Z}_3 &= \frac{\Gamma_1 \mathbf{r}_1^0 + \Gamma_2 \mathbf{r}_2^0 + \Gamma_3 \mathbf{r}_3^0}{\Gamma_1 + \Gamma_2 + \Gamma_3} \\
&= \Gamma \mathbf{r}_1^0 + \mathbf{r}_2^0 - \Gamma \mathbf{r}_3^0 \\
&= \langle -L + L, \frac{\Gamma d}{2} - \Gamma d + \frac{\Gamma d}{2} \rangle \\
&= \langle 0, 0 \rangle.
\end{aligned}$$

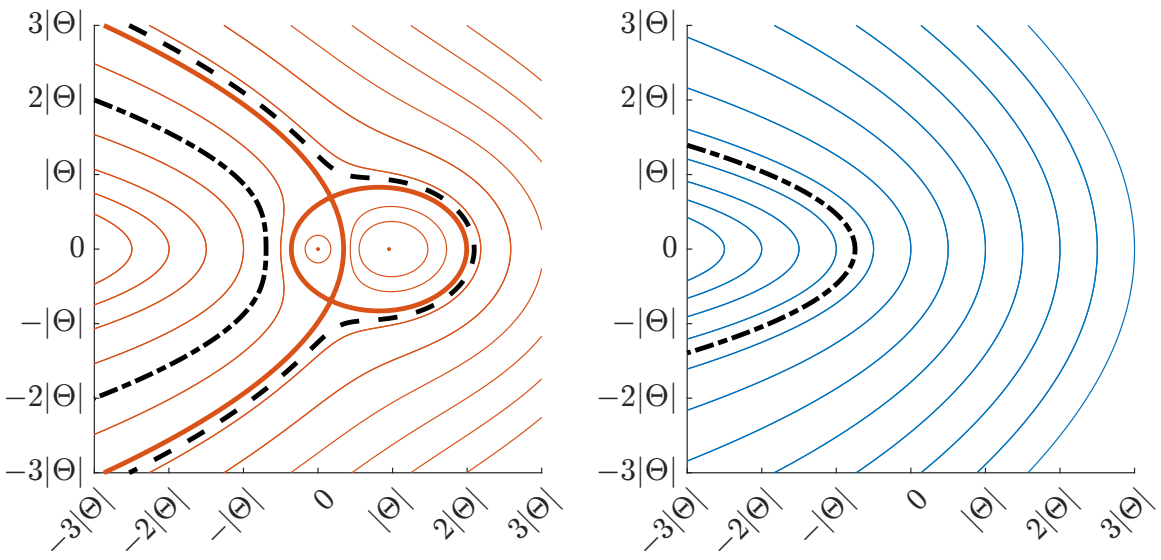

Figure 6.11 The phase planes for $\Gamma = 2.5 > \frac{2}{\sqrt{3}}$. Left: The case $\Theta < 0$ with singular points $\mathcal{S}_{12}$ (left) and $\mathcal{S}_{23}$ (right). Right: The case $\Theta > 0$, which has no fixed points or singular points.

The generalized Hamiltonian in the new coordinates

$$\begin{aligned} h &= -\frac{\Gamma}{2}\log\left\|\mathbf{r}_1^0 - \mathbf{r}_2^0\right\|^2 + \frac{\Gamma}{2}\log\left\|\mathbf{r}_2^0 - \mathbf{r}_3^0\right\|^2 + \frac{\Gamma^2}{2}\log\left\|\mathbf{r}_1^0 - \mathbf{r}_3^0\right\|^2 \\ &= \frac{\Gamma}{2}\log\left(\frac{L^2 + [\rho - d(\Gamma - 1/2)]^2}{L^2 + [\rho + d(\Gamma + 1/2)]^2}\right) + \frac{\Gamma^2}{2}\log(d)^2 \\ &= \frac{\Gamma^2}{2}\log(d)^2 + \mathcal{O}\left(\frac{1}{L}\right). \end{aligned} \tag{6.17}$$

Without loss of generality, we assume $d = 1$. Under this assumption, and as $L \to +\infty$, $h \to 0$, and the angular momentum in these new coordinates is

$$\begin{aligned} \Theta &= \Gamma_1\left\|\mathbf{r}_1^0\right\|^2 + \Gamma_2\left\|\mathbf{r}_2^0\right\|^2 + \Gamma_3\left\|\mathbf{r}_3^0\right\|^2 \\ &= \Gamma\left\|\mathbf{r}_1^0\right\|^2 + \left\|\mathbf{r}_2^0\right\|^2 - \Gamma\left\|\mathbf{r}_3^0\right\|^2 \\ &= \Gamma\left(L^2 + \left(\rho + \frac{\Gamma d}{2}\right)^2\right) + \Gamma^2 d^2 - \Gamma\left(L^2 + \left(\rho - \frac{\Gamma d}{2}\right)^2\right) \\ &= \Gamma^2(1 + 2\rho). \end{aligned} \tag{6.18}$$

Now, let us discuss the scattering phenomenon by using the same methodology as outlined in Subsection 6.3.1. In the case where $\Theta < 0$, wherein the energy level of the separatrices aligns with that of the rotating triangular configurations denoted as $\mathcal{E}^{\pm}_{\text{tri}}$.

$$E(\mathcal{E}^{\pm}_{\text{tri}}) = \frac{\Gamma^2}{2}\log(-2\Theta(1+\Gamma)) + \frac{\Gamma}{2}\log\big((1+\Gamma)^2\big). \tag{6.19}$$

Substituting the value of Θ obtained from Equation (6.18) into the Hamiltonian in Equation (6.17), we obtain

$$\rho^{-}_{\text{crit}} = -1,$$

which does not change from the one obtained in the Equation (6.11).

For $\Theta > 0$ and $\Gamma < \frac{2}{\sqrt{3}}$, the critical energy is obtained by the collinear equilibria $\mathcal{E}_{-\Gamma}$. The energy at the collinear equilibria $\mathcal{E}_{-\Gamma}$, is

$$E(\mathcal{E}_{-\Gamma}) = \frac{\Gamma^2}{2}\log\left(\frac{(2-\Gamma^2+\sqrt{4-3\Gamma^2})2\Theta}{\Gamma-1}\right) + \frac{\Gamma}{2}\log\left(\left(\frac{\Gamma-\sqrt{4-3\Gamma^2}}{\Gamma+\sqrt{4-3\Gamma^2}}\right)(\Gamma^2-1)\right). \tag{6.20}$$

From Equations (6.17), (6.18), and (6.20), we obtain

$$\rho^{+}_{\text{crit}} = \frac{(1+\Gamma)^2(1-\Gamma)\left(\frac{(B+1)(\Gamma+1)^2\left(1-\Gamma^2\right)}{-2A\Gamma^2+B(1-\Gamma^4)-(1-\Gamma^2)^2}\right)^{\frac{1}{\Gamma}}}{2(A+B\Gamma)} - \frac{1}{2},$$

where

$$A = \Gamma^2 - 2 + \sqrt{4-3\Gamma^2} \quad \text{and} \quad B = \sqrt{\Gamma^2(\Gamma^2-1)^2 + A^2}.$$

This result agrees with the value $\frac{7}{2}$ obtained for $\Gamma = 1$. Since there is no hyperbolic fixed point when $\Theta > 0$ and $\Gamma < \frac{\sqrt{3}}{2}$, the scattering diagram is expected to exhibit only a single singular point.

Figure 6.12 presents two examples of scattering diagrams, illustrating how the second singularity vanishes as Γ decreases. For $\Gamma = 2.5$, the curve exhibits a discontinuous jump of 2π at approximately $\rho \approx -0.88$.

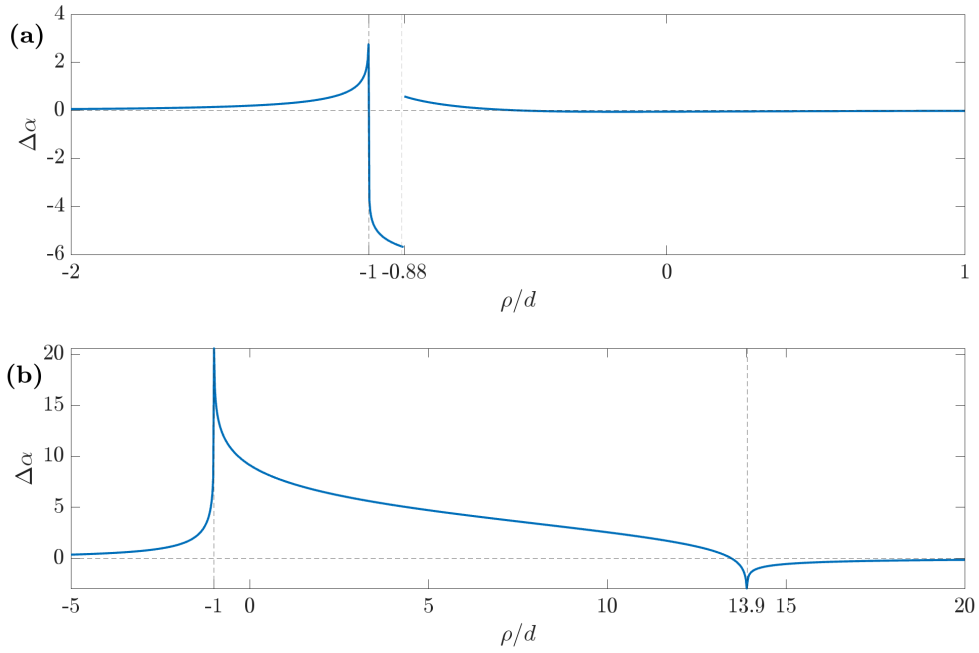

Figure 6.12 (a) Scattering angle as a function of ρ for $\Gamma = 2.5$. **(b)** The case $\Gamma = \frac{10}{17}$.

This phenomenon is attributed to the disappearance of a loop in the trajectory of vortex 3, as shown in Figure 6.13.

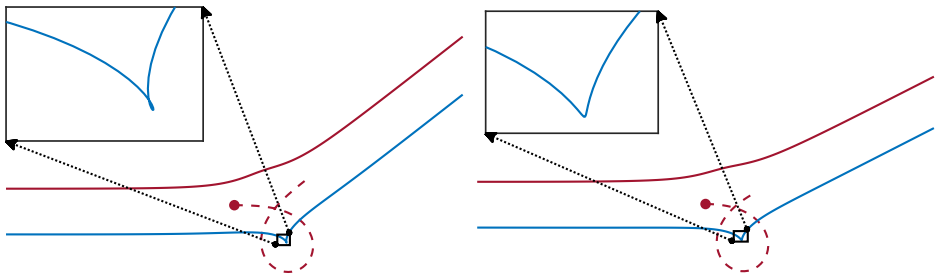

Figure 6.13 (a) Vortex trajectories for $\Gamma = 0.4$ and $\rho = -0.9$. **(b)** The trajectories for $\rho = -0.85$. In the left panel, the trajectory of vortex 3 forms a small loop, which disappears in the right panel. This change explains the 2π jump in the scattering angle observed in Figure 6.12.

CHAPTER 7

THE FOUR VORTEX MOTION WITH VANISHING NET CIRCULATION

The dynamics of four interacting point vortices form an integrable system when the total circulation of the vortices is zero and the system has zero linear impulse.

Eckhardt [17] was the first to analyze the dynamics of four-point vortices on an unbounded plane under the conditions of zero net circulation and zero linear impulse. Under these conditions, he showed that the system is integrable and its equations of motion can be solved in closed form. Using a Hamiltonian formulation, he further showed the system's phase space and identified uniformly rotating configurations as a class of exact solutions.

Rott [44] showed that the case with zero total circulation and zero linear impulse can, in fact, be reduced to a three-body problem analogous to the three-vortex case.

Aref and Stremler [7] revisited this problem using the trilinear coordinate formulation, which, as discussed in Section 1.3, simplifies the governing equations but introduces coordinate singularities. These singularities, also present in the three-vortex problem, complicate the analysis of specific vortex configurations and limit the general applicability of the resulting solutions.

Motivated by the limitations of trilinear coordinates discussed in the preceding chapter, we aim to reformulate the four-vortex problem in a more elegant framework—one that is free from coordinate singularities. The reduction method we introduce is discussed the following section.

7.1 Reduction to the Three-Vortex Problem

In this section, we discuss the four vortex problem of arbitrary circulations such that

$$\Gamma_1 + \Gamma_2 + \Gamma_3 + \Gamma_4 = 0. \tag{7.1}$$

We will also impose the condition of vanishing linear impulse

$$(Q, P) = \sum_{i=1}^{4} \Gamma_i \mathbf{r}_i = 0. \tag{7.2}$$

From Equations (7.1) and (7.2), we see that the total circulation and linear impulse vanish. Then, from Equation (3.8), it follows that P, Q, and Θ are in pairwise involution. Therefore, we conclude that the system is integrable.

We use the same reduction technique as discussed in Section 5.1. The Jacobi transformation initially modifies vortices one and two, preserving vortices three and four. The relative positions and reduced circulations are as follows:

$$\mathbf{R}_1 = \mathbf{r}_1 - \mathbf{r}_2, \quad \mathbf{R}_2 = \frac{\Gamma_1 \mathbf{r}_1 + \Gamma_2 \mathbf{r}_2}{\Gamma_1 + \Gamma_2}, \quad \mathbf{R}_3 = \mathbf{r}_3, \quad \mathbf{R}_4 = \mathbf{r}_4;$$

$$\tilde{\Gamma}_1 = \frac{\Gamma_1 \Gamma_2}{\Gamma_1 + \Gamma_2}, \quad \tilde{\Gamma}_2 = \Gamma_1 + \Gamma_2, \quad \tilde{\Gamma}_3 = \Gamma_3, \quad \tilde{\Gamma}_4 = \Gamma_4,$$

where the positions and circulations of the ith vortex is $\mathbf{r}_i$ and Γ_i, respectively.

After the first Jacobi transformation, the new relative positions and reduced circulation of the ith vortex is $\mathbf{R}_i$ and $\tilde{\Gamma}_i$.

The second Jacobi transforms the relative positions and reduced circulations of the second and third vortex, while keeping first and fourth unchanged.

We define the relative position and reduced circulation of the ith vortex in the second Jacobi transformation as $\mathbf{Z}_i$ and κ_i, respectively.

$$\mathbf{Z}_1 = \mathbf{R}_1, \quad \mathbf{Z}_2 = \mathbf{R}_2 - \mathbf{R}_3, \quad \mathbf{Z}_3 = \frac{\mathbf{R}_2(\Gamma_1 + \Gamma_2) + \mathbf{R}_3 \Gamma_3}{\Gamma_1 + \Gamma_2 + \Gamma_3}, \quad \mathbf{Z}_4 = \mathbf{R}_4,$$

$$\kappa_1 = \frac{\Gamma_1\Gamma_2}{\Gamma_1+\Gamma_2}, \quad \kappa_2 = \frac{(\Gamma_1+\Gamma_2)\Gamma_3}{\Gamma_1+\Gamma_2+\Gamma_3}, \quad \kappa_3 = \gamma_1, \quad \kappa_4 = -\gamma_1,$$

where γ_1 is defined in Equation (5.1).

Given that both the total vorticity and the linear impulse of the system vanish, we find that

$$\mathbf{Z}_4 = \mathbf{r}_4 = \frac{\Gamma_1\mathbf{r}_1 + \Gamma_2\mathbf{r}_2 + \Gamma_3\mathbf{r}_3}{\Gamma_1+\Gamma_2+\Gamma_3} = \mathbf{Z}_3$$

As a consequence, after two successive steps of Jacobi reduction, the Hamiltonian becomes dependent solely on the variables $\mathbf{Z}_1$ and $\mathbf{Z}_2$.

We now introduce a final change of variables to express the system in terms of four scalar quantities, see Equation (5.6):

$$\mu_1 = |\mathbf{Z}_1|^2, \quad \mu_2 = |\mathbf{Z}_2|^2, \quad \mu_3 + i\mu_4 = \mathbf{Z}_1\mathbf{Z}_2^*, \quad \text{and} \quad \mu_3 - i\mu_4 = \mathbf{Z}_2\mathbf{Z}_1^* \tag{7.3}$$

In these variables, the angular impulse defined in Equation (5.4) is

$$\Theta = \kappa_1\mu_1 + \kappa_2\mu_2. \tag{7.4}$$

The system also preserves the Equation (5.15) in these variables.

Given that Θ is conserved, from Equation (5.20), we can again make an additional change of variables, defining

$$Z := \kappa_1\mu_1 - \kappa_2\mu_2 \quad \text{and} \quad X + \mathrm{i}Y := \mu_3 + \mathrm{i}\mu_4. \tag{7.5}$$

Then, the rank-one condition (5.15) becomes

$$\Theta^2 = Z^2 + 4\kappa_1\kappa_2\left(X^2+Y^2\right) = Z^2 + \frac{4\gamma_3}{\gamma_1}\left(X^2+Y^2\right), \tag{7.6}$$

which is the same as we obtained for the three vortex case in the Equation (5.17). From Equations (7.5) and (7.6), we may write the Hamiltonian as:

$$\begin{aligned} h = &-\frac{\Gamma_1\Gamma_2}{2}\log(Z+\Theta)+\frac{\Gamma_3\gamma_1}{2}\log(Z-\Theta) \\ &-\frac{\Gamma_1\Gamma_3}{2}\log\left((\Gamma_1+\Gamma_2)(\Gamma_1+\Gamma_3)\Theta+4\gamma_3 X-\left(\Gamma_1^2+\Gamma_2\Gamma_1+\Gamma_3\Gamma_1-\Gamma_2\Gamma_3\right)Z\right) \\ &-\frac{\Gamma_2\Gamma_3}{2}\log\left((\Gamma_1+\Gamma_2)(\Gamma_2+\Gamma_3)\Theta-4\gamma_3 X-\left(\Gamma_2^2+\Gamma_1\Gamma_2+\Gamma_3\Gamma_2-\Gamma_1\Gamma_3\right)Z\right) \\ &+\frac{\Gamma_1\gamma_1}{2}\log\left((\Gamma_1+\Gamma_2)(\Gamma_2+\Gamma_3)\Theta+4\gamma_3 X+\left(\Gamma_2^2+\Gamma_1\Gamma_2+\Gamma_3\Gamma_2-\Gamma_1\Gamma_3\right)Z\right) \\ &+\frac{\Gamma_2\gamma_1}{2}\log\left((\Gamma_1+\Gamma_2)(\Gamma_1+\Gamma_3)\Theta-4\gamma_3 X+\left(\Gamma_1^2+\Gamma_2\Gamma_1+\Gamma_3\Gamma_1-\Gamma_2\Gamma_3\right)Z\right), \end{aligned} \tag{7.7}$$

where γ_1 and γ_3 are defined in Equation (5.1).

In principle, this system can be approached using the same methods applied to the three-vortex problem. However, a significant complication arises: the number of terms in the resulting expressions for the resultants and discriminants is substantially greater than those encountered in the previous section (see Section 5.3, and Equations (5.28) and (5.29)). As a result, `Mathematica` is unable to return a solution.

Nevertheless, we believe that a more advanced application of algebraic geometry techniques, particularly those presented in the works of Hampton, Roberts, and Santoprete [21] and of Hoyer-Leitzel and Le [25], may offer a promising avenue for further progress.

Using the fact that the rank-one condition (5.17) for the three-vortex case (see Chapter 5) is identical to that of the four-vortex system under the constraints of vanishing linear impulse and zero net circulation (see Equation (7.6)), this geometric characterization extends directly to the constrained four-vortex dynamics.

Since Θ is conserved, the trajectories in the three-vortex system are confined to a quadric surface in the three-dimensional (X, Y, Z) space. Under the constraints of

vanishing linear impulse and zero net circulation, the four-vortex problem effectively reduces to the three-vortex case and can be analyzed similarly. Without loss of generality, we assume $\gamma_1 > 0$. The geometry of the phase space depends on the signs of the circulations:

- If one or all three circulations are positive, the surface is a spheroid with $\Theta > 0$ and Z taking both signs.
- If two circulations are positive and one is negative, the trajectories lie on a one-sheeted hyperboloid with $\gamma_3 < 0$ restricting $Z > 0$, while Θ can vary.
- When $\Theta = 0$, the surface reduces to the upper half of a right circular cone.

We believe these conditions will enhance our understanding of the bifurcation diagram for this case. Accordingly, we plan to apply the same analytical approach used for the three-vortex problem, introducing a novel bifurcation to interpret Figure 5.1.

CHAPTER 8

CONCLUSION

8.1 Summary of Contributions to the Three-Vortex Problem

In Chapter 1, we outlined two primary goals for this dissertation. Both of these goals have been successfully addressed.

Goal I: We focused on developing a novel coordinate reduction method for the three-vortex problem that could effectively eliminate coordinate singularities in the system.

In Chapter 4, we introduced such a method—Jacobi-Lie-Poisson reduction. This approach was then implemented in Chapter 5, where it enabled a systematic classification of all relative equilibria in the three-vortex problem. Through this new reduction method, we analyzed the linear stability of these equilibria and identified critical parameter values at which bifurcations occur.

This novel reduction method not only resolved longstanding issues related to singularities but also allowed for a complete and physically intuitive classification of the system's dynamical regimes. In addition, we performed a detailed bifurcation analysis, providing a novel interpretation of Figure 5.1, and constructed a full bifurcation diagram capturing the equilibria and singularities of the three-vortex interactions (see Figure 5.2).

Furthermore, in Section 5.5, we presented global phase portraits along the symmetry line $\Gamma_1 = \Gamma_2$ in a clear and elegant manner. These portraits offer a more accessible and insightful depiction of the dynamics than those previously available in the literature.

Goal II: We applied the reduction method to a different type of problem: vortex-dipole scattering. This was discussed in Chapter 6. We started with the symmetric case, where the vortex circulations are $(1, 1, -1)$, and then considered the

more general asymmetric case with circulations $(\Gamma, 1, -\Gamma)$, where $0 < \Gamma \neq 1$. These examples showed that the Jacobi-Lie-Poisson reduction method can also be used to study vortex-dipole scattering effectively. We compared our results with those from existing research and confirmed that our method gives accurate results.

8.2 Application to the Integrable Four-Vortex Problem

In addition to outlining two goals, we also mentioned a to-do item in Chapter 1, which discusses the integrable four-vortex problem and how our novel reduction to the three-vortex case can be effectively applied to the four-vortex case.

In Chapter 7, we applied the reduction techniques introduced in Chapters 4 and 5 to the integrable four-vortex problem. This process led to the derivation of the Hamiltonian for the reduced system, which forms the basis for our subsequent analysis. While we briefly discussed the additional challenges involved in studying the four-vortex dynamics compared to the three-vortex case, we also pointed to relevant literature that will be useful for developing a comprehensive analysis of the system.

APPENDIX A

SUPPLEMENT FOR CALCULATING THE SCATTERING ANGLE IN VORTEX-DIPOLE SCATTERING

This appendix computes the change in angle $\Delta\alpha$ along trajectories with initial conditions as $t \to -\infty$, as depicted in Figure 6.3. The result obtained is equivalent to the one calculated in the supplementary material of [31], and is provided here for completeness, with an emphasis on its connection to the phase planes shown in Figure 6.5.

To derive an explicit integral form, we differentiate $\frac{\mathrm{d}\alpha}{\mathrm{d}t}$ with respect to Y, as obtained from Equation (6.2b) and Equation (6.7). Subsequently, we eliminate the dependencies on X and Z by employing the conservation laws (5.17) and (6.1).

Finally, we substitute H with its value determined by the initial condition presented in Figure 6.3. In the subsequent calculations, we will utilize Θ as the parameter, as it simplifies the formulas and enables us to rewrite the expression in terms of the parameter ρ defining the initial conditions, as obtained from Equation (6.10). Integrating this expression yields an expression for $\Delta\alpha$ as a definite integral

$$\Delta\alpha = \int_{Y_{\min}}^{\infty} \frac{-8\Theta^2 \mathrm{d}Y}{(Y^2+\Theta^2)\sqrt{p_4(Y^2;\Theta)}} + \int_{Y_{\min}}^{\infty} \frac{8(\Theta^2-8\Theta)\mathrm{d}Y}{(Y^2+\Theta^2-8\Theta)\sqrt{p_4(Y^2;\Theta)}}, \tag{A.1}$$

where

$$p_4(Y^2;\Theta) = Y^4 + 2\left(\Theta^2-4\Theta-8\right)Y^2 + (\Theta-8)\Theta^3.$$

In the expression for $\Delta\alpha$, the lower limit $Y_{\min}$ ensures $p_4(Y^2;\Theta) \geq 0$ so the integrand is real. Since the integrand is even in Y, the integral over $(-\infty,\infty)$ reduces

to twice the integral from $Y_{\min}$ to ∞, eliminating the need to integrate over negative values. These are *complete elliptic integrals* [13].

To place them in standard form, we must first factor $p_4(Y^2;\Theta)$. We plot its zero locus in Figure A.1 as a function of Θ and Y^2. From this image, it is clear that p_4 can be factored as follows

$$p_4(Y^2,\Theta) = \begin{cases} (Y^2-(a+ib)^2)(Y^2-(a-ib)^2), & a>0, b>0, \text{ if } \Theta<-1; \\ (Y^2-a^2)(Y^2-b^2), & a>b>0, \text{ if } -1<\Theta<0; \\ (Y^2-a^2)(Y^2+b^2), & a>0, b>0, \text{ if } 0<\Theta<8; \\ (Y^2+a^2)(Y^2+b^2), & a>b>0, \text{ if } 8<\Theta. \end{cases} \tag{A.2}$$

The first two cases correspond to the left phase plane of Figure 6.5, the last two to the right phase plane; the first and last cases correspond to direct scattering, and the second and third to exchange scattering. The lower limit of integration is $Y_{\min}=0$ in the first and fourth cases, while in the second and third $Y_{\min}=a$.

Both integrals in Equation (A.1) can be evaluated with the help of references such as Gradshteyn/Ryzhik and Byrd/Friedman [13, 19]. It is quite possible that these expressions can be simplified further.

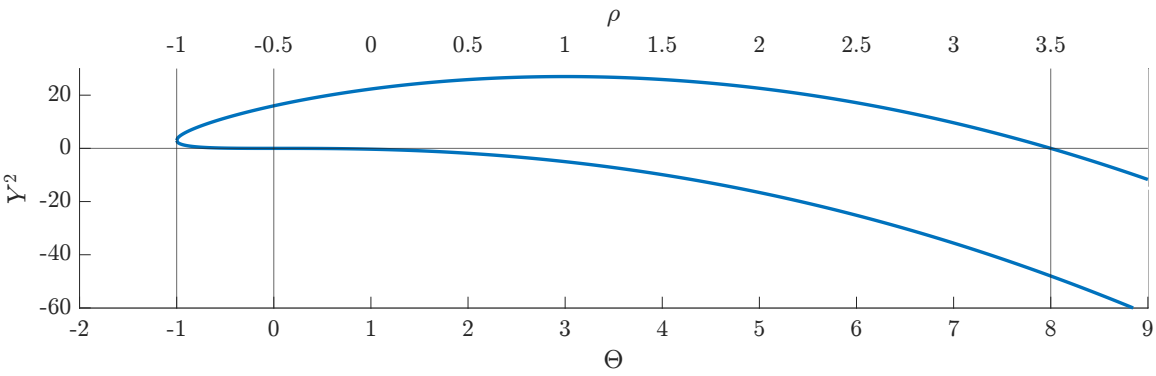

Figure A.1 The solutions to $p_4(Y^2,\Theta)=0$, with the transitions between the factored form in Equation (A.2) marked be vertical lines.

In the four regions, the constants evaluate to the following

$$\binom{a^2}{b^2} = \begin{cases} \frac{1}{2}\begin{pmatrix} \sqrt{\Theta-8}\Theta^{3/2} - \Theta^2 + 4\Theta + 8 \\ \sqrt{\Theta-8}\Theta^{3/2} + \Theta^2 - 4\Theta - 8 \end{pmatrix} & \text{if } \Theta < -1; \\ \begin{pmatrix} -\Theta^2 + 4\Theta + 8\sqrt{\Theta+1} + 8 \\ -\Theta^2 + 4\Theta - 8\sqrt{\Theta+1} + 8 \end{pmatrix} & \text{if } -1 < \Theta < 0; \\ \begin{pmatrix} -\Theta^2 + 4\Theta + 8\sqrt{\Theta+1} + 8 \\ \Theta^2 - 4\Theta + 8\sqrt{\Theta+1} - 8 \end{pmatrix} & \text{if } 0 < \Theta < 8; \\ \begin{pmatrix} \Theta^2 - 4\Theta + 8\sqrt{\Theta+1} - 8 \\ \Theta^2 - 4\Theta - 8\sqrt{\Theta+1} - 8 \end{pmatrix} & \text{if } 8 < \Theta. \end{cases}$$

In each of the four ρ intervals, the scattering angle can be written as a linear combination of complete elliptic integrals of the first kind

$$K(m) = \int_0^1 \frac{\mathrm{d}x}{\sqrt{(1-x^2)\,(1-mx^2)}} = \int_0^{\frac{\pi}{2}} \frac{\mathrm{d}\theta}{\sqrt{1-m\sin^2\theta}}.$$

and the third kind

$$\Pi(n,m) = \int_0^1 \frac{\mathrm{d}x}{(1-nx^2)\sqrt{(1-x^2)\,(1-mx^2)}} = \int_0^{\frac{\pi}{2}} \frac{\mathrm{d}\theta}{\left(1-n\sin^2\theta\right)\sqrt{1-m\sin^2\theta}}.$$

The convention is to define these functions for $0 < m < 1$, though they are analytic for all m except for a branch cut from $m = 1$ to $m = \infty$ along the positive real axis. In the next section, we report the values found in each of the cases.

A.1 Direct Scattering with $\rho < -1$

Here $\Theta < -1$, and

$$\Delta\alpha = \frac{64\sqrt[4]{\Theta - 8}\,(-K(m) + \Pi(n,m))}{\sqrt[4]{\Theta}\left(\Theta - 8 + \sqrt{\Theta^2 - 8\Theta}\right)\left(\Theta + \sqrt{\Theta^2 - 8\Theta}\right)}$$

with

$$m = \frac{1}{2} + \frac{4 - \Theta}{2\sqrt{\Theta^2 - 8\Theta}} \quad \text{and} \quad n = \frac{1}{2} - \frac{\Theta^2 - 4\Theta - 8}{2\Theta\sqrt{\Theta^2 - 8\Theta}}.$$

A.2 Exchange Scattering with $-1 < \rho < -\frac{1}{2}$

In this case $-1 < \Theta < 0$, and

$$\Delta\alpha = \frac{4\Theta K(m) + 8\sqrt{1+\Theta}\Big(\Pi(n_1,m) - \Pi(n_2,m)\Big)}{\sqrt{-\Theta^2 + 4\Theta + 8\sqrt{\Theta+1} + 8}},$$

where

$$\begin{aligned} m &= \frac{8 + 4\Theta - \Theta^2 - 8\sqrt{\Theta+1}}{8 + 4\Theta - \Theta^2 + 8\sqrt{\Theta+1}}, \\ n_1 &= \frac{\Theta - 2 + 2\sqrt{\Theta+1}}{\Theta + 2 - 2\sqrt{\Theta+1}}, \\ n_2 &= \frac{\Theta + 2 - 2\sqrt{\Theta+1}}{\Theta + 2 + 2\sqrt{\Theta+1}}. \end{aligned}$$

A.3 The Borderline case $\rho = -\frac{1}{2}$

This is the case $\Theta = 0$ plotted in Figure 6.6 (b). Vortex 2 travels along a straight line with no deflection, so the scattering angle is $\alpha = 0$.

A.4 Exchange Scattering with $-\frac{1}{2} < \rho < \frac{7}{2}$

Here $0 < \Theta < 8$, and

$$\Delta\alpha = \frac{-\Theta^2 + 4\Theta + 8\sqrt{\Theta+1} + 8}{2\sqrt[4]{\Theta+1}\left(\Theta + 2\sqrt{\Theta+1} + 2\right)}\Big(\Pi(n_1, m) - \Pi(n_2, m)\Big),$$

where

$$\begin{aligned} m &= \frac{1}{2} + \frac{\Theta^2 - 4\Theta - 8}{16\sqrt{1-\Theta}}, \\ n_1 &= \frac{2 - \Theta - 2\sqrt{1+\Theta}}{4}, \\ n_2 &= \frac{2 + \Theta - 2\sqrt{1+\Theta}}{4}. \end{aligned}$$

A.5 Direct Scattering with $\frac{7}{2} < \rho$

In this last case, $\Theta > 8$ and

$$\Delta\alpha = c_K K(m) + c_{\Pi,1}\Pi_1(n_1, m) + c_{\Pi,2}\Pi(n_2, m),$$

where

$$m = \frac{16\sqrt{\Theta+1}}{\Theta^2 - 4\Theta - 8 + 8\sqrt{\Theta+1}}, n_1 = -\frac{4}{\Theta + 2\sqrt{\Theta+1} - 2}, n_2 = \frac{4\left(\Theta + 2\sqrt{\Theta+1} + 2\right)}{\Theta^2},$$

$$c_K = -\frac{4\Theta}{\sqrt{\Theta^2 - 4\Theta + 8\sqrt{\Theta+1} - 8}},$$

$$c_{\Pi,1} = \frac{-2\Theta^3 + 4\Theta^2 + 64\Theta + 64 - 4\sqrt{\Theta+1}\left(\Theta^2 - 8\Theta - 16\right)}{\sqrt{(\Theta-8)\Theta^3\left((\Theta-4)\Theta - 8\left(\sqrt{\Theta+1}+1\right)\right)}},$$

$$\text{and} \quad c_{\Pi,2} = \frac{-2\Theta^3 + 12\Theta^2 - 32\Theta - 64 + 4\left(\Theta^2 - 16\right)\sqrt{\Theta+1}}{\sqrt{(\Theta-8)\Theta^3\left((\Theta-4)\Theta - 8\left(\sqrt{\Theta+1}+1\right)\right)}}$$

APPENDIX B

TRILINEAR COORDINATES FOR THE PLANE

In this appendix, we define the trilinear coordinates for the plane. To define trilinear coordinates, we define three points on the unit circle

$$(x_1, y_1) = (0, 1), \quad (x_2, y_2) = \left(\frac{-\sqrt{3}}{2}, \frac{-1}{2}\right), \quad (x_3, y_3) = \left(\frac{\sqrt{3}}{2}, \frac{-1}{2}\right).$$

Then, the point defined by the affine combination[1]

$$\eta_1 x_1 + \eta_2 x_2 + \eta_3 x_3 = x, \quad \eta_1 y_1 + \eta_2 y_2 + \eta_3 y_3 = y,$$

where the weights η_j satisfy Equation (5.24), defines the point (x, y) as an *affine* (or weighted) combination of the three points $(x_1, y_1), (x_2, y_2), (x_3, y_3)$. Geometrically, this means:

- If all weights $\eta_j \geq 0$, then (x, y) lies *inside or on the boundary* of the triangle formed by the three points.
- If one or more weights are negative, then (x, y) lies *outside* the triangle, but still within the *affine span* of the three points, which in this case is the entire plane (since the points are assumed non-collinear).

[1] An affine combination of elements $x_1, \ldots, x_n$ in a vector space over a field K is a linear combination

$$\sum_{i=1}^{n} \alpha_i x_i = \alpha_1 x_1 + \alpha_2 x_2 + \cdots + \alpha_n x_n,$$

where the coefficients α_i are elements of K and satisfy the constraint

$$\sum_{i=1}^{n} \alpha_i = 1.$$

APPENDIX C

PROOF OF THE MAPS DEFINED IN SECTION 4.3

In this appendix, we present the theorems and definitions necessary to prove the functional maps defined in Section 4.3. Throughout this appendix, we assume that $V(\mathbb{K})$ is a vector space defined over a field $\mathbb{K}$, which we consider here to be a $\mathbb{C}$ or $\mathbb{R}$.

C.1 Tangent Space

Let M be a smooth manifold, and let $p \in M$ be a point. The tangent space of M at p, denoted by T_pM, is the vector space of all tangent vectors to M at the point p. It is defined as follows:

$$T_pM := \left\{ \frac{\mathrm{d}}{\mathrm{d}t}\gamma(t)\bigg|_{t=0} \;\middle|\; \gamma : (-\epsilon, \epsilon) \to M \text{ is smooth, } \gamma(0) = p, \epsilon > 0 \right\}$$

If $M = \mathbb{R}^n$, the tangent space at any point $p \in \mathbb{R}^n$ is simply the space of all vectors in $\mathbb{R}^n$, i.e.,

$$T_p\mathbb{R}^n \cong \mathbb{R}^n.$$

C.2 Cotangent Bundle

Let M be a smooth manifold of dimension n. For each point $x \in M$, the *cotangent space* at x, denoted T_x^*M, is the dual vector space to the tangent space T_xM:

$$T_x^*M := \mathrm{Hom}(T_xM, \mathbb{R}),$$

where $\mathrm{Hom}(T_xM, \mathbb{R})$ denotes the space of all linear functionals on T_xM. In local coordinates $(x^1, \ldots, x^n)$ on M, the cotangent space T_x^*M has a natural basis

$$\{dx^1, dx^2, \ldots, dx^n\},$$

which is dual to the basis $\left\{\frac{\partial}{\partial x^1}, \ldots, \frac{\partial}{\partial x^n}\right\}$ of the tangent space T_xM. Any $\alpha \in T_x^*M$ can be written as

$$\alpha = \sum_{i=1}^{n} a_i \, dx^i,$$

for some coefficients $a_i \in \mathbb{R}$.

C.3 Group

A group G is a set equipped with a binary operation $*$ that satisfies the following properties:

- **Closure:** For all $a, b \in G$, $a * b \in G$.
- **Associativity:** For all $a, b, c \in G$, $(a * b) * c = a * (b * c)$.
- **Identity element:** There exists an element $e \in G$ such that for all $a \in G$, $a * e = e * a = a$.
- **Inverse element:** For every $a \in G$, there exists an element $a^{-1} \in G$ such that $a * a^{-1} = a^{-1} * a = e$, where e is the identity element.

A simple example of a group is the set of real numbers under addition, i.e., $(\mathbb{R}, +)$. The operation $*$ in this case is the addition of real numbers.

C.4 Group Action

Let G be a group, and let X be a set. A *left group action* of G on X is a map:

$$\alpha : G \times X \to X,$$

that satisfies the following two properties:

- **Identity property:** For all $x \in X$, we have $\alpha(e, x) = x$, where $e \in G$ is the identity element of the group.
- **Compatibility property:** $\alpha(g_1, \alpha(g_2, x)) = \alpha(g_1 g_2, x)$, for all g_1 and g_2 in G and all x in X.

C.5 Lie Group

A Lie group G is a group that is also a smooth manifold such that the group operations (multiplication and inversion) are smooth maps. Specifically:

- The map $m : G \times G \to G, \quad (g_1, g_2) \mapsto g_1 g_2$ is smooth.
- The inverse map $\iota : G \to G, \quad g \mapsto g^{-1}$ is smooth.

One of the famous examples of a Lie group is the *general linear group* $\mathrm{GL}(n, \mathbb{R})$, which consists of all $n \times n$ invertible matrices with real entries. The operation in this case is matrix multiplication. Formally, we define the general linear group as:

$$\mathrm{GL}(n, \mathbb{R}) = \{A \in \mathbb{R}^{n \times n} \mid \det(A) \neq 0\},$$

where A is an $n \times n$ matrix and $\det(A)$ denotes the determinant of A.

It is easy to verify that the set $\mathrm{GL}(n, \mathbb{R})$ under multiplicative operation forms a group. In addition to the group structure, $\mathrm{GL}(n, \mathbb{R})$ is also a smooth manifold. The group operations of matrix multiplication and inversion are smooth maps:

- The multiplication map $m : \mathrm{GL}(n, \mathbb{R}) \times \mathrm{GL}(n, \mathbb{R}) \to \mathrm{GL}(n, \mathbb{R})$, given by $(A, B) \mapsto AB$, is smooth.
- The inverse map $\iota : \mathrm{GL}(n, \mathbb{R}) \to \mathrm{GL}(n, \mathbb{R})$, given by $A \mapsto A^{-1}$, is also smooth.

Thus, $\mathrm{GL}(n, \mathbb{R})$ is a Lie group because it is both a group and a smooth manifold where the group operations are smooth.

C.6 Lie Algebras

The Lie algebra describes the infinitesimal structure of the Lie group around the identity element. The Lie algebra of a Lie group G, denoted $\mathfrak{g}$, is the tangent space at the identity element $e \in G$, i.e.,

$$\mathfrak{g} = T_e G.$$

The Lie algebra is a vector space that is equipped with a Lie bracket, which is a bilinear map:

$$[\cdot, \cdot] : \mathfrak{g} \times \mathfrak{g} \to \mathfrak{g},$$

and satisfies:

- **Bilinearity:** $[X, aY + bZ] = a[X, Y] + b[X, Z]$,
- **Anti-symmetry:** $[X, Y] = -[Y, X]$,
- **Jacobi identity:** $[X, [Y, Z]] + [Y, [Z, X]] + [Z, [X, Y]] = 0$.

The Lie algebra of the Lie group $\mathrm{GL}(n, \mathbb{R})$, its Lie algebra $\mathfrak{g}$ is the space of all $n \times n$ matrices,

$$\mathfrak{g} = \mathfrak{gl}(n, \mathbb{R}),$$

with the Lie bracket defined by the matrix commutator:

$$[A, B] = AB - BA.$$

This Lie algebra is the vector space of all $n \times n$ real matrices.

C.7 Linear Functional

Let V be a vector space over $\mathbb{C}$. A **linear functional** on V is a linear map

$$\phi : V \to \mathbb{C}$$

such that for all $u, v \in V$ and $\alpha \in \mathbb{C}$, we have:

$$\phi(u+v) = \phi(u) + \phi(v), \quad \phi(\alpha v) = \alpha\phi(v).$$

C.8 Dual Space

The **dual space** of V, denoted V^*, is the set of all linear functionals on V:

$$V^* = \{\phi : V \to \mathbb{C} \mid \phi \text{ is linear}\}.$$

C.9 Riesz Representation Theorem

Let H be a Hilbert space over $\mathbb{C}$ with inner product $\langle \cdot, \cdot \rangle$. For every continuous linear functional $\phi \in H^*$, there exists a **unique** element $u_\phi \in H$ such that

$$\phi(v) = \langle v, u_\phi \rangle \quad \text{for all } v \in H.$$

Moreover, the correspondence is norm-preserving:

$$\|\phi\| = \|u_\phi\|.$$

C.10 Dual of a Lie Algebra

Let $\mathfrak{g}$ be a finite-dimensional Lie algebra over a field $\mathbb{F}$. The **dual space** of $\mathfrak{g}$ is:

$$\mathfrak{g}^* := \{\phi : \mathfrak{g} \to \mathbb{F} \mid \phi \text{ is linear functional}\}$$

C.11 Coadjoint Action

The *coadjoint action* ad^*_ξ is the dual action of the adjoint action on the dual space $\mathfrak{g}^*$. The adjoint action ad_ξ is defined by the Lie bracket:

$$\mathrm{ad}_\xi \eta = [\xi, \eta], \quad \text{for } \xi, \eta \in \mathfrak{g}.$$

The *coadjoint action* ad^*_ξ acts on the dual space $\mathfrak{g}^*$ and is defined through the following relation:

$$\langle \mathrm{ad}^*_\xi \mu, \eta \rangle = \langle \mu, [\xi, \eta] \rangle, \quad \text{for all } \mu \in \mathfrak{g}^*, \xi, \eta \in \mathfrak{g}.$$

Here, $\langle \cdot, \cdot \rangle$ denotes the natural pairing between $\mathfrak{g}^*$ and $\mathfrak{g}$, and $\mu \in \mathfrak{g}^*$ is a linear functional on $\mathfrak{g}$.

C.12 Directional Derivative

Let $F \in \mathcal{C}^\infty(\mathfrak{g}^*)$ be a smooth function on the Lie algebra $\mathfrak{g}$. The **directional derivative** of F at a point $\mu \in \mathfrak{g}^*$ in the direction $v \in \mathfrak{g}^*$ is defined as:

$$DF(\mu)v := \frac{\mathrm{d}}{\mathrm{d}t} F(\mu + tv)\bigg|_{t=0}.$$

Note: The map $DF(\mu) : \mathfrak{g}^* \to \mathbb{R}$ is a linear functional on $\mathfrak{g}^*$, also known as the Fréchet derivative. Since $DF(\mu)$ linear functional on $\mathfrak{g}^*$, that means,

$$DF(\mu) \in (\mathfrak{g}^*)^* \cong \mathfrak{g}.$$

Since, $DF(\mu) \in \mathfrak{g}$, by the Riesz Representation theorem, there exists a unique $\frac{\partial f}{\partial \mu} \in \mathfrak{g}$, such that

$$DF(\mu)v = \left\langle v, \frac{\partial f}{\partial \mu} \right\rangle, \forall v \in \mathfrak{g}^*.$$

C.13 Lie-Poisson Equations

Let $\mathfrak{g}$ be a finite-dimensional Lie algebra, and let $\mathfrak{g}^*$ be its dual. Consider a smooth Hamiltonian function $H : \mathfrak{g}^* \to \mathbb{R}$. For any smooth function $F : \mathfrak{g}^* \to \mathbb{R}$, define the Lie–Poisson bracket as:

$$\{F, H\}(\mu) = \left\langle \mu, \left[\frac{\delta F}{\delta \mu}, \frac{\delta H}{\delta \mu} \right] \right\rangle,$$

where $\mu \in \mathfrak{g}^*$, and $\frac{\delta F}{\delta \mu}, \frac{\delta H}{\delta \mu} \in \mathfrak{g}$ denote the functional derivatives of F and H, respectively. The time evolution of F is given by Hamilton's equation:

$$\frac{\mathrm{d}F}{\mathrm{d}t} = \{F, H\}(\mu) = \left\langle \mu, \left[\frac{\delta F}{\delta \mu}, \frac{\delta H}{\delta \mu} \right] \right\rangle.$$

Using the definition of the coadjoint action ad^*, which satisfies:

$$\langle \mathrm{ad}^*_x \, \mu, y \rangle = \langle \mu, [y, x] \rangle \quad \forall x, y \in \mathfrak{g},$$

we obtain:

$$\left\langle \mu, \left[\frac{\delta F}{\delta \mu}, \frac{\delta H}{\delta \mu} \right] \right\rangle = \left\langle \mathrm{ad}^*_{\frac{\delta H}{\delta \mu}} \, \mu, \frac{\delta F}{\delta \mu} \right\rangle.$$

Thus,

$$\frac{\mathrm{d}F}{\mathrm{d}t} = \left\langle \mathrm{ad}^*_{\frac{\delta H}{\delta \mu}} \, \mu, \frac{\delta F}{\delta \mu} \right\rangle.$$

Applying by the chain rule:

$$\frac{\mathrm{d}F}{\mathrm{d}t} = \left\langle \frac{\mathrm{d}\mu}{\mathrm{d}t}, \frac{\delta F}{\delta \mu} \right\rangle.$$

Since this equality holds for all functionals F, we identify:

$$\dot{\mu} = \frac{\mathrm{d}\mu}{\mathrm{d}t} = \mathrm{ad}^*_{\frac{\delta H}{\delta \mu}} \mu. \tag{C.1}$$

C.14 Lie Algebra of the Unitary Group $U(n)$

Let $U(n) = \{U \in GL(n, \mathbb{C}) \mid U^\dagger U = I\}$ be the group of $n \times n$ unitary matrices. We aim to show that its Lie algebra $\mathfrak{u}(n)$ is:

$$\mathfrak{u}(n) = \{X \in M_n(\mathbb{C}) \mid X^\dagger = -X\},$$

i.e., the set of skew-Hermitian matrices.

We want to find the Lie algebra $\mathfrak{u}(n)$ of the Lie group $U(n)$. By definition, the Lie algebra $\mathfrak{g}$ of a Lie group G is defined as:

$$\mathfrak{g} = T_I G,$$

the tangent space to the group at the identity element. To compute $T_I U(n)$, we take a smooth curve $U(t) \in U(n)$ such that:

- $U(0) = I$ (the identity element),
- $\frac{\mathrm{d}U}{\mathrm{d}t} \in T_I U(n)$.

Since $U(t) \in U(n)$, it satisfies:

$$U(t)^\dagger U(t) = I.$$

Differentiating both sides with respect to t at $t = 0$, we get:

$$\frac{\mathrm{d}}{\mathrm{d}t} \left(U(t)^\dagger U(t) \right) \Big|_{t=0} = 0.$$

Using the product rule:

$$\left(\frac{\mathrm{d}}{\mathrm{d}t}U(t)^\dagger\right)_{t=0} \cdot U(0) + U(0)^\dagger \cdot \left(\frac{\mathrm{d}}{\mathrm{d}t}U(t)\right)_{t=0} = 0.$$

Since $U(0) = I$, and $\frac{\mathrm{d}}{\mathrm{d}t}U(t)^\dagger = \left(\frac{\mathrm{d}}{\mathrm{d}t}U(t)\right)^\dagger$ we get:

$$\left(\frac{\mathrm{d}U}{\mathrm{d}t}\right)^\dagger + \frac{\mathrm{d}U}{\mathrm{d}t} = 0.$$

Let $X = \frac{\mathrm{d}U}{\mathrm{d}t}$. Then the condition becomes:

$$X^\dagger = -X.$$

Thus, the Lie algebra of $U(n)$ is:

$$\mathfrak{u}(n) = \{X \in M_n(\mathbb{C}) \mid X^\dagger = -X\}.$$

This is the set of all skew-Hermitian matrices. The Lie bracket on $\mathfrak{u}(n)$ is given by the matrix commutator:

$$[X, Y] = XY - YX.$$

The proof provided earlier can be used to demonstrate that $\mathfrak{u}(N)_\Gamma$ is a Lie algebra under the bracket defined in Equation (4.11).

C.15 Casimir Function

Let $(M, \{\cdot,\cdot\})$ be a Poisson manifold, where M is a smooth manifold and $\{\cdot,\cdot\}$ is a Poisson bracket on the algebra of smooth functions $C^\infty(M)$. A function $C \in C^\infty(M)$ is called a *Casimir function* if

$$\{C, f\} = 0 \quad \forall f \in C^\infty(M).$$

Properties

- Casimir functions lie in the **center**[1] of the Poisson algebra $(C^\infty(M), \{\cdot,\cdot\})$, meaning that they commute with all other functions in $C^\infty(M)$.
- They are **conserved quantities** under any Hamiltonian vector field on M.
- Casimir functions are **invariants of the Poisson structure** itself, independent of any particular Hamiltonian.

[1] Recall, the center of a Poisson manifold $C^\infty(M)$ is defined as

$$Z(C^\infty(M)) = \{C \in C^\infty(M) \mid \{C, f\} = 0 \quad \forall f \in C^\infty(M)\}\,.$$

APPENDIX D

TWO CONCEPTS FROM ALGEBRAIC GEOMETRY: THE RESULTANT AND THE DISCRIMINANT

In this Appendix, we provide a concise overview of two concepts used in Chapter 5: the resultant and discriminant. Aref [4] offers an exceptional introduction to these concepts.

D.1 The Resultant

The **resultant** of two polynomials $a(x)$ and $b(x)$ is a scalar that vanishes if and only if a and b have a common root. Let:

$$a(x) = a_0x^m + a_1x^{m-1} + \cdots + a_m, \quad b(x) = b_0x^n + b_1x^{n-1} + \cdots + b_n,$$

then the resultant $\text{Res}(a, b, x)$ is the determinant of the Sylvester matrix formed by the coefficients of a and b, which we define below in Equation (D.1).

Consider, for example, the case that

$$a(x) = a_2x^2 + a_1x + a_0, \quad b(x) = b_3x^3 + b_2x^2 + b_1x + b_0.$$

To determine whether they share a root, augment the system

$$a(x) = 0, \quad b(x) = 0$$

with the redundant equations

$$x^2a(x) = 0, \quad xa(x) = 0, \quad \text{and} \quad xb(x) = 0.$$

These expressions can be arranged into a linear system:

$$\begin{bmatrix} a_2 & a_1 & a_0 & 0 & 0 \\ 0 & a_2 & a_1 & a_0 & 0 \\ 0 & 0 & a_2 & a_1 & a_0 \\ b_3 & b_2 & b_1 & b_0 & 0 \\ 0 & b_3 & b_2 & b_1 & b_0 \end{bmatrix} \begin{bmatrix} x^4 \\ x^3 \\ x^2 \\ x^1 \\ x^0 \end{bmatrix} = \begin{bmatrix} 0 \\ 0 \\ 0 \\ 0 \\ 0 \end{bmatrix}. \tag{D.1}$$

The matrix in this equation is known as the *Sylvester matrix*. A necessary condition for system (D.1) to have a nontrivial solution is that its determinant vanishes. This determinant, denoted $\mathrm{Res}(a, b, x)$, is the resultant of the two polynomials, $a(x)$ and $b(x)$.

This construction can be extended to polynomials of arbitrary degree, and the dimension of the Sylvester matrix is $\deg a + \deg b$. In `Mathematica`, the resultant can be computed using the command `Resultant[a(x), b(x), x]`.

D.2 The Discriminant

We are often interested in how the roots of a polynomial $p(x, \mu)$ change as a parameter μ varies. In particular, in the bifurcations that occur when two or more roots coincide. This happens when $p(x, \mu)$ and its derivative $p'(x, \mu)$ vanish simultaneously.

The *discriminant* of a polynomial p is a scalar quantity that vanishes precisely when p has a multiple root. The discriminant of a degree-n polynomial

$$p(x) = a_0 x^n + a_1 x^{n-1} + \cdots + a_n$$

is given by

$$\mathrm{Disc}(p) = (-1)^{n(n-1)/2} \cdot \frac{1}{a_0} \cdot \mathrm{Res}(p, p', x),$$

where $p'(x)$ is the derivative of $p(x)$. For a quadratic function $p(x) = ax^2 + bx + c$, we have

$$\mathrm{Disc}(p) = (-1)^1 \cdot \frac{1}{a} \cdot \mathrm{Res}(p, p') = b^2 - 4ac,$$

which is the well-known quadratic discriminant $b^2 - 4ac$. The Discriminant can be computed using `Mathematica`'s command `Discriminant[p(x), x]`.

REFERENCES

[1] A. Anurag, R. H. Goodman, and E. K. O'Grady. A new canonical reduction of three-vortex motion and its application to vortex-dipole scattering. *Physics of Fluids*, 36:067110, 2024.

[2] H. Aref. Motion of three vortices. *The Physics of Fluids*, 22(3):393–400, 1979.

[3] H. Aref. Point vortex dynamics: a classical mathematics playground. *Journal of Mathematical Physics*, 48(6), 2007.

[4] H. Aref. Stability of relative equilibria of three vortices. *Physics of Fluids*, 21(9), 2009.

[5] H. Aref. Three-vortex motion with zero total circulation: addendum. *Zeitschrift für angewandte Mathematik und Physik ZAMP*, 40:495–500, 1989.

[6] H. Aref, N. Rott, and H. Thomann. Gröbli's solution of the three-vortex problem. *Annual Review of Fluid Mechanics*, 24(1):1–21, 1992.

[7] H. Aref and M. A. Stremler. Four-vortex motion with zero total circulation and impulse. *Physics of Fluids*, 11(12):3704–3715, 1999.

[8] V. I. Arnol'd. *Mathematical methods of classical mechanics*, volume 60. Springer Science and Business Media, New York, NY, 2013.

[9] B. M. Behring. *Dances and Escape of the Vortex Quartet*. Ph.D. dissertation, New Jersey Institute of Technology, 2020.

[10] B. M. Behring and R. H. Goodman. Stability of leapfrogging vortex pairs: a semi-analytic approach. *Physical Review Fluids*, 4(12):124703, 2019.

[11] A. V. Bolsinov, A. V. Borisov, and I. S. Mamaev. Lie algebras in vortex dynamics and celestial mechanics iv. *Regular and Chaotic Dynamics*, 4(1):23–50, 1999.

[12] A. V. Borisov and A. E. Pavlov. Dynamics and statics of vortices on a plane and a sphere–i. *Regular and Chaotic Dynamics*, 3(1):28–38, 1998.

[13] P. Byrd and M. Friedman. *Handbook of Elliptic Integrals for Engineers and Scientists*. Grundlehren der mathematischen Wissenschaften. Springer Berlin Heidelberg, 2nd edition, 1971. ISBN: 9783540053187.

[14] E. A. Coddington. *An Introduction to Ordinary Differential Equations*. Prentice-Hall, Englewood Cliffs, NJ, 1955. ISBN: 9780486659428. Reprinted by Dover Publications, 1989.

[15] R. Conte. *Etude d'écoulements bidimensionnels tourbillonnaires: mouvement de trois ou quatre tourbillons ponctuels et de nappes tourbillonnaires*. PhD thesis, Université Paris VI, 1979.

[16] R. Conte and L. de Seze. Exact solution of the planar motion of three arbitrary point vortices. *Modern Physics Letters B*, 29:1530017, 2015.

[17] B. Eckhardt. Integrable four vortex motion. *Physics of Fluids*, 31(10):2796–2801, 1988.

[18] R. H. Goodman. An english translation of Gröbli's Ph.D. Dissertation: "Specielle Probleme über die Bewegung geradliniger paralleler Wirbelfäden", 2024. arXiv: 2404.01305 [physics.flu-dyn].

[19] I. Gradshteyn and I. Ryzhik. *Table of integrals, series, and products*. Academic Press, Boston, MA, 2014.

[20] W. Gröbli. *Spezielle probleme Über die Bewegung geradliniger paralleler Wirbelfäden*. PhD thesis, Georg-August-Universität Göttingen, 1877.

[21] M. Hampton, G. E. Roberts, and M. Santoprete. Relative equilibria in the four-vortex problem with two pairs of equal vorticities. *Journal of Nonlinear Science*, 24(1):39–92, 2014.

[22] H. Helmholtz. Über integrale der hydrodynamischen gleichungen, welche den wirbelbewegungen entsprechen. ger. *Journal für die reine und angewandte Mathematik*, 55:25–55, 1858.

[23] A. Hernández-Garduño. Three-point vortex dynamics as a lie-poisson system, 2016. arXiv: 1609.05851.

[24] A. Hernández-Garduño and B. N. Shashikanth. Reconstruction phases in the planar three-and four-vortex problems. *Nonlinearity*, 31(3):783, 2018.

[25] A. Hoyer-Leitzel and P. Le. Symmetric relative equilibria with one dominant and four infinitesimal point vortices. *Journal of Dynamics and Differential Equations*:1–32, 2025.

[26] C. G. J. Jacobi. *Vorlesungen uber Dynamik von CGJ Jacobi*. G. Reimer, Leipzig, 1866.

[27] G. Kirchhoff. *Vorlesungen über mathematische Physik: Mechanik*, volume 1 of *Vorlesungen über mathematische Physik*. Teubner, Leipzig, 1876.

[28] V. S. Krishnamurthy, H. Aref, and M. A. Stremler. Evolving geometry of a vortex triangle. *Physical Review Fluids*, 3(2):024702, 2018.

[29] S. Lie. Theorie der Transformationsgruppen. Zweiter Abschnitt. Unter Mitwirkung von F. Engel. German. Leipzig. B. G. Teubner. IV + 554 S. 8° (1890). 1890.

[30] Q. Luo, Y. Chen, and Q. Liu. Global phase diagrams of three point vortices. *International Journal of Bifurcation and Chaos*, 32(02):2250025, 2022.

[31] K. Lydon, S. V. Nazarenko, and J. Laurie. Dipole dynamics in the point vortex model. *Journal of Physics A: Mathematical and Theoretical*, 55(38):385702, 2022.

[32] V. Makarov. Group scattering of point vortices on an unbounded plane. *Journal of Fluid Mechanics*, 911:A24, 2021.

[33] J. E. Marsden and T. S. Ratiu. *Introduction to mechanics and symmetry: a basic exposition of classical mechanical systems*, volume 17. Springer Science and Business Media, New York, NY, 2013.

[34] J. E. Marsden, T. S. Ratiu, and R. Hermann. Introduction to mechanics and symmetry. *SIAM Review*, 39(1):152–152, 1997.

[35] V. V. Meleshko and H. Aref. A bibliography of vortex dynamics 1858-1956. *Advances in Applied Mechanics*, 41(197):197–292, 2007.

[36] K. R. Meyer. Symmetries and integrals in mechanics. In *Dynamical Systems*, pages 259–272. Elsevier, 1973.

[37] P. K. Newton and M. Platzer. N-vortex problem: analytical techniques. *Applied Mechanics Reviews*, 55(1):B15–B16, 2002.

[38] E. Novikov. Dynamics and statistics of a system of vortices. *Zhurnal Eksperimental'noi i Teoreticheskoi Fiziki*, 68(1868-188):2, 1975.

[39] T. Ohsawa. Nonlinear stability of relative equilibria in planar N-vortex problem, 2024. arXiv: 2406.12144 [math.DS].

[40] T. Ohsawa. Relative dynamics of vortices in confined Bose–Einstein condensates. *Physica D: Nonlinear Phenomena*:134639, 2025.

[41] T. Ohsawa. Symplectic reduction and the Lie–Poisson shape dynamics of N point vortices on the plane. *Nonlinearity*, 32(10):3820, 2019.

[42] L. Perko. *Differential equations and dynamical systems*, volume 7. Springer Science and Business Media, New York, NY, 2013.

[43] H. Poincaré. *Théorie des tourbillons*. Gauthier-Villars, Carré, Paris, 1893.

[44] N. Rott. Constrained three-and four-vortex problems. *Physics of Fluids A*, 2(8):1477–1480, 1990.

[45] N. Rott. Three-vortex motion with zero total circulation. *Zeitschrift für angewandte Mathematik und Physik ZAMP*, 40:473–494, 1989.

[46] M. A. Stremler. Something old, something new: three point vortices on the plane. *Regular and Chaotic Dynamics*, 26(5):482–504, 2021.

[47] J. Synge. On the motion of three vortices. *Canadian Journal of Mathematics*, 1(3):257–270, 1949.

[48] J. Tavantzis and L. Ting. The dynamics of three vortices revisited. *The Physics of Fluids*, 31(6):1392–1409, 1988.